Molecular-scale simulation of electronic processes in organic white light-emitting and single-carrier devices : steady-state and time-dependent responses

Molecular-scale simulation of electronic processes in organic white light-emitting and single-carrier devices: Steady-state and time-dependent responses

by

Murat Mesta

Submitted to the Department of Applied Physics
in Partial Fulfillment of the Requirements for the
Degree of Doctor of Philosophy

at the

Eindhoven University of Technology

March 2015

A catalogue record is available from the Eindhoven University of Technology Library

ISBN: 978-90-386-3807-2

Front cover: A photograph of OLED prototypes. Published after the permission of Lighting Research Center, Rensselaer Polytechnic Institute.

This work is funded by the research programme NanoNextNL 06D02.

Molecular-scale simulation of electronic processes in organic white light-emitting and single-carrier devices:
Steady-state and time-dependent responses

PROEFSCHRIFT

ter verkrijging van de graad van doctor aan de Technische Universiteit Eindhoven, op gezag van de rector magnificus, prof.dr.ir. C.J. van Duijn, voor een commissie aangewezen door het College voor Promoties, in het openbaar te verdedigen op maandag 30 maart 2015 om 16:00 uur

door

Murat Mesta

geboren te Ankara, Turkije

Dit proefschrift is goedgekeurd door de promotoren en de samenstelling van de promotiecommissie is als volgt:

voorzitter:	prof.dr.ir. Gerrit M.W. Kroesen
promotor:	prof.dr. Reinder Coehoorn
co-promotor:	dr. Peter A. Bobbert
leden:	prof.dr Jenny Nelson (Imperial College, London UK)
	dr. Geert H.L.A. Brocks (University of Twente, Enschede NL)
	prof.dr.ir. René A.J. Janssen
Lid TU/e	prof.dr. Herman Clercx
Reserve:	dr. Stefan C.J. Meskers

LIST OF FIGURES

LIST OF TABLES

CONTENTS

1

INTRODUCTION: CONDUCTION AND ELECTROLUMINESCENCE IN MOLECULAR SOLIDS

Organic electronics is becoming an important technology field, promising lower production costs and unique features in large area displays, solid state lighting, field-effect transistors, and solar cells. Moreover, the organic semiconductors used in organic electronics allow for mechanical flexibility[1]. The scientific interest in organic semiconducting materials dates back to the 1960's, when Pope et al.[2] and Helfrich and Schneider[3] performed one of the first studies of electroluminescence in these materials. Their work concentrated on fluorescence in molecular crystals of tetracene and anthracene in vacuum, using large biases of a few hundred volts. Applicable low-voltage OLEDs were first developed in the late 1980s from thin-film molecular materials[4] and conjugated polymers[5], while the appearance of the first commercial products took about a decade more[6,7]. In parallel to this development, the Nobel prize in Chemistry 2000 was awarded to Heeger, MacDiarmid, and Shirakawa for their discovery and development of conductive polymers. They showed[8] that doped films of polyacetylene (one of the simplest linear conjugated polymers) can have, depending on the dopant concentration, an eleven orders of magnitude conductivity range in which a metal-to-insulator transition occurs. This enormous adaptability is one of the motivations for scientists to study organic electronics.

Nowadays, a large part of organic electronics research is concentrating on lighting applications of organic light-emitting diodes (OLEDs), which involves the challenge of generating white light. In contrast to monochrome OLEDs, white light emission should be obtained by a combination of several emitting materials in a layer stack. The stack design of such 'white' OLEDs is complicated, because the stack structure as well as the material properties of each organic layer in the stack have a large influence on device performance. A predictive understanding of how material-specific parameters control the charge and excitation dynamics in white OLEDs is required for further progress in their development, and in particular for improving their energy efficiency, long-term stability, and color rendering.

1.1 OLEDS AT A FIRST GLANCE

OLEDs are ultrathin, large-area light sources made of thin films of organic semiconductors placed between one transparent and one highly reflective metallic electrode. A typical OLED is only a few hundred nanometers thick, but its surface area can reach macroscopic scales ($0.1-1\,m^2$)[9]. In principle, only one layer of organic material is sufficient to accomplish electroluminescence. However, state-of-the-art small-molecule white OLEDs[10–12] consist of several different functional organic layers, usually manufactured by thermal evaporation, organic vapor-phase deposition, spin coating, or printing*. Using a multilayer structure appears necessary to improve efficiency and lifetime as well as to obtain white light by combining† layers emitting light of different wavelengths.

A large part of white OLED research is devoted to combining different emitting materials while keeping device efficiency and lifetime as high as possible. Use of phosphorescent emitters in principle allows for almost 100% internal quantum efficiencies, meaning that every injected electron-hole pair recombines by generating a photon. One of the main issues associated with phosphorescent emitters is that their quantum efficiency is low in bulk form due to concentration quenching. Kawamura et al.[14] obtained ~100% efficiencies from Iridium(III) organic complexes, used to dope a thin-film host material. The idea here is to spatially separate the phosphorescent guests by using low dopant concentrations of $1-10\,wt\%$, so that interaction between the guests and luminescence quenching is prevented. The host material has to be chosen such that its triplet exciton energy is higher than that of the guest emitter, so that efficient exciton transfer from host to guest is obtained.

White OLED stacks making use of both phosphorescent and fluorescent emitters are called 'hybrid stacks'. The need for these kind of stacks is due to the limitations on available stable blue phosphorescent emitters. The lifetime of presently available emitters is often too short[15]. The other difficulty is the required high operating voltage of a device with a blue phosphorescent emitter, because a wide band gap host material is necessary. These two problems associated with blue phosphorescent emitters result in a very limited set of available materials for designing a fully phosphorescent OLED operating at a low voltage. In general, small-molecule hybrid white OLED stacks therefore make use of a blue fluorescent emitter and larger-wavelength phosphorescent emitters to obtain a white spectrum.

* Small-molecule OLEDs are typically prepared by thermal evaporation or organic vapor-phase deposition and polymer OLEDs by spin-coating or printing methods.

† Obtaining white light from a single layer of an organic material is not feasible, because organic materials typically have emission bands of only 50–100 nm full width at half maximum[13].

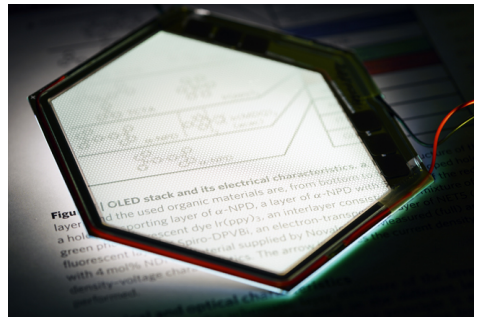

Figure 1.1.: A transparent white OLED made by Philips. Tuning the optical properties of electrodes in an OLED allows for building bottom-emitting, top-emitting, or fully transparent devices.

Depending on the optical properties of the electrodes, an OLED can be a bottom-emitting, top-emitting, or a fully transparent device (Figure 1.1). The architecture of a bottom-emitting OLED requires a transparent substrate, e.g. glass, and a transparent electrode at the substrate side. A top-emitting or fully transparent OLED allows (also) emission through the top electrode. Indium tin oxide (ITO) is a frequently used anode material that is highly transparent and electrically conductive. It is necessary for the anode material to have a high work function, while the cathode should consists of a low-work function and highly reflecting metal, e.g., Al or Ag.

Electroluminescence can occur when both types of charge carriers –holes and electrons– are injected and transported to emitter molecules such that excitons (tightly bound electron-hole pairs) are formed that decay radiatively. More specifically, one can distinguish the following processes:
(1) Injection of charge carriers. When a metallic electrode forms a contact with an organic material, charge carriers move from the Fermi level of the metal to the unoccupied molecular states of the organic molecules adjacent to the metal-organic interface. Injection may be difficult due to a possible injection barrier resulting from metal-organic interface effects (see for example Ref. 16), so it depends critically on the strength of this barrier[17]. One way of improving the injection is to introduce injection layers[18,19] made of highly p- or n-doped organic materials. The doping is achieved by introducing electron-acceptor or -donor materials into the organic semiconductor. Since doping creates free charge carriers, the Fermi level of the electrode metal aligns such that the injection barrier is lowered and a Schottky contact is formed. Different from inorganic semiconductors, doping with ions, e.g., lithium[20], may result in poor device stability because of the high diffusivity of smal ions in an organic medium. It has been shown[21] that stable doping can be realized with molecular dopants, yielding a conductivity increase by several orders of magnitude. In Chapter 5, we discuss

the layer structure of a white OLED stack that includes doped injection layers of this kind, and in Chapters 3 and 4 devices of a light-emitting-polymer with one of the most widely used doped polymer injection materials PEDOT:PSS[22] (poly(3,4-ethylenedioxythiophene):poly(4-styrenesulphonate)).
(2) Transport of charge carriers. An efficient OLED stack should have emitting layers that are well separated from the injection layers. This helps to increase the quantum efficiency, since quenching of excitons is expected near the injection regions as a result of exciton-charge interactions and interactions with the metallic electrode. Moreover, in the center of the stack the outcoupling efficiency of generated light will generally be better than elsewhere. Therefore, transporting and confining the charge-carriers to the emitting layers in the center of the stack is important. To this end, charge transport layers with high hole or electron mobilities are introduced. These can also be designed such that transport of electrons to the anode and holes to the cathode is blocked. This is important to prevent leakage of oppositely charged charge carriers and to achieve exciton confinement by keeping the carriers within the emitting layers.
(3) Formation of excitons. The strong Coulomb attraction between an electron and a hole results in a tightly bound pair, an exciton, that has a certain lifetime before recombination to the ground state occurs. An exciton is electrically neutral and carries energy. Excitons in organic semiconductors are much more strongly bound (binding energies of 0.5 – 1.5 eV[23]) than those in inorganic semiconductors because of of weaker charge screening. They are usually referred as Frenkel and Wannier–Mott excitons, respectively[24]. In the case of Wannier–Mott excitons in an inorganic crystalline semiconductor, the electron-hole pair is usually separated by more than a few lattice constants, so that the effective mass approximation can be applied. The Frenkel excitons in organic semiconductors cannot be treated in a similar way, since the excited state is composed of the molecular orbitals of an individual molecule. Another important type of exciton in organic molecular semiconductors is the charge-transfer exciton. In that case, the electron and hole reside on a pair of neighboring molecules. The binding energy and oscillator strength of charge-transfer excitons are small and they therefore often disassociate into free carriers or quickly decay to a Frenkel exciton[25]. In this thesis we only consider Frenkel excitons that are localized on a single molecule. Depending on the spin configuration of the two spin-½ carriers, the excitons can be in a spin-singlet or -triplet state. In an efficient OLED, both singlet and triplet excitons should decay radiatively. However, lifetimes of triplets are significantly longer than those of singlets, so that triplets generally take part in exciton processes that have a strong influence on the final light output of the OLED.
(4) Transfer of excitons. The transfer of excitons, or energy transfer, occurs via dipole-dipole coupling or by wave-function overlap between two emitting molecules. A detailed discussion is given in Section 2.1. In a white OLED with emitters of different color, energy transfer between emitters can have a crucial

influence on the color of the emitted light. This can also aid in gaining efficiency by transferring the excitation energy of a non-radiative triplet exciton on a fluorescent emitter to a phosphorescent emitter.
(5) Decay of excitons. The emission of photons as a result of the decay of excitons is essential for a light-emitting device. The decay process can be considered in two steps: relaxation between the electronic states and subsequent vibrational relaxation of the molecule. The emission occurs when there is an electronic relaxation and the emission wavelength is determined by the amount of energy transferred to molecular vibrations. The overlap between nuclear wave functions in the electronically excited state and the ground state determines the probability that a certain vibrational mode enters. A completely vibrational relaxation yields a non-radiative decay, which is one of the factors that limits the quantum yield of an emitter. We assume that radiative decay always occurs from the lowest excited state (Kasha's rule) and that relaxation between higher-lying excited states always occurs via non-radiative processes. We obtain the rate of non-radiative transitions from the lowest excited state to the ground state from the measured decay efficiencies and lifetimes.

The external quantum efficiency η_{EQE} is a measure of the electroluminescence performance of an OLED. It is defined as the number of photons generated per injected charge carrier and is given by:

$$\eta_{EQE} = \gamma \times r_{ST} \times \eta_r \times \eta_{out}. \tag{1.1}$$

In Equation 1.1 γ is the charge balance factor, describing the ratio between injected holes and electrons, r_{ST} is the ratio between singlet and triplet excitons* (often assumed to be equal to the statistical fraction 25% of singlet excitons formed by random encounters of two spin-½ charges), η_r is the radiative decay efficiency of the emitter, indicating the fraction of excitons that decays by emitting a photon, and η_{out} is the optical outcoupling efficiency, which is defined as the fraction of generated photons that actually leaves the device. The product of all factors but η_{out} is referred to as the internal quantum efficiency. So, even if the internal quantum efficiency is close to 100% by well balancing the charge-carrier inection and using highly efficient phosphorescent emitters[14,26], η_{out} can be the bottleneck that drastically limits the external quantum efficiency. Usually, only a fraction of the generated light will leave the device. There are several reasons for this. Light can be trapped in the OLED because of differences in refractive index between air and substrate or between substrate and emitting layer. There are different optical modes in thin-film OLED structures that cause emission loss. Depending on the angle between the surface normal and the light ray, the light may be wave-guided back into the OLED stack and at the end get absorbed or emitted at the edge. Even when the emission angle is

* r_{ST} should be replaced by 1 for phosphorescent emitters.

small enough to allow penetration into air, some fraction of the emission is lost due to coupling to substrate modes or other transparent-layer modes. Finally, surface plasmon polaritons are generated at the interface between the dielectric (organic matter) and metal electrode (cathode). The emitter can also couple to the plasmon modes. In fact, Brütting et al.[9] stress in their recent review that the coupling with surface plasmon polaritons captures more than 40% of the generated light. A rough estimate of η_{out} can be obtained[27] using the relation of geometrical optics that $\eta_{out} = 1/2n^2$, with n the average refractive index of the organic semiconductors in the OLED stack. Considering typical values[28] in the range $n = 1.6 - 1.8$, only $15 - 20\%$ of the generated light is extracted. We note that a more dedicated analysis of the above mentioned loss channels can be performed considering optical microcavity effects, but this is a research field by itself that falls outside the scope of this thesis.

In general, the efficiency of OLEDs tends to decrease with increasing current and luminance. This effect is called "efficiency roll-off" and is caused by non-trivial photo-physical processes. The efficiency roll-off at the typical operation current and luminance of OLEDs is significant[29] and future work to identify the most important reasons for this is necessary. Whenever a molecule is in an excited state, there will be interactions with the surroundings that can result in quenching of the excited state. The main processes leading to quenching are believed to be exciton-charge, exciton-exciton, and exciton-field interactions, all leading to a lower η_r in Equation 1.1. In state-of-the-art host-guest OLED systems with phosphorescent guests, triplet-triplet annihilation is proposed[30,31] to be the main cause of the quenching of platinum- and iridium-based emitters. By contrast, Kalinowski et al.[32] propose that the efficiency drop is dominated by exciton-charge interactions and field-induced quenching in similar systems. However, there is also the general view that field-induced quenching should be a rare process in phosphorescent OLEDs owing to the large triplet binding energies. We will discuss in Chapter 6 the exciton quenching and efficiency roll-off taking place in a white OLED by addressing all these relevant processes.

OLEDs can also be made using polymeric organic materials. Although the main principles are similar to those of small-molecule materials, polymeric semiconductors are electronically more complex as a result of their repeating molecular units connected via covalent bonds. One important difference between small-molecule and polymer OLEDs is the size of the recombination zone. As also described in Chapter 5, exciton generation in small-molecule OLEDs can be confined to narrow regions, depending on the effective trapping of guest emitters and the thickness of doped charge transporting layers. Excited states of a polymeric semiconductor are more delocalized. The extent of delocalization is determined by the strength of the Coulomb attraction within the bound electron-hole pair and the reorganization energy related to atomic rearrangements due to the presence of the exciton, becoming less for larger

exciton delocalization[33]. One of the great advantages of polymeric materials is the possibility to attach functional groups. These attachments can drastically change the electrical conduction as well as the emission properties of the polymer. White emission from a polymer OLED can be realized[12] using a single-component polymer sensitized with chromophores that cover a broad range of the emission spectrum. Another possibility is to physically dope the polymer with small molecules, that is, forming a host-guest system in which the polymer acts as the host for charge transport, while the emission takes place on the small-molecule emitter guests. It is possible to obtain both fluorescence[34] and phosphorescence[35,36] by selecting appropriate dopant molecules. White light can also be obtained by combining several light-emitting polymers having different emission spectra. These polymer blends can either have a single-[37] or multi-layer[38] design. The advantage of a blend is the possibility to change the emission spectrum by altering the operating voltage, a phenomenon that arises from the self-organizing properties of the blend[39]. Unfortunately, the efficiencies of these polymer OLEDs are still behind small-molecule OLEDs, because their development is hampered by the difficulty in controlling the morphology. Being multicomponent systems, the amount of each component in the final mixture sensitively depends on the processing conditions. On the other hand, polymers are more conveniently fabricated with wet processing techniques than small-molecule OLEDs, holding the promise of a low-cost solution for organic light sources.

1.2 A MOLECULAR PICTURE

Organic semiconductors are either small-molecule or polymer π-conjugated hydrocarbons, which can be doped with heavy-metal phosphorescent or other molecular compounds. Regardless of being in crystalline or amorphous form, the carbon-carbon interactions within the molecular subunits of these compounds lead to strong intramolecular and weak intermolecular electronic interactions. Their electronic and optical characteristics are very different from metals and inorganic semiconductors, and can be essentially attributed to intramolecular interactions.

The photo-physical and chemical properties of molecular solids can be understood by studying their electronic structure. This requires a quantum-mechanical treatment and solving the Schrödinger equation with the electrostatic Coulomb interaction potential. However, because of the high number of electrons and nuclei, the complexity of solving this Schrödinger equation is so large that obtaining exact solutions is not possible. The most fundamental assumption to decrease the complexity is the Born–Oppenheimer approximation[40], where the nuclei are considered as frozen in the evaluation

of the electronic wave functions. The total wave function of the system can then be separated into nuclear and electronic wave functions. Once the electronic structure is obtained, nuclear vibrations and rotations can be described within the adiabatic approximation. The total energy of a molecular state is then composed of vibrational, rotational and electronic energies. A common approach to construct the electronic wave functions is using linear combinations of atomic orbitals[41,42] (LCAOs), which combines single-electron atomic solutions (orbitals) of the Schrödinger equation to construct molecular orbitals. Spin configurations of the molecular orbitals can be introduced by multiplying individual orbitals with the corresponding spin wave functions such that the Pauli exclusion principle is obeyed. The final many-electron wave function is constructed as a Slater determinant, guaranteeing the antisymmetry of the fermionic wave function.

Molecular orbital theory and hybridization schemes are useful constructions to discuss the types of interactions among the molecules in a molecular solid. The outermost atomic orbitals of a carbon atom (2s and 2p) hybridize, leading to two different kinds of molecular orbitals, viz. σ- and π-orbitals. Conjugated polymers and small-molecule organic materials are typically sp^2-hybridized molecules in which 2s, $2p_x$, and $2p_y$ atomic orbitals make up three sp^2-hybrid molecular orbitals, corresponding to three σ-bonds per carbon atom of the molecule. The remaining p_z-orbitals form the π molecular orbitals. The electrons of the σ-orbitals are strongly localized to the bonds, whereas the π-orbitals are delocalized over the molecule. The strongly bound σ-electrons form the molecular backbone, while the weakly bound π-electrons determine the electronic structure. The latter are involved in the construction of the frontier orbitals, in particular the highest occupied molecular orbital (HOMO) and the lowest unoccupied molecular orbital (LUMO). A neutral excited electronic state on a molecule can be formed by promoting one of the two HOMO-electrons to the LUMO, forming a hole in the HOMO. A charged excited electronic state on a molecule results from placing an additional electron in the LUMO or placing a hole in the HOMO (removing a HOMO-electron). In order for charge-transfer processes to occur between a pair of molecules in organic semiconductors, there should exist an electronic coupling between the initial and final molecular states. This coupling is given by the electronic charge-transfer integral in a Hamiltonian for the wave functions of the two coupled molecules. Since the intermolecular interactions are weak in organic matter, the charge is strongly confined to a single molecule, or a few repeat units of a single polymer chain. This leads to much lower charge mobilities and smaller dielectric constants (because of less electronic screening) than in inorganic crystalline semiconductors.

Keeping this molecular picture in mind, a general description of charge transfer can be obtained from the following one-electron Hamiltonian,[13,43–45]

$$\mathcal{H} = \mathcal{H}_o + \mathcal{H}_{el} + \mathcal{H}_{el\text{-}ph} + \mathcal{H}_{dis}, \tag{1.2}$$

with $\mathcal{H}_o$ the Hamiltonian of the excited electron-phonon system excluding any electron-phonon interactions, $\mathcal{H}_{el}$ the Hamiltonian yielding electron transfer between molecules, $\mathcal{H}_{el\text{-}ph}$ the electron-phonon interaction (polaronic contribution), and $\mathcal{H}_{dis}$ including the effect of static (structural) disorder. In the linear electron-phonon coupling regime, adopting second-quantization notation with creation (destruction) operators $a_n^\dagger$ (a_n) for an electron at molecule n with energy E_n, and $b_q^\dagger$ (b_q) for a phonon with wavevector q and energy $\hbar\omega_q$, the contributions to the Hamiltonian 1.2 can be written as

$$\mathcal{H}_o = \sum_n E_n a_n^\dagger a_n + \sum_q \hbar\omega_q (b_q^\dagger b_q + 1/2), \tag{1.3a}$$

$$\mathcal{H}_{el} = \sum_n \sum_{\substack{m \\ m\neq n}} J_{nm} a_n^\dagger a_m, \tag{1.3b}$$

$$\begin{aligned}\mathcal{H}_{el\text{-}ph} = &\sum_n \sum_q g_{nq}^2 \hbar\omega_q a_n^\dagger a_n (b_q^\dagger + b_{-q}) \\ &+ \sum_n \sum_{\substack{m \\ m\neq n}} \sum_q f_{nmq}^2 \hbar\omega a_n^\dagger a_m (b_q^\dagger + b_{-q}),\end{aligned} \tag{1.3c}$$

$$\mathcal{H}_{dis} = \sum_n \delta E_n a_n^\dagger a_n + \sum_n \sum_{\substack{m \\ m\neq n}} \delta J_{nm} a_n^\dagger a_m. \tag{1.3d}$$

Here, J_{nm} is the charge-transfer integral for charge transfer between molecules n and m, g_{nq} and f_{nmq} are electron-phonon coupling constants for intra- and inter-molecular (diagonal and off-diagonal) interactions, and δE_n and δJ_{nm} are the effect of static disorder on E_n and J_{nm}. The description of charge transport can be given in three limiting cases, determined by J_{nm}, g_{nq}, f_{nmq}, δE_n, and δJ_{nm} as follows:

Band-like transport. In molecular crystals, J_{nm} is much larger than $g_{nq}^2 \hbar\omega_q$, $f_{nmq}^2 \hbar\omega_q$, δE_n, and δJ_{nm}, and band-like carrier transport may occur. Nevertheless, the bands of an organic crystal are so narrow that the mean free path of a charge carrier is a few lattice constants at most.[43,46] Fratini and Ciuchi[47] have shown that, due to the electron-phonon coupling, atomic lattice vibrations prevent band-like transport at room temperature (dynamic disorder). Organic

crystalline materials are used in field effect transistors as an active layer because of their high charge mobility[43] (10–50 cm^2/Vs). In this thesis we will not further address these materials, as they are not commonly used in OLEDs.

Polaronic transport. When $g^2_{nq}\hbar\omega_q$ or $f^2_{nmq}\hbar\omega_q$ is the dominant energy, the charge transport has a polaronic nature. Whenever a charge carrier is added to or removed from a molecule, the molecular structure strongly changes. A charge carrier coupled to an atomic rearrangement is called a polaron. The two terms in $\mathcal{H}_{\text{el-ph}}$ express that polaronic effects may influence the site energies as well as the charge-transfer integral.

Disorder-dominated transport. Organic semiconductors often display static disorder, which is independent of molecular vibrations. This disorder is solely due to variations in morphological structure –positions, orientations, and configurations of molecules. In amorphous organic semiconductors, the molecular energies, charge-transfer integrals, and thus also the charge transport, are dominated by static disorder. In the model Hamiltonian 1.2, δE_n and δJ_{nm} are now the dominant energies. The corresponding terms express the presence of diagonal and off-diagonal disorder, respectively. In the following chapters we will merely use the term "disorder" when we refer to static disorder.

1.3 METHODS OF DEVICE MODELING

Because of the need for cost-effective production, amorphous thin films of organic materials are usually used in manufacturing OLEDs, organic solar cells, and field-effect transistors. Their characteristic properties, and in particular their charge-transport properties, result from the energetic disorder. Charge transport occurs as thermally assisted tunneling, hopping, between molecules, where the strength of the electron-phonon interaction, the charge-transfer integral, and the energy difference between initial and final state determines the charge transfer rate. The spatial distribution and the time dependence of the current are related to the hopping transport. Strong spatial fluctuations in hopping rates due to the disorder lead to a filamentary structure in the current.[48*]

In general, current density–voltage curves of single-carrier organic devices show a range with a quadratic and a range with a linear dependence of the current density on voltage.[51] In the linear regime the current is injection-limited. Assuming a constant carrier mobility μ and neglecting the diffusion contribution to the current, the current density J in this regime is

$$J = e\mu n_0 V/L. \tag{1.4}$$

* This allows one to study hopping transport using percolation theory[49,50].

Here, e is the electronic charge, V the voltage, and L the thickness of the organic layer. V should be replaced by $V - V_{bi}$ whenever a built-in voltage V_{bi} exists due to the difference between the work functions of the metallic electrodes. The carrier density and electric field are then uniform and equal to n_0 and V/L, respectively, throughout the device. The carrier density n_0 is determined by the condition of thermal equilibrium between injecting electrode and the organic layer adjacent to this electrode, and therefore by the injection barrier at this electrode. In the quadratic regime, the current is space-charge-limited, with a current density given by the Mott–Gurney formula[52]

$$J = 9/8\, \epsilon \mu\, V^2/L^3, \tag{1.5}$$

where ϵ is the dielectric permittivity of the organic material. The current is space-charge-limited when $n_0 \gg n_{1/2}$ and injection-limited when $n_0 \ll n_{1/2}$, where $n_{1/2}$ is the carrier density halfway the organic layer in the case of space-charge-limited transport[53]: $n_{1/2} = \sqrt{9/8}(\epsilon/e)(V/L^2)$.

In between these two regimes, the current density–voltage characteristics of organic materials are more complicated and more advanced models for charge transport should be used. A valid model of charge transport is required to describe first of all the current density–voltage characteristics without the above simplifications. Furthermore, the energetic disorder plays an important role and should be accounted for. Analytical approaches are then difficult to obtain[45]. Use of numerical approaches is a better strategy in this case, allowing us to parameterize, for example, the dependence of the charge-carrier mobility on charge-carrier density, electric field, and temperature. Moreover, numerical approaches allow us to study different material combinations, for example in an OLED stack, and to perform a sensitivity analysis to determine the device parameters that are most critical for the performance. In the last decade, and especially with the upcoming research on efficient white OLEDs, several modeling techniques have been developed to obtain predictive descriptions of the working of organic devices. The most widely used computational device-modeling approaches are based on solving the drift-diffusion equation, solving the Pauli master equation, and performing kinetic Monte Carlo simulations.

The drift-diffusion approach

The drift-diffusion approach (see for example Ref. 54) is a simple and computationally convenient approach for OLED device modeling. It treats an organic sandwich device as a one-dimensional continuum system and ignores any lateral dependences. All physical quantities are obtained as a function of distance

x to one of the electrodes (usually the anode). The approach relies on solving three coupled equations, the drift-diffusion, the Poisson, and the continuity equation, which are, for bipolar charge transport,

$$J_e(x) = e\mu_e(x)n(x)F(x) + D_e(\mu_e)\frac{dn(x)}{dx}, \tag{1.6a}$$

$$\frac{dF(x)}{dx} = \frac{e}{\epsilon}[p(x) - n(x)], \tag{1.6b}$$

$$\frac{dn(x)}{dt} = \frac{1}{e}\frac{dJ_e(x)}{dx} - r(x), \tag{1.6c}$$

with the condition

$$V = \int_0^L F(x)\,dx.$$

Here, n (p) is the electron (hole) density, F the electric field, r the recombination rate, and D the diffusion constant. The diffusion contribution in Equation 1.6a is in general omitted when the voltage is larger than the flat-band voltage[54]. Equations 1.6a and 1.6b are written for the electron current density J_e and density n. Equivalent equations apply to holes. It is possible to obtain analytical solutions of this set of equations only for a few cases of unipolar transport. Two of these cases have been discussed above when assuming a constant mobility and neglecting diffusion: injection-limited and space-charge-limited transport. The Mott-Gurney relation for space-charge-limited transport given in Equation 1.5 gives the maximum possible current for the case of unipolar transport. An exponential trap distribution can be coupled to the above equations, resulting in a current-density-voltage relation increasing faster than quadratic until all the traps are filled[51,55].

The crude assumption of a constant μ is often dropped by considering a field-dependent $\mu(F)$ of the Poole-Frenkel type

$$\mu(F) = \mu_0 \exp(\beta\sqrt{F}), \tag{1.7}$$

where $\beta = 1/k_BT\,(e^3/\pi\epsilon)^{1/2}$. An approximate analytical solution[56] gives the current density as

$$J = 9/8\,\epsilon\,V^2/L^3 \times \exp(0.89\beta\sqrt{V/L}). \tag{1.8}$$

The influence of charge-carrier diffusion can be implemented via the Einstein relation[57], which links D to μ as $D = (k_BT/e)\,\mu$ –a generalized form can be obtained for a general density of states, see, e.g., Roichman and Tessler[58]. When the voltage is low, the diffusion current density is larger than the space-charge-limited current density[53]. Above a cross-over voltage $V_0 = (32\pi^2/9) \times (k_BT/e)$,

obtained from equating the diffusion current density $J = 4\pi^2 \epsilon \mu (k_B T/e)(V/L^3)$ to the space-charge-limited current density Equation 1.5, the current changes from diffusion- to drift-dominated[53]. When the voltage is smaller than V_0 the diffusion contribution in Equation 1.6 should be considered and solving Equations1.6 becomes more complicated.

In the case of bipolar charge transport the situation becomes even more complicated. One should then consider the influence on the space charge of both types of charge carriers and account for the recombination. A commonly used form of r is the Langevin relation $r(x) = (e/\epsilon)\, n(x) p(x) (\mu_e + \mu_h)$[13]. It has been shown by van der Holst et al.[59] that the Langevin relation has a broad validity if one takes into account the change of the mobilities of each carrier caused by the presence of the other carrier.

Gaussian disorder model

Up to this point we have not discussed how to implement energetic disorder into device modeling. A realistic and predictive model is required to account for the effect of disorder, which is substantial in both steady-state modeling[53] and modeling of time-dependent responses of organic devices[60]. The most widely used model for describing charge transport in disordered organic semiconductors is the Gaussian disorder model (GDM). Bässler[61] first proposed the GDM to study the temperature- and field-dependent mobility in organic semiconductors in a comparison with time-of-flight measurements. The model was first explored with Monte Carlo, but one can apply the GDM using other numerical techniques as well[59,62,63]. In the GDM the organic material is considered as a cubic array of point-like hopping sites and the influence of structural disorder is implemented as fluctuations in the site energies. Each lattice site is assigned an energy value derived from a Gaussian distribution

$$g(E) = \frac{N_t}{\sqrt{2\pi\sigma}} \exp[-E^2/(2\sigma^2)], \tag{1.9}$$

with N_t the total density of hopping sites and σ the standard deviation. The center of the Gaussian is taken to be equal to the HOMO or LUMO energy for holes and electrons, respectively. The Gaussian distribution may be observed in the broadening of the absorption spectra[43] or in direct measurements of the energy distribution[64].

The other ingredient of the GDM is the hopping rate between the sites. The simplest and one of the most frequently used hopping rates is the one obtained from the Miller–Abrahams formalism[61,65]:

$$W_{ij} = \nu_0 \exp(-2\alpha R_{ij}) \times \begin{cases} \exp(-\Delta E_{ij}/k_B T) & \Delta E_{ij} > 0, \\ 1 & \Delta E_{ij} \leqslant 0, \end{cases} \tag{1.10}$$

where ν_0 is a phonon-frequency prefactor. The Miller–Abrahams formalism is based on phonon-assisted tunneling and was originally proposed for electron conduction by hopping among impurities in an inorganic semiconductor at low impurity concentration, e.g., $\sim 10^{17}\,\mathrm{cm}^{-3}$ in n-type Si. In an inorganic semiconductor the impurity states are situated in between the conduction and valence band, whereas in the case of disordered organic semiconductors the sites are the intrinsic transport sites. Equation 1.10 has an asymmetric dependence on the energy difference $\Delta E_{ij} = E_j - E_i$ between the sites i and j. The excess energy from hops downward in energy is immediately transferred to the phonon heat bath, whereas the energy required for an energetically upward hop results in the Boltzmann lowering factor. The first exponential term corresponds to the decrease in electronic coupling with distance, α being the inverse wave function localization length and R_{ij} the distance between two hopping sites. Off-diagonal disorder may be included by assigning a value α_{ij} per pair of hopping sites taken from another Gaussian distribution[61]. One should consider *ab initio* electronic-structure methods to evaluate the actual electronic coupling between molecules and the change in molecular geometries involved in hopping. In this thesis we mostly consider energetic disorder and ignore off-diagonal and polaronic contributions. The reason is that we stay in the regime were static disorder dominates charge transport. Fishchuk et al.[66] argue that a critical temperature $T_c = (C/k_B E_a)\sigma^2$ defines the boundary between polaron-controlled and disorder-controlled charge transport (the dimensionless 'C-parameter' in this expression is discussed below). For $T > T_c$ charge transport is polaron-controlled, while for $T < T_c$ it is disorder-controlled. Hoffmann et al.[67] studied several π-conjugated polymers in which temperature-dependent measurements of the hole mobility suggest values of σ of $91-109\,\mathrm{meV}$, while DFT calculations yield polaron activation energies E_a of $25-46\,\mathrm{meV}$. With these values of σ and E_a, T_c is above $1000\,\mathrm{K}$, so that at room temperature the charge transport is disorder-controlled.

The description of the dependence of the mobility μ on temperature, electric field, and charge-carrier density dependence is one of the cases where disorder models yield a better agreement with measurements than other theories. We will discuss this point further starting from the temperature dependence of μ. Differently from crystalline organic semiconductors, disordered organic semiconductors show a higher mobility when temperature is raised, because of the thermal activation involved in hopping conduction. The temperature dependence at vanishing electric field was often fitted to an Arrhenius-like expression $\mu(T, F = 0) = \mu_0 \exp(-\Delta/k_B T)$, where Δ is the material-specific activation energy. Although there is no theoretical justification for this expression, it is observed to fit the measured temperature dependence well in several studies, e.g.,

Ref. 68,69. On the other hand, the GDM leads to a non-Arrhenius temperature dependence[62,70–73]

$$\mu(T, F = 0) = \mu_0 \exp\left(-C\frac{\sigma^2}{k_B^2 T^2}\right), \tag{1.11}$$

with the 'C-parameter' in the range $C = 0.4-0.5$ and given by Bässler as $C = 4/9$. Unfortunately, experimental results are only available in a limited range of temperatures and in some cases the correct T dependence is therefore open to discussion. Bässler and Köhler[43] discuss this problem regarding the T^{-1} temperature dependence of polaron models[74,75]. Mobilities are often determined by time-of-flight measurements, in which the measured signal might be dispersive. In that case the current–time plot yields a featureless decay, resulting from the still ongoing relaxation process of the charge carriers. During the relaxation process the mobility decreases until steady-state is reached. For a correct determination of the steady-state mobility, the relaxation process should be complete before the fastest charge-carriers arrive at the counter electrode. Only then can the mobility be considered as independent of the experimental parameters (for example the sample thickness[76]). When the time-of-flight signal is dispersive, the temperature dependence of the extracted mobility may seem Arrhenius-type, which can wrongly be interpreted as supporting polaronic transport. Meisel et al.[77] consider a Holstein model and show that for some conjugated polymers E_a is much smaller than σ (e.g. 30 – 60 meV for polyphenylenes with 2 – 2.5 nm polaron size), so that transport should be disorder-controlled and not polaron-controlled.

Let us now address the field dependence of the mobility. An applied electric field directly influences the site energies, making hops along the field direction more likely. Measured field dependences of μ in the field range $10^4 - 10^6$ V/cm generally show a Poole–Frenkel behavior[61,73] (Equation 1.7). In the framework of the GDM without any off-diagonal disorder, the field dependence is parameterized by Bässler as[61]

$$\mu(T, F) = \mu(T) \times \exp\left[C'\left(\frac{\sigma^2}{k_B^2 T^2} - 2.25\right) F^{1/2}\right], \tag{1.12}$$

with C' a constant (with the dimension $(m/V)^{1/2}$). Interestingly, for low σ/k_BT, μ decreases with increasing field. This is due to the fact that at low σ/k_BT carriers can at low field move around difficult passages by hopping against the field direction, while at high field they get stuck in front of those passages. The expression Equation 1.12 is only a good fit to the GDM results in a rather limited field range.

Tanase et al.[78] found that the hole mobility in poly(para-phenylene vinylene) is orders of magnitude larger in a field-effect transistor (FET) configuration than

in a diode configuration. Since the carrier density is higher in a FET than in a diode, they attributed this to a carrier-density dependence of the mobility. Pasveer et al.[79] implemented a carrier-density (n) dependence in the GDM by solving a three-dimensional master equation for the hopping transport. They proposed a parametrization known as the extended GDM (EGDM) of the form $\mu(T, F, n) = \mu(T)\, g(T, n)\, f(T, F)$, where $\mu(T)$ is the non-Arrhenius temperature dependence given in Equation 1.11, with $C \approx 0.42$. Expressions for $g(T, n)$ and $f(T, F)$ fitting to the numerical results were given. In the EGDM, the parameters are N_t, ν_0, and σ, and these will often appear in the next chapters in fits of current-voltage characteristics with the EGDM.

Correlated disorder model

The limited field range in which the Poole–Frenkel type field dependence of μ as obtained by the GDM in Equation 1.12 is valid has led to a search for alternative explanations for a Poole-Frenkel dependence. One of these explanations is the presence of correlations between site energies. In the GDM, the site energies are assumed to be uncorrelated. The correlated disorder model (CDM) considers static dipoles that may be present on the molecules[80–82], causing spatial correlations between site energies. One way to model the CDM is to place equal-magnitude point dipoles with random orientations at each point of the cubic lattice. The energy of a charge carrier at a given site j then results from charge-dipole interactions and can be calculated using[82]

$$U_j = \sum_{i \neq j} \frac{e\vec{p}_i \cdot (\vec{r}_i - \vec{r}_j)}{\epsilon \left|\vec{r}_i - \vec{r}_j\right|^3},$$

with $\vec{p}_j$ the dipole vector at position vector $\vec{r}_j$. The resulting shape of the density of states is almost a Gaussian, with a width $\sigma_d = 2.35\ ep/\epsilon a^2$, where $a = N_t^{-1/3}$ is the lattice constant. Dunlap et al.[81] found that the Poole–Frenkel field dependence is now valid in a more extended field range than in the GDM in the low carrier-density regime ($\sim 10^{-4}$ carriers per site). The temperature dependence was found to be of the type Equation 1.11 with $C = 9/25$. Bouhassoune et al.[83] extended the CDM (ECDM) by including also the carrier-density dependence, which was found to be similar to the EGDM. The temperature dependence could be modeled with $C \approx 0.29$. There is still a debate going on whether a correlated or an uncorrelated energy distribution is a better description of the energy disorder in organic semiconductors. In this thesis we follow the rule-of-thumb that for small-molecule semiconductors the ECDM should be used, while for polymers the EGDM is more appropriate[53].

Multiple-trapping model

The effect of energetic disorder on charge transport in disordered organic semiconductors can also be addressed with a multiple-trapping model. Scher and Montroll[84] introduced the continuous-time random-walk model to study anomalous charge transport in amorphous semiconductors like As_2Se_3 and a polyvinylcarbazole derivative. In this random-walk model charge carriers hop after a random time interval t that is taken from a waiting-time distribution $\psi(t)$. For the case of hopping conduction resulting from detrapping of charge carriers, the waiting-time distribution is[85] $\psi(t) = At^{-1-T/T_0}$. This power-law form of $\psi(t)$ follows from the combination of the existence of a transport energy[86], E_t, and an exponential density of trap states, $g(E) \propto \exp(-E/kT_0)$. The transport-energy concept is based on the idea that charge transport is governed by hops to sites with energy close to this energy. In equilibrium, E_t is defined as the energy of sites that are most often visited by the hopping charges. The charge carriers residing at sites with energy lower than E_t are considered as trapped carriers, which are thermally detrapped by jumping to E_t with a certain rate. Similar to this, in a multiple-trapping model a mobility edge is defined as the lowest energy of a band of states that are no longer localized. Carriers that hop from localized trap states to states with energy above the mobility edge are allowed to move freely until they are trapped again at the localized states. In this picture, the transport energy corresponds to the mobility edge. A t-dependent demarcation energy separates deep and shallow traps depending on whether trap release occurs within a time t or not. Deeply trapped carriers can then be considered as immobile within this time t. From this, a time-dependent mobility can be derived that can be used to model the frequency-dependent capacitance of sandwich-type organic devices[87].

1.4 SCOPE OF THIS THESIS

In this thesis, we study by simulations the electronic processes leading to time-dependent responses in the current of unipolar organic devices and to electroluminescence of a multilayer white OLED stack. We employ two simulation approaches: 1) solving the time-dependent master equation for the occupational probabilities of sites in the disordered semiconductor by charge carriers, 2) Monte Carlo simulations of the charge dynamics of electrons and holes as well as of exciton processes. In *Chapter 2* we discuss the theory behind the relevant electronic processes and describe the two simulation approaches. Solving the time-dependent master-equation provides a tool a with a computational efficiency sufficient to reach simulation time scales at which the complete relaxation process of injected charge carriers can be studied. It has recently been

shown that steady-state charge-transport properties of unipolar organic devices can be well described by solving a time-independent stationary master equation for the full device[59]. We extend these stationary full-device master-equation calculations to include the time dependence. We compare our results to dark-injection and impedance spectroscopy measurements in *Chapter 3* and *Chapter 4*, respectively. In dark-injection experiments, the current transient is monitored after the applied voltage over an unilluminated organic device is suddenly increased. From the shape of the transient current, information about the relaxation of charge carriers can be extracted. In *Chapter 3* the measured and simulated transient currents of devices of a polymer with a hole-transporting unit are presented. Additionally, we present current transients obtained by solving a one-dimensional time-dependent master equation that makes use of the equilibrium charge-carrier mobility. By a comparison, we can study the effect of charge-carrier relaxation. In *Chapter 4* we investigate non-stationary charge transport by analyzing charge-carrier relaxation effects in impedance spectroscopy performed on exactly the same devices as in *Chapter 3*. In impedance spectroscopy, a small-magnitude ac voltage is applied to a biased device. The frequency- and bias voltage-dependent capacitance is obtained from the measured impedance. We present measured and simulated capacitance–voltage profiles for different frequencies. In this case we can study the effect of charge-carrier relaxation by a comparison with results of a drift-diffusion model using the equilibrium charge-carrier mobility. In *Chapter 5* we present a kinetic Monte Carlo simulation study of a multilayer white OLED stack. We address the relevant electronic processes leading to electroluminescence. We simulate the charge transport of holes and electrons as well as the relevant exciton processes. We compare our simulation results with the position-dependent and color-resolved emission profiles reconstructed with nanometer-scale resolution from the measured angle- and polarization-dependent emission. This allows us to establish how the light of the different colors is generated in this particular OLED stack and to identify the factors that lower its efficiency. Furthermore, we present an analysis of the sensitivity of the current and the emission of the different colors on the device and material parameters of this OLED. In *Chapter 6* we study the decrease of the light-emission efficiency with increasing current of the OLED of Chapter 5, the so-called 'roll-off', due to triplet exciton-polaron and triplet-triplet exciton quenching. In *Chapter 7* we summarize our main conclusions and give an outlook.

2

ANALYTICAL AND NUMERICAL METHODS

ABSTRACT: In this chapter we discuss the excited-state physics of organic semiconductors that may occur through monomolecular or bimolecular processes. The understanding of how these processes follow from fundamental laws of physics is necessary to develop a valid description of charge and exciton dynamics. The generation and decay of excited states most often takes place on a single molecule, the electronic structure of which strongly influences this process and in particular determines whether the decay is radiative or not. We also discuss intermolecular interactions giving rise to energy transfer between two molecules, with either one or both molecules in an excited state. Furthermore, we describe the details of the numerical methods that we consider in our models, that is, how to solve a time-dependent three-dimensional master equation and how to perform kinetic Monte Carlo simulations.

2.1 EXCITON PROCESSES

A charge carrier appears on a molecule of an organic semiconductor device when an electron is injected from the cathode into the LUMO of a molecule or an electron is taken away from the HOMO by the anode, creating a hole. The holes and electrons migrate through the organic material and form bound states –excitons– on the same or neighboring molecules, resulting from their Coulomb attraction. Excitons can have singlet or triplet spin states. The spins of the electron and hole add up according to the quantum-mechanical rules of addition of angular momenta. This system of two spin-½ particles has simultaneous eigenvectors of the square $\mathcal{S}^2$ and the component $\mathcal{S}_z$ of the total spin operator, with eigenvalues $\hbar^2 s(s+1)$ $(s = 0, 1)$ and $\hbar m_s$ $(m_s = -s, \cdots, s)$, respectively. The state with $s = 0$ (and $m_s = 0$) is called the singlet state and the three states with $s = 1$ and $m_s = -1, 0, 1$ are called the triplet states. The energy of a singlet state is larger than than that of the degenerate triplet states because of the exchange interaction between the electron and the hole. In order to obtain a total wave function that is antisymmetric, the antisymmetric singlet spin state should be combined with a symmetric spatial wave function and the symmetric triplet spin states with an antisymmetric spatial wave function.

An excited molecule will eventually decay back to its ground state. The decay process can take place in several different ways, which can be subdivided into radiative and non-radiative transitions. If the spin-orbit coupling is absent or very small, the triplet excitons can only decay to the ground state via vibrational relaxations ("forbidden transitions"). These transition are non-radiative processes, since triplet to singlet electronic transitions are spin-forbidden*. In the presence of spin-orbit coupling –following perturbation theory– the triplet states mix with the singlets as[33]

$$\left|T'\right\rangle = |T\rangle + \sum_k \frac{\langle S_k \,|\, \mathcal{H}_{SO} \,|\, T\rangle}{E_T - E_{S_k}} |S_k\rangle \,, \tag{2.1}$$

with the spin-orbit coupling operator

$$\mathcal{H}_{SO} = \sum_i \sum_j \frac{Z_i}{\left|\vec{R_i} - \vec{r_j}\right|^3} \vec{\mathcal{L}}_{ji} \cdot \vec{\mathcal{S}}_j .$$

Here, Z_i is the atomic number of nucleus i at position $\vec{R_i}$, $\vec{\mathcal{S}}_j$ the spin operator of electron j with position $\vec{r_j}$, and $\vec{\mathcal{L}}_{ji}$ the angular momentum operator of electron j with respect to the position $\vec{R_i}$ of nucleus i. Incorporating heavy nuclei (large Z) into the molecular structure is a common method to create phosphorescent

* Since the transition dipole operator is independent of spin, the final and initial spin states have to be the same.

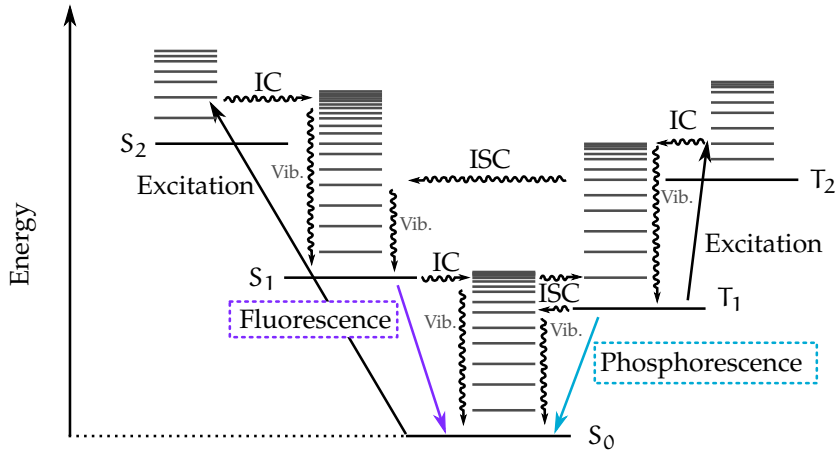

Figure 2.1.: Jablonski diagram showing transitions between excited states. The long horizontal lines labeled with S_n and T_n denote n^{th} electronically excited, but vibrationally unexcited, singlet and triplet states, with $n = 0$ the ground state. The shorter lines denote vibrationally excited states. Non-radiative processes are shown by wavy-line arrows: internal conversion (IC), intersystem crossing (ISC), and vibrational relaxation (Vib.). Processes involving absorption and emission of light are shown by full-line arrows. Adapted from ref. 88.

emitters in which the radiative triplet-singlet transitions become much more probable.

The Jablonski diagram in Figure 2.1 shows different photo-physical processes that might take place between singlet, triplet, and vibrational states of a molecule. In the diagram, the long horizonal lines labeled with S_n and T_n denote electronically excited, but vibrationally unexcited singlet and triplet states, respectively, with $n = 0$ the ground state. With increasing energy, the vibrational levels (short horizontal lines) rapidly form a band, since the density of states of a polyatomic molecule grows rapidly with increasing vibrational energy. Radiationless transitions between these states take place within picoseconds, and are indicated with vertical wavy arrows. A molecule can be excited directly to a vibrational level of, let's say, S_2, as indicated in the figure. One should note that absorption of a photon can induce only $S_0 \rightarrow S_n$ or $T_1 \rightarrow T_n$ transitions. Non-radiative transitions between vibrationally excited states $S_n \rightarrow S_m$ and $T_n \rightarrow T_m$ with $n > m$ are called "internal conversion" (IC) and occur with rates that depend on the degree of overlap between the vibrational wave functions (Franck–Condon factors) of these states. The rates are largest if the vibrational levels are close in energy. It is very often assumed –known as Kasha's rule[89]– that internal conversion and vibrational relaxation

are very rapid transitions, so that emission takes place from the first electronically excited, but vibrationally unexcited, state. In addition, depending on the strength of the spin-orbit coupling, transitions $S_n \leftrightarrow T_n$ can take place. Such transitions are known as "intersystem crossing" (ISC). An excited highly efficient phosphorescent emitter undergoes fast intersystem crossing, ending up in T_1 and followed by the decay $T_1 \rightarrow S_0$. Emission resulting from the transition $S_1 \rightarrow S_0$ is called fluorescence and emission resulting from the transition $T_1 \rightarrow S_0$ is called phosphorescence. As illustrated in Figure 2.1, not all of the decay processes $S_1 \rightarrow S_0$ and $T_1 \rightarrow S_0$ are radiative, because by IC and ISC an excited state can fully relax vibrationally without light emission. Without sufficient spin-orbit coupling, it is very likely that triplet excitons decay non-radiatively. The time scales of all these processes are roughly[88]: $k_{IC}(S_n \rightarrow S_1) \approx 10^{12}$–$10^{14}\,s^{-1}$, $k_{IC}(S_1 \rightarrow S_0) < 10^{8}\,s^{-1}$, $k_{ISC}(S_1 \rightarrow T_1) \approx 10^{6}$–$10^{11}\,s^{-1}$, and $k_{ISC}(T_1 \rightarrow S_0) \approx 10^{4}$–$10^{-1}\,s^{-1}$. The ISC from a triplet to singlet state (also known as reverse ISC), e.g. $T_1 \rightarrow S_1$ in the figure, is another pathway to fluorescence, which is referred to as "delayed fluorescence".

Interaction of light with matter

Light emission from organic devices by excited molecules where the excitation is established by electrical injection of electrons and holes is called electroluminescence. A fundamental understanding of electroluminescence is obtained by first realizing that there are three main processes through which light interacts with matter: absorption of incoming light, stimulated emission, and spontaneous emission. When the energy difference $\hbar\omega_0$ between two states of a molecule is equal to that of an incoming photon, absorption can take place, leading to a transition between the energetically lower-lying to the higher-lying state. If $\rho(\omega)d\omega$ is the energy density of the electromagnetic field in the frequency range $d\omega$, treated classically, the probability for having a transition from the lower-lying state $|i\rangle$ to the higher-lying state $|j\rangle$ after time t is, from perturbation theory[42],

$$k_{i\rightarrow j} = \frac{2e^2}{\epsilon\hbar^2}\,|\langle j\,|\,\vec{r}\,|\,i\rangle|^2 \int_0^\infty \rho(\omega)\frac{\sin^2\left[(\omega_0-\omega)\,t/2\right]}{(\omega_0-\omega)^2}\,d\omega. \tag{2.2}$$

The same result is obtained for the energetically downward transition from $|j\rangle$ to $|i\rangle$. In other words, when light is incident on a molecule in an excited state, it can stimulate a transition to a lower-lying state with a probability exactly equal to that of the upward transition. This is called stimulated emission (first predicted by Einstein[90]), crucial for the functioning of, for example, lasers. The typical decay of an excited state in a working OLED, however, is spontaneous

emission*: the downward transition releases a photon spontaneously. The transition rate of spontaneous emission can be calculated as follows[42]. Let's say in an ensemble of molecules, N_i are in state $|i\rangle$ and N_j in state $|j\rangle$. If we define A as the spontaneous emission rate and $B_{ji}\rho(\omega_0)$ as the transition rate from j to i (stimulated emission), with $\omega_0 = (E_j - E_i)/\hbar$, then

$$\frac{dN_j}{dt} = -N_j A - N_j B_{ji}\rho(\omega_0) + N_i B_{ij}\rho(\omega_0). \tag{2.3}$$

In thermal equilibrium $dN_j/dt = 0$ and N_i/N_j is a Boltzmann factor, hence

$$\rho(\omega_0) = \frac{A}{e^{\hbar\omega_0/k_B T}B_{ij} - B_{ji}}. \tag{2.4}$$

Comparing Equation 2.4 with Planck's black body radiation energy density, we obtain $B_{ij} = B_{ji}$ and

$$A = \frac{\omega_0^3\hbar}{\pi^2 c^3}B_{ji}. \tag{2.5}$$

Equation 2.5 is the rate of spontaneous emission in terms of the transition matrix element B_{ji} that follows from Equation 2.2 as $B_{ji} = (2e^2/\epsilon\hbar^2)\,|\langle j\,|\,\vec{r}\,|\,i\rangle|^2$.

In case of a large number of molecules pumped to state $|j\rangle$ we have $dN_j/dt = -N_j A$. Solving for $N_j(t)$ then gives

$$N_j(t) = N_j(0)\exp(-At). \tag{2.6}$$

The characteristic time $\tau_0 = 1/A$ resulting from this relation is called the natural lifetime of the state $|j\rangle$. From Equation 2.5 it is evident that τ_0 is inversely related to the transition moment $|\langle j\,|\,\vec{r}\,|\,i\rangle|^2$, thus τ_0 can be determined from absorption spectra. Strickler and Berg[91] showed that

$$\tau_0 = \frac{3.47\times10^8}{\nu_{max}^2}\frac{1}{\int \varepsilon(\nu)\,d\nu}, \tag{2.7}$$

where ν_{max} is the wave number [cm^{-1}] of the absorption maximum and $\varepsilon(\nu)$ the molar extinction coefficient (absorption cross-section in units of liter mole cm^{-1}). If there are more decay processes in addition to spontaneous emission, then the observed lifetime is $\tau = 1/(1/\tau_0 + \sum_i k_i)$, with k_i the rates of these processes. The quantum efficiency of the spontaneous emission is then

$$\eta = \frac{1/\tau_0}{1/\tau_0 + \sum_i k_i}. \tag{2.8}$$

The excitation energy of a molecule can also be transferred to other molecules. In the following subsections we give a brief theoretical background of these energy transfer processes.

* In quantum electrodynamics spontaneous emission is nothing but the stimulated emission by the nonzero background electromagnetic field.

Radiative energy transfer

Radiative energy transfer is often referred to as a trivial process[92] because of its conceptual simplicity. The transfer is a two-step process in which no interaction between donor (D) and acceptor (A) is required:

$$D^* \rightarrow D + \hbar\omega, \qquad \hbar\omega + A \rightarrow A^*.$$

The rate of the transfer depends on the quantum efficiency of the donor, the region of the spectrum in which the emission occurs, and the light absorption properties of the acceptor. Since the probability of radiative energy transfer does not depend on donor-acceptor separation, it can be the dominating mechanism in dilute systems in which the other energy transfer processes (which are distance dependent) are unlikely. Since in a typical thin-film OLED the excitons are confined in a region of only a few nanometers thick, radiative energy transfer is negligible in OLEDs.

Resonance energy transfer

Resonance energy transfer (Förster transfer[93]) is a non-radiative* transfer of an excitation based on weak dipole-dipole interactions present between a donor and an acceptor. The transfer occurs when there is an overlap between the emission spectrum of the donor and the absorption spectrum of the acceptor. The first observation of this kind of energy transfer was made in 1922[92] in an experiment where a vapor mixture of a donor and an acceptor metal was photo-excited at a specific wavelength only exciting the donor. The emission spectrum showed spectral lines from both species, suggesting a non-radiative excitation transfer taking place from donor to acceptor. Since no strong coupling between donor and acceptor states is required, transfer in organic semiconductors can occur up to a few intermolecular distances.

The description of Förster transfer occurs by considering four electronic quantum states: The ground $|\psi_D\rangle$ and excited $|\psi_D^*\rangle$ donor states, and the ground $|\psi_A\rangle$ and excited $|\psi_A^*\rangle$ acceptor states. Initially, we have the donor in the excited and the acceptor in the ground state. For simplicity we will assume that only two electrons are involved in the transfer, one at the donor and one at

* One should note here that resonance energy transfer is in fact mediated by photons as all electromagnetic interactions are. The transfer is referred to as non-radiative since it involves virtual photons, instead of real photons as in radiative energy transfer. A unified description of radiative and non-radiative energy transfer can be obtained in quantum electrodynamics.

the acceptor. The initial wave function, obeying the antisymmetry requirement, is[94]

$$\psi_i(1,2) = \frac{1}{\sqrt{2}}\left[\psi_{D^*}(1)\psi_A(2) - \psi_{D^*}(2)\psi_A(1)\right], \tag{2.9a}$$

where 1 and 2 refer to the coordinate and spin of the two involved electrons. Similarly, the final electronic wave function of the donor-acceptor system is

$$\psi_j(1,2) = \frac{1}{\sqrt{2}}\left[\psi_D(1)\psi_{A^*}(2) - \psi_D(2)\psi_{A^*}(1)\right]. \tag{2.9b}$$

One can apply time-dependent perturbation theory in order to calculate the transition probability from ψ_i to ψ_j under a weak dipole-dipole interaction potential given as

$$\mathcal{V} = \frac{\vec{\mu}_D \cdot \vec{\mu}_A - 3\left(\vec{\mu}_D \cdot \hat{x}\right)\left(\vec{\mu}_A \cdot \hat{x}\right)}{|\vec{x}|^3}, \tag{2.10}$$

with $\vec{x}$ the distance vector between donor and acceptor, and $\hat{x} = \vec{x}/|\vec{x}|$. The dipole operators in Equation 2.10 can be constructed using quantum-mechanical analogs[40]:

$$\vec{\mu}_D = \mu_D \hat{u}_D = -e\sum_i \vec{r}_{D,i} + e\sum_j Z_{D,j}\vec{R}_{D,j}, \tag{2.11a}$$

$$\vec{\mu}_A = \mu_A \hat{u}_A = -e\sum_i \vec{r}_{A,i} + e\sum_j Z_{A,j}\vec{R}_{A,j}, \tag{2.11b}$$

where the index i labels electrons at positions $\vec{r}_i$, and j labels nuclei with nuclear charge Z_j at positions $\vec{R}_j$. Equation 2.10 can be simplified by separating the directional contributions as

$$\mathcal{V} = \frac{\mu_D \mu_A}{|x|^3}\kappa, \tag{2.12}$$

with the orientation factor $\kappa = \hat{u}_D \cdot \hat{u}_A - 3(\hat{u}_D \cdot \hat{x})(\hat{u}_A \cdot \hat{x})$, which can also be written in terms of the angle between the two dipoles θ_{DA} and the angles θ_D and θ_A between the dipoles and $\vec{x}$ as $\kappa = \cos\theta_{DA} - 3\cos\theta_D\cos\theta_A$. We continue by writing the total Hamiltonian of the donor-acceptor system as

$$\mathcal{H} = \mathcal{H}_D + \mathcal{H}_A + \mathcal{V},$$

with the non-interacting Hamiltonians $\mathcal{H}_D$ and $\mathcal{H}_A$ of donor and acceptor, respectively. The transfer rate $k_{i\to j}$ can be obtained from Fermi's golden rule as

$$k_{i\to j} = \frac{2\pi}{\hbar}\left|\mathcal{V}_{ji}\right|^2 \rho, \tag{2.13}$$

where the matrix element $\mathcal{V}_{ji}$ is obtained, using Equations 2.9, as

$$\mathcal{V}_{ji} = \iint \left[\begin{array}{r} \psi_D^*(1)\psi_{A^*}^*(2)\,\mathcal{V}\,\psi_{D^*}(1)\psi_A(2) \\ -\psi_D^*(2)\psi_{A^*}^*(1)\,\mathcal{V}\,\psi_{D^*}(1)\psi_A(2) \end{array} \right] d1d2, \tag{2.14}$$

where $\iint d1d2$ stands for an integral over the coordinates and a sum over the spins of the two electrons. The second term of the integrand in Equation 2.14 is called the exchange term, which is discussed later. The first term is the Coulomb term, in which the acceptor electron gets excited, while simultaneously the donor electron gets de-excited. If we insert Equation 2.12 into Equation 2.13 and use Equation 2.14 we obtain

$$k_{i\to j} = \frac{2\pi}{\hbar}\frac{|\kappa|^2}{|\chi|^6}\,|\mu_D|^2\,|\mu_A|^2\,\rho, \tag{2.15}$$

where ρ is a measure of the density of the interacting initial and final states. In order to include the vibrionic contributions in ρ in the Born–Oppenheimer approximation, the electronic wavefunctions in Equation 2.9 should be multiplied with wavefunctions of the nuclear coordinates and the integrals in Equation 2.14 should also be performed over the nuclear coordinates of donor and acceptor. This brings in products of Franck–Condon factors of the donor and the acceptor. We stay in the so-called limit of "very weak coupling", where the interaction energy is so small that the time after which energy transfer takes place($10^{-9}-10^{-7}$ s) is much longer than the vibrational relaxation time ($\sim 10^{-12}$ s). Energy transfer will then take place between the vibrationally unexcited states of donor and acceptor. The product $|\mu_D|^2\,|\mu_A|^2\,\rho$ can then be replaced by the overlap integral between the emission spectrum of the donor and the absorption spectrum of the acceptor[13]:

$$\mathcal{J} = \int \frac{c^4}{\omega^4 n^4} f_D(\omega) s_A(\omega)\,d\omega. \tag{2.16}$$

Here, f_D is the normalized donor emission spectrum, s_A the normalized acceptor absorption spectrum (in units of cm²), c the speed of light, and n the refractive index of the donor-acceptor medium. A more common form of the rate can be obtained[93] by taking the integral over the inverse wave number ν [cm^{-1}] and using the molar extinction (absorption) coefficient $\varepsilon_A = (N_a/10^3 \ln 10)s_A$:

$$k_{i\to j} = \frac{1}{\tau_i}\frac{9000\ln(10)\kappa^2}{128\pi^5 n^4 N_a R_{ij}^6}\int_0^\infty \frac{f_i(\nu)\varepsilon_j(\nu)}{\nu^4}\,d\nu, \tag{2.17}$$

where τ_i is the mean life time of the donor excited state, N_a Avogadro's number, and $R_{ij} \equiv |x|$ the donor-acceptor separation. Equation 2.17 can be further simplified as

$$k_{i\to j} = \frac{1}{\tau_i}\left(\frac{R_0}{R_{ij}}\right)^6, \qquad R_0 = \frac{9000\ln(10)\kappa^2}{128\pi^5 n^4 N_a}\int_0^\infty \frac{f_i(\nu)\varepsilon_j(\nu)}{\nu^4}\,d\nu. \tag{2.18}$$

R_0 is usually referred as the Förster radius, which is the donor-acceptor separation for which the energy transfer rate is equal to the decay rate of the donor excited state. The resonance energy transfer occurs provided that both the transitions on the donor and acceptor are allowed, that is, provided that the spin selection rules are obeyed. Since there is no spin contribution the dipole-dipole interaction potential, the integration over spin states in Equation 2.14 ends up giving zero if the initial and the final spin states differ. The only allowed transition is therefore

- $^1D^* + {}^1A \to {}^1D + {}^1A^*$ (singlet-singlet),

unless the ground state is a triplet state. When phosphorescent molecules are involved, the spin-orbit coupling allows the following additional transfers:

- $^3D^* + {}^1A \to {}^1D + {}^1A^*$ (triplet-singlet),
- $^3D^* + {}^1A \to {}^1D + {}^3A^*$ (triplet-triplet),

where the triplet-triplet transfer requires two intersystem crossings and is therefore only likely in molecules with high spin-orbit coupling.

Exchange energy transfer

The other type of energy transfer is mediated by the exchange interaction between the donor and acceptor molecules. Unlike resonance energy transfer, exchange energy transfer requires orbital overlap between the excited molecular states. This requirement leads to very limited donor-acceptor separations being not more than a nanometer. In Equation 2.14 the second term of the integrand is the exchange interaction term. A rate equation can be obtained by inserting the exchange interaction matrix elements into Equation 2.13 similarly to the case of resonance energy transfer. Dexter[95] showed how to evaluate the matrix elements directly from experiments. The rate is given as

$$k_{i\to j} = \frac{2\pi}{\hbar} K \exp(-2R_{ij}/L) \times \mathcal{J}. \tag{2.19}$$

The overlap integral $\mathcal{J} = \int [f_i(\nu)\varepsilon_j(\nu)/\nu^4]\,d\nu$ of the experimentally accessible emission and absorption spectra is again used to calculated transition matrix

elements. However, the constant K is not related to any experimental spectroscopic data, so that it is in this case more difficult to fully characterize Equation 2.19 experimentally. The rate decays exponentially with the ratio of the donor-acceptor separation R_{ij} and the sum of the van der Waals radii L. The exchange mechanism obeys the Wigner spin conservation rules[96], leading to the following allowed transitions:

- $^1D^* + {}^1A \rightarrow {}^1D + {}^1A^*$ (singlet-singlet),
- $^3D^* + {}^1A \rightarrow {}^1D + {}^3A^*$ (triplet-triplet).

Quenching of excited states

Interactions between molecules in excited states can lead to loss of the excitation energy, which is called "exciton quenching". Exciton quenching has a direct negative influence on the efficiency of OLEDs. Furthermore, it can induce chemical reactions leading to irreversible degradation of the molecules. Quenching of the excited state of a donor D^* may be initiated by interactions with the same or different kinds of molecules, referred as "concentration-quenching" and "impurity-quenching", respectively. Quenching may occur by formation and decay of encounter complexes, like excimers ($D^* + D \rightarrow (DD)^*$) or exciplexes ($D^* + A \rightarrow (DA)^*$). In this section we will not consider such encounter complexes, but concentrate on exciton quenching processes based on energy transfer. These are considered to be the most important quenching processes in thin-film OLEDs.

We return to the long-range (Förster) and short-range (Dexter) energy transfer discussed above. Instead of considering an acceptor in the ground state, we may consider the situation that both the donor and the acceptor are in an excited state. One of the most commonly known quenching mechanisms is the so-called "triplet-triplet annihilation" (TTA), in which the two excited states have triplet character. There are essentially two pathways that the TTA can take: $^3D^* + {}^3A^* \rightarrow {}^1D + {}^xA^{**}$ with the spin multiplicity $x = 1, 3$ corresponding to singlet and triplet acceptor configurations ($**$ denotes a higher than the lowest excited state). When $x = 1$, both triplet excitons are quenched yielding a highly excited singlet acceptor. The singlet exciton subsequently relaxes to the lowest excited singlet state, from which the transition $S_1 \rightarrow S_0$ follows. If the acceptor is a fluorescent molecule, the TTA then results in delayed fluorescence (as described before in Figure 2.1). The main difference between regular, prompt, fluorescence and the delayed fluorescence resulting from TTA is a much longer excitation lifetime due to the two-stage decay process of the latter. When $x = 3$, the donor triplet is lost, while the acceptor is in a higher excited triplet state. Similar to the previous case, the internal conversion

$T_n \rightarrow T_1$ rapidly follows the TTA, after which a phosphorescent acceptor may decay radiatively via $T_1 \rightarrow S_0$. This process is rather important in phosphorescent OLEDs comprising several different emitting materials. When the TTA occurs between two emitters of different wavelength, the process results in a change in the color point of the OLED. An efficient OLED has an exothermic host-guest layer structure with low guest concentrations, so that the emitting (guest) molecules are spatially well separated. The TTA can in this case occur by a single-step long-range energy transfer instead of the short-range exchange energy transfer, which is generally considered to be dominant in triplet-triplet energy transfer[13]. The idea of TTA via long-range energy transfer has come up earlier, see, for example, ref. 97, but Staroske et al.[98] only recently showed that a single-step transfer was responsible for the TTA in molecular host-guest systems with phosphorescent guests. In this case, the Förster-type transfer requires an overlap between $T_1 \rightarrow S_0$ emission (donor) and $T_1 \rightarrow T_n$ absorption (acceptor) spectra.

The other common form of exciton quenching is due to the interaction of excited states with polarons –spin-½ particles in general. When the excited state is a singlet, singlet-polaron quenching occurs, resulting in either non-radiative $S_1 \rightarrow S_0$ or $S_1 \rightarrow T_1$ transitions. This leads to a decrease in fluorescence quantum yield, which may be observed experimentally by exposing fluorescent samples to high-energy electrons[99]. Similarly, triplet exciton quenching may occur by triplet-polaron quenching (TPQ). TPQ consists of the non-radiative transition $T_1 \rightarrow S_0$: $^3D^* + {}^2A_\pm \rightarrow {}^1D + {}^2A_\pm^*$, where $^2A_\pm$ ($^2A_\pm^*$) denotes an unexcited (excited) spin-doublet hole or electron polaron. Since the final spin state is a doublet, only triplet-polaron pairs with total spin of $1/2$ can undergo TPQ. TPQ can be measured from the change in the delayed fluorescence by introducing free charge carriers in a fluorescent sample[99]. In phosphorescent OLEDs the influence of TPQ can be observed at low brightness, when the TTA has almost no contribution to quenching. The TPQ increases with current and therefore with brightness, but its effect may then get overshadowed by the TTA because of the strongly increasing triplet concentration. This is especially the case when the charge-carrier balance is optimized ($\gamma \sim 1$ in Equation 1.1), in which case the probability for finding charge carriers that do not participate in exciton generation is low.

2.2 SOLVING THE MASTER EQUATION

A macroscopic quantum-mechanical system can have a large number of states $|\psi_i\rangle$ between which transitions can occur due to an interaction Hamiltonian $\mathcal{H}_{int}$. The occupational probability $p_i(t)$ of $|\psi_i\rangle$ can be considered as a first order Markovian process, i.e., the transition rates W_{ij} at a given instant only

depend on p_i at that instant and not on the history of the system. This holds true if the time scale of the evolution of the physical system is much larger than the time scale of individual transitions. In that case, the Pauli master equation describes the time evolution of p_i:

$$\frac{dp_i(t)}{dt} = \sum_{j \neq i} \left[W_{ji} p_j(t) - W_{ij} p_i(t) \right], \tag{2.20}$$

where $W_{ij} = \langle \psi_j | \mathcal{H}_{int} | \psi_i \rangle / \hbar$ is the transition rate from $|\psi_i\rangle$ to $|\psi_j\rangle$. Conservation of the total probability requires

$$\frac{d}{dt} \sum_i p_i(t) = \sum_i \sum_{j \neq i} \left[W_{ji} p_j(t) - W_{ij} p_i(t) \right] = 0. \tag{2.21}$$

In transport theory the resulting equations of Equation 2.20 are often called rate equations.

The master-equation approach has been used to study excitation dynamics in random systems[100]. We would like to have a master-equation description for the time-dependent charge transport in unipolar devices. The advantage of such a description, as compared to, e.g., a drift-diffusion description, is that it provides a time-dependent three-dimensional nanometer-scale (scale of lattice parameter) understanding of charge transport, when occupational probabilities of individual sites can be calculated for a time-interval of roughly $10^{-7} - 10^{-2}$ s. Apart from the possibility to take the effects of space charge into account, the explicit effects of Coulomb interactions cannot be straightforwardly included. The effects of the strong on-site Coulomb interaction can, however, be included by imposing the constraint of at most single occupancy of a site, turning Equation 2.20 into

$$\frac{dp_i}{dt} = \sum_{j \neq i} \left[W_{ji} p_j (1 - p_i) - W_{ij} p_i (1 - p_j) \right] \equiv g_i(\mathbf{p}), \tag{2.22}$$

where p_i is now the probability for occupancy of site i and $\mathbf{p}$ is the vector of all p_i's. Pasveer et al.[79] and van der Holst et al.[59] showed that it is possible to solve Equation 2.22 for a cubic lattice of sites at steady state ($dp_i/dt = 0$) with W_{ij} the Miller–Abrahams rate given in Equation 1.10. They used an iterative approach to obtain p_i by writing Equation 2.22 in the steady-state case as

$$p_i = \frac{\sum_{j \neq i} W_{ji} p_j}{\sum_{j \neq i} \left[W_{ij} (1 - p_j) + W_{ji} p_j \right]}. \tag{2.23}$$

This equation allows an iterative update of p_i by inserting the previous update in the left-hand side. During this update procedure, the effects of space charge

on the electrostatic potential, which depends on the p_i's, can also be iteratively included. Once convergence of the p_i's is reached, the current density is obtained by summing over the individual bond currents, yielding, in the case of a cubic lattice,

$$J = \frac{e}{a^3 N} \sum_{i,j} W_{ij} p_i (1 - p_j) R_{ij,x}, \tag{2.24}$$

with N the total number of sites, a the lattice parameter, and $R_{ij,x}$ the hopping distance along the field (x) direction between sites i and j.

In this thesis we use a more direct approach to solve Equation 2.22, since obtaining convergence using the iterative method is difficult for time-dependent calculations. We follow a similar way as Szymański et al.[101] and only occasionally use the iterative method as an initial solution or when we face convergence problems. As in the development of the (E)GDM, we assume a cubic lattice of sites, each of which has an energy $E_i = E_0 + eV_i + eV_{img}$, with E_0 the contribution of diagonal disorder, V_i the electrostatic potential including the space-charge potential, and V_{img} the image charge corrections[59]. We use the backward Euler time discretization

$$\frac{p_i^n - p_i^{n-1}}{\Delta t} = \sum_{j \neq i} \left[W_{ji} p_j^n (1 - p_i^n) - W_{ij} p_i^n (1 - p_j^n) \right], \tag{2.25}$$

where p_i^n is the solution at the current time step and p_i^{n-1} that at the previous time step. We would like to find the solution of the coupled equations Equation 2.25 and the Poisson equation $\nabla^2 V = -ep/\epsilon$ (here, p is the local charge density), but obtaining this solution is numerically very complicated, because of the large number of sites (equations) in the order of $10^5 - 10^6$. In order to decrease the complexity, first, we use a one-dimensional Poisson equation for the space-charge potential by a layer-averaging of the charge density:

$$\frac{V_{i+1} - 2V_i + V_{i-1}}{a^2} = -\frac{e}{\epsilon} \frac{1}{N_y N_z} \sum_{\substack{j \\ (j_x = i)}}^{N_y \times N_z} p_j, \tag{2.26}$$

where, as a convention, we assume that "j" actually stands for (j_x, j_y, j_z). Second, we decouple Equation 2.26 from Equation 2.25 and update the effect of the space-charge potential on the site energies at every time step[102].

The Newton–Raphson method is used to find the roots of Equation 2.25, as it allows us to reach convergence rather quickly. This method is well known among computational physicist, but we would like to mention its main points for completeness. The approach relies on how close a trial solution is to the exact solution and on the availability of the derivatives at each convergence

step. To illustrate the approach, let's consider a simple function $f(x)$ that has a root (solution to $f(x) = 0$) at $x = x_r$. One can approach to x_r by using the first-order Taylor series expansion around the trial solution x^n and obtain the updated trial solution as $x^{n+1} = x^n - f(x^n)/f'(x^n)$, where the superscript n denotes the convergence step, and $f'(x^n)$ the derivative of $f(x)$ at $x = x^n$. This is geometrically equivalent to drawing a tangent line to $f(x)$ at x^n and choosing x^{n+1} as the intersection point of the tangent line with the x-axis. Provided that the initial trial solution x^0 is sufficiently close to x_r –if not, the intersection with the x-axis will not approach x_r– and that $f'(x^n)$ is well-defined at all x^n, the method converges quadratically.

In order to apply the Newton–Raphson method to a system of nonlinear equations such as Equation 2.25, the system of equations is vectorized. Let's define the solution vector $\mathbf{p}$ as

$$\mathbf{p} = \begin{bmatrix} p_1 \\ \vdots \\ p_N \end{bmatrix}, \tag{2.27}$$

and the residue $\mathbf{F}(\mathbf{p}^n)$ of Equation 2.25 as

$$\mathbf{F}_i(\mathbf{p}^n) = \frac{p_i^n - p_i^{n-1}}{\Delta t} - \sum_{j \neq i} \left[W_{ji} p_j^n (1 - p_i^n) - W_{ij} p_i^n (1 - p_j^n) \right]. \tag{2.28}$$

The problem is equivalent to finding $\mathbf{p}$ such that $\mathbf{F}(\mathbf{p}) \approx 0$. The Newton–Raphson iteration involves solving the matrix equation

$$\mathbf{J} \Delta \mathbf{p}^n = -\mathbf{F}, \tag{2.29}$$

where $\Delta \mathbf{p}^n$ denotes the difference $\mathbf{p}^{n+1} - \mathbf{p}^n$, and the matrix $\mathbf{J}(\mathbf{p}^n)$ the Jacobian of $\mathbf{F}(\mathbf{p}^n)$, defined as

$$\mathbf{J}_{ij} = \left. \frac{\partial \mathbf{F}_i}{\partial \mathbf{p}_j} \right|_{\mathbf{p}=\mathbf{p}^n}. \tag{2.30}$$

The matrix elements of $\mathbf{J}$ can be calculated analytically:

$$\mathbf{J}_{ii} = \frac{1}{\Delta t} + \sum_{k \neq i} W_{ki} p_k^n + W_{ik}(1 - p_k^n), \tag{2.31a}$$

$$\mathbf{J}_{ij} = -W_{ji}(1 - p_i^n) + W_{ij} p_i^n. \tag{2.31b}$$

Since we decouple Equations 2.25 and 2.26, we consider the effect of Δp^n on W_{ij} by updating each row (i) of $\mathbf{J}$ with the term

$$\sum_{k \neq i} \frac{\Delta W_{ij}}{\Delta p_i^n} p_i^n (1 - p_k^n) - \frac{\Delta W_{ji}}{\Delta p_i^n} p_k^n (1 - p_i^n),$$

where

$$\frac{\Delta W_{ij}}{\Delta p_i^n} = \frac{\Delta W_{ij}}{\Delta E_{ij}} \frac{\Delta E_{ij}}{\Delta V_{ij}} \frac{\Delta V_{ij}}{\Delta p_i^n}. \tag{2.32}$$

In other words, when the occupational probabilities change, the hopping rates also change because of their dependence on the difference between site energies, which contains an electrostatic potential contribution due to the space charge. The first two factors of the chain rule in Equation 2.32 can easily be calculated analytically, while the last factor is obtained form solutions of Equation 2.26. Here, one faces the difficulty that the matrix equation Equation 2.29 cannot be solved numerically in a straightforward way, as the $N \times N$-matrix $\mathbf{J}$ has typically $N > 10^5$. Fortunately, W_{ij} can be cut off at a few lattice parameters, so that $\mathbf{J}$ is a sparse matrix. The large values of N do not allow us to use a direct sparse-matrix solver. Instead, we solve Equation 2.29 by an iterative scheme based on the numerical linear algebra method called "biconjugate gradient stabilized"[103], which we implement in our model by the commercial Fortran library NAG[104]. We note that in order to solve the matrix equation, it is not necessary to obtain $\mathbf{J}^{-1}$, which is usually not available. For the convergence criterion of the matrix solver we take $\|\mathbf{F}(\mathbf{p}) - \mathbf{J}\Delta\mathbf{p}\| < \alpha_1 \nu_0 \exp(-2\alpha) N^{1/2}$, with the adjustable convergence parameter α_1.

We now return to the iteration procedure of the Newton–Raphson method, which requires a few additional maneuvers to obtain convergence within an acceptable computation time. We start with the initial guess for the solution, which is obtained from the following self-consistent procedure. For a zero applied voltage over the device we are in thermodynamic equilibrium, so that p_i can be obtained from the relation

$$p_i = \frac{1}{1 + \exp\left[(E_i - \bar{\mu}_i)/k_B T\right]}. \tag{2.33}$$

Although the chemical potential is then constant throughout the device, the electrochemical potential $\bar{\mu}$ in Equation 2.33 depends on position[57] according to $\bar{\mu}_i = eV_i + \Phi$, with Φ the work function of the injecting electrode and V_i the electrostatic potential of site i with respect to this electrode. We solve Equations 2.26 and 2.33 iteratively by the sequence $V_i^m(p_i^{m-1}) \to \bar{\mu}_i^m(V_i^m) \to p_i^m(\bar{\mu}_i^m) \to V_i^{m+1}(p_i^m)$ until $V_i^{m+1} \approx V_i^m$, starting with $V_i^0 = 0$. We now have the solution for a voltage $V = 0$ over the device. The resulting p_i will be the initial guess in the Newton–Raphson iteration at a non-zero voltage. However, unless the initial guess is close to the actual solution, the Newton–Raphson iteration will often diverge. This would limit our method to low voltages. However, we can go to higher voltage by considering small increments in the voltage and use the solution of the previous voltage as the initial guess for the next. Another procedure improving the convergence is to introduce a mixing parameter

q such that $\mathbf{p}^{n+1} = \mathbf{p}^n + q\Delta\mathbf{p}^n$ with $0 < q \leqslant 1$. For $q = 1$ we have the regular Newton–Raphson iteration, whereas taking $q < 1$ is necessary when Δp is large. In our model we check several values of q and choose the one leading to the smallest $\mathbf{F}(\mathbf{p}^{n+1})$. We terminate the Newton–Raphson iteration when $\|\mathbf{F}(\mathbf{p})\| < a_2 \nu_0 \exp(-2\alpha) N^{1/2}$ where a_2 is the second convergence parameter.

2.3 DESCRIPTION OF THE MONTE CARLO APPROACH

Monte Carlo methods are computational algorithms based on random sampling and averaging[105]. They allow us to solve complex physical and mathematical problems that involve many degrees of freedom. The most famous Monte Carlo algorithm is no doubt the Metropolis Monte Carlo algorithm[106] that describes statistical properties of stochastic processes at equilibrium. One application of the Metropolis Monte Carlo algorithm is obtaining equilibrium geometries of interacting particles, where sampling of the geometries is achieved by moving one particle at a time following simple Monte Carlo rules that satisfy detailed balance*. It was not possible to study the time evolution of physical systems by Monte Carlo models until the 1960's, when so-called "kinetic" Monte Carlo techniques were developed[107]. Although they have different titles, like the n-fold way[108], Gillespie algorithm[109], and dynamic Monte Carlo[110], all kinetic Monte Carlo methods require a well-known rate of occurrence for the processes in question. The basic algorithm consists of forming a list of rates of possible events at every time step, randomly choosing an event from the list, updating the ensemble and the simulation time according to the chosen event and its rate, and following the same procedure until the simulation time reaches a desired value. One should note that detailed balance does not need to be obeyed, in contrast to Metropolis Monte Carlo, if the purpose is to simulate the time dependence of a system instead of equilibrium processes[110].

We would like to simulate the dynamics of charge carriers and excitons taking place in an OLED using the kinetic Monte Carlo approach. The kinetic Monte Carlo approach to charge transport in disordered organic semiconductors was first considered by Bässler and coworkers[61,111] and later by Houili et al.[112]. Studying the operation of OLEDs not only requires simulating charge transport, but also exciton processes. The availability of individual charge-carrier trajectories in kinetic Monte Carlo provides a complete description of charge transport, in contrast to the master-equation approach, which only provides

* Metropolis et al.[106] showed in their algorithm that the forth and back transition probabilities should be related by a Boltzmann factor, i.e., $W_{ij}/W_{ji} = \exp\left((E_j - E_i)/k_B T\right)$ in order to accept a Monte Carlo move without disturbing the equilibrium. This is the requirement of "detailed balance".

occupational probabilities. Another important advantage of the kinetic Monte Carlo over the master-equation approach is that, in principle, electrostatic interactions between the individual charges can be exactly taken into account. These interactions may play an important role in OLEDs, since charge accumulation commonly occurs in disordered organic semiconductors owing not only to their low charge mobility but also to the typical usage of multilayer structures. We also stress that, unlike in the master-equation approach, the study of bipolar charge transport is feasible with kinetic Monte Carlo. Furthermore, we can study exciton processes in a similar way as charge transport by introducing excitons, which may decay, be transferred, or quenched according to predefined rates.

In our kinetic Monte Carlo model, in addition to the fundamental ingredients of the (E)GDM, we consider all the electronic processes that may occur in an OLED. Our purpose is to come up with a proper and complete device model, with the goal of reaching a better understanding of the functioning of OLEDs by investigating the relevant processes in detail. We would like to analyse the sensitivity of the device performance on material parameters and the exciton processes involved in the light generation process. We therefore consider in the device model injection and dynamics of charge-carriers as well as formation, decay, energy transfer, and quenching of excitons. The initial step in the model is to construct a cubic lattice of point sites and assign a pair of HOMO and LUMO energies derived from Gaussian distributions for holes and electrons, respectively. Injecting and collecting electrode sites are then defined at the boundaries of the cubic lattice in one direction, let's say at $x = 0$ and $x = L$, while periodic boundary conditions are applied along the other two directions. The energy of the electrode sites is set to the Fermi level of the corresponding electrode. The charge injection and collection rates, like the hopping rates for charge transport, are given by well-defined hopping rates –we consider Miller–Abrahams rates, but other rates can be used as well. After this initialization, the model consists of the following algorithm: (1) The electrostatic interactions due to the charge carriers present in the lattice are calculated, including their images in the metallic electrodes. The resulting energy landscape is updated after each hop of a charge carrier. (2) The rate of all possible events (injection/collection and hopping of charges as well as all exciton processes) are calculated for all pairs of sites. A sum tree is generated containing the cumulative sums $\mathcal{W}[n] = \sum_{n'<n} \mathcal{W}_n$ of the normalized rates defined as $\mathcal{W}_n = W_n / \sum_{n'} W_n$, where n labels all possible events. (3) A random number $r \in [0, 1)$ is generated from a uniform distribution. If $\mathcal{W}[n] \leqslant r < \mathcal{W}[n+1]$, then the event n is chosen to take place at the present Monte Carlo step. The rate of an event n determines the size of the corresponding interval $[\mathcal{W}[n], \mathcal{W}[n+1]]$ in the sum tree, so that the probability that the event is chosen is indeed proportional to its rate. (4) The

simulation time t is incremented by a random waiting time Δt drawn from an exponential distribution:

$$f(t) = \Omega e^{-\Omega \Delta t}, \tag{2.34}$$

using the total rate $\Omega = \sum_n W_n$. This four-step algorithm is repeated until we have obtained sufficient statistics in the quantity that we would like to determine. The "measurement phase" should be preceded by an "equilibration phase", in which an empty device is brought to steady state. We calculate the current across a sheet between layers i and $i+1$ of the device from

$$J_i = \frac{1}{a^2 N_y N_z} \frac{1}{t} \left[\sum_{\substack{j \\ (j_x = i)}}^{N_y \times N_z} e_j m_+ - \sum_{\substack{j \\ (j_x = i+1)}}^{N_y \times N_z} e_j m_- \right], \tag{2.35}$$

where e_j is the charge at a site j, which can be $+e$, 0, or $-e$, and m_+ and m_- are the accumulated numbers of hops in the x and $-x$ direction, respectively, during the simulation time t. Equation 2.35 allows us to check whether we have reached the steady state by comparing the minimum and maximum J_i, which should approach each other in the steady state. We perform ensemble averaging by carrying out simulations with several different sets of site energies and different seeds for the random number generator.

Let us now take a closer look at the calculation of the electrostatic interactions among the charges. Taking into account the interactions between all charge pairs is computationally very demanding, but also unnecessary. We follow the approach of ref. 48 by introducing a spherical region with a cut-off radius R_c around each site i within which the contribution of charges to the electrostatic potential is taken into account exactly. The contribution of charges outside this sphere is taken into account in a layer-averaged way. The layer-averaged charge distribution only depends on x and can be considered as the "space charge", yielding a potential that can be calculated in an equivalent way as in Equation 2.26. However, this space charge also takes into account the charge within the spherical region for which the contribution to the potential was already included exactly. In order to avoid this double counting, we subtract from the potential the contribution of the layer-averaged charge within the disc-shaped regions formed by the intersection of the sphere and each layer. In addition, because of the metallic electrodes, we have to account for the image-charge potential of a charge due to its own repeated images, due to the repeated images of other charges, and due to the repeated images of the homogeneously charged disc-shaped regions. Expressions for all these contributions can be found in ref. 48. This all then leads to an electrostatic energy of a charge at a site i to which the random site-energy should be added to obtain its total energy E_i. The same should be done for all the target sites j to which the

charge can hop. It is then the energy difference $E_j - E_i$ that determines the rate for hopping of the charge from i to j. The cut-off radius R_c should be chosen sufficiently large, so that the end result becomes unsensitive to its precise value. Taking $R_c = 8-10\,a$ is found to be sufficient in most cases.

In order to investigate all the processes that lead to electroluminescence in an OLED, modeling of exciton processes should be included. The simplest approach is to extend the kinetic Monte Carlo model for charge transport in a way that the exciton processes are treated separately from the charge dynamics. The first step of this approach is to make sure that the steady state is reached, after which a record is made of the sites where exciton generation takes place. In a separate simulation, excitons are introduced at these sites and the energy transfer and decay of these excitons is simulated. Lost excitons are reintroduced such that the total number of excitons in the system remains constant. This simple approach allows us to identify the exciton generation zones, to study the effect of energy transfer on the final emission spectrum, and to obtain the efficiency drop due to non-radiative decay. A complete and simultaneous modeling of charge dynamics and exciton processes is achieved by combining all the possible processes into a single Monte Carlo simulation. To this end, the rates given in Equation 2.17 and 2.19 are embedded into the simulation, while following the same main algorithm. Quenching of excitons can be introduced in several ways. The simplest way is to assume that exciton quenching occurs immediately when two excitons or an exciton and a charge are on nearest-neighbor sites. More realistic is to assume that quenching occurs when one exciton is transferred to the site of another, when an exciton is transferred to a site where a charge is present, or when a charge hops to a site where an exciton is present. Finally, we note that whenever an exciton is formed, the exciton binding energy should be accounted for. Triplet excitons are more strongly bound than singlet excitons and therefore have a larger exciton binding energy. We assume that singlet and triplet excitons are formed with the spin-statistical ratio of 1:3. A first application of the complete and simultaneous modeling of charge dynamics and exciton processes to the study of the efficiency roll-of of phosphorescent light-emitting diodes was given in ref. 113.

3

CHARGE-CARRIER RELAXATION IN DISORDERED ORGANIC SEMICONDUCTORS STUDIED BY DARK INJECTION: EXPERIMENT AND MODELING*

ABSTRACT Understanding of stationary charge transport in disordered organic semiconductors has matured during recent years. However, charge-carrier relaxation in non-stationary situations is still poorly understood. Such relaxation can be studied in dark injection experiments, in which the bias applied over an unilluminated organic semiconductor device is abruptly increased. The resulting transient current reveals both charge-carrier transport and relaxation characteristics. We performed such experiments on hole-only devices of a polyfluorene-based organic semiconductor. Modeling the dark injection by solving a one-dimensional master equation using the equilibrium carrier mobility leads to a too slow current transient, since this approach does not account for carrier relaxation. Modeling by solving a three-dimensional time-dependent master equation does take into account all carrier transport and relaxation effects. With this modeling, the time scale of the current transient is found to be in agreement with experiment. With a disorder strength somewhat smaller than extracted from the temperature-dependent stationary current-voltage characteristics, also the shape of the experimental transients is well described.

* This chapter is based on the work that has been published: M. Mesta, C. Schaefer, J. de Groot, J. Cottaar, R. Coehoorn, and P.A. Bobbert, *Phys. Rev. B*, 88(17), 174204 (2013).

3.1 INTRODUCTION

In the understanding of the functioning of organic semiconductor devices, such as organic light-emitting diodes (OLEDs), knowledge about the various aspects of the charge dynamics in these devices is crucial. In recent years, much progress has been made in measuring and modeling the charge-carrier mobility μ in such devices under stationary conditions. Key to a proper description of charge transport is the energetic disorder present in the organic semiconductors used in these devices. This disorder is commonly described by assuming that carriers hop between sites having random energies, which are often assumed to be distributed according to a Gaussian density of states (DOS) with a standard deviation σ, henceforth called the "disorder strength". The resulting model is called the "Gaussian disorder model" (GDM)[61]. At increasing carrier densities state-filling effects come into play, leading to a dependence of μ on the charge-carrier concentration c [78,79,114,115]. Together with the dependence of the mobility on temperature, T, and electric field, F, this has led to the "extended Gaussian disorder model" (EGDM). A parametrization of the mobility function $\mu(T, c, F)$ within the EGDM was constructed in Ref. 79. It has been proposed that spatial correlation in the energies of the sites can be present, for example due to presence of dipoles[80,82], leading to the "correlated disorder model" (CDM). When also in this model the density dependence is included, this results in the "extended correlated disorder model" (ECDM)[83].

Charge transport in organic semiconductors can be studied in single-carrier devices, in which carrier-injecting electrodes are used with work functions that are close to either the highest occupied molecular orbital (HOMO) or lowest unoccupied molecular orbital (LUMO) of the semiconductor. By this it is possible to study the transport of holes and electrons separately. By modeling the current density-voltage, J-V, characteristics of such devices using different mobility functions, one can extract values for the disorder strength σ and the density of sites N_t, and judge whether the EGDM or ECDM provides the most appropriate mobility function. It has been found that charge transport in two typical small-molecule semiconductors, α-NPD[116] (a hole conductor) and BAlq[117] (an electron conductor) can be described most appropriately with the ECDM. On the other hand, charge transport in polymeric semiconductors like two PPV-based polymers[79,83] (hole transport) and a polyfluorene-based polymer[62,118] (hole and electron transport) can be described best with the EGDM. Description of electron transport requires the consideration of traps, which makes the analysis more involved[117,118].

However, studies of stationary properties like J-V characteristics can provide only a limited insight into charge dynamics, because they do not address the possible time dependence of the charge transport. A large body of work exists

on the time dependence of charge transport in disordered, organic and inorganic, solids. The standard technique to study time-dependent transport is a time-of-flight (TOF) experiment, where in a sandwich device of a disordered solid a sheet of carriers is photogenerated at one of the electrodes, after which the carriers move to the opposite collecting electrode in an applied electric field. Dispersion in the transport leads to different carrier arrival times at the collecting electrode, resulting in a smoothly instead of abruptly decaying current transient. Such transients are often described in terms of the Scher–Montroll theory[84], which has, for example, been quite successfully applied in the case of a molecularly doped polymer[119]. In the case of semiconducting polymers TOF experiments can be used to extract the carrier mobility and its dependence on temperature and electric field[120]. The effect of relaxation of an excitation in the DOS of localized states[121] has also been analyzed with TOF experiments[122]. A difficulty with TOF experiments, however, is that relatively thick ($\sim$ µm or more) layers should be used to make sure that the photogeneration occurs in a region that is narrow as compared to the total device thickness. This makes TOF experiment unsuitable for studying time-dependent transport in the relatively thin devices ($\sim$ 100 nm) that are of importance for OLED studies.

Alternative techniques to study time-dependent transport in thin devices are available. Recently, impedance-spectroscopy studies were performed on hole-only devices of a polyfluorene-based polymer (the same as in Refs. 62 and 118), with a thickness around 100 nm, showing the importance of carrier-relaxation effects[87]. A fair description of the frequency- and voltage-dependent capacitance could be obtained within a one-dimensional (1D) multiple-trapping model for carrier relaxation[87]. In that study, the following approach was used: (1) three-dimensional (3D) Monte Carlo (MC) calculations were carried out to obtain the time-dependent mobility after a sudden very small increase of the charge density, providing the (complex) frequency dependent mobility after a Fourier transformation, and (2) this result was included in a 1D calculation of the (complex) frequency dependent current density. Because this approach is indirect and rather involved, it is of interest to analyze the results of transient current-density measurements using a more direct fully 3D approach.

Here, we extend the study of carrier-relaxation effects by performing and analyzing so-called "dark injection" (DI) experiments on these hole-only devices. In DI experiments the bias applied over an unilluminated semiconductor device is abruptly increased and the current transient as a function of time is recorded. Because instantaneous injection of extra charges occurs by the bias step, DI experiments are in spirit comparable to TOF experiments. However, DI experiments are more flexible, because they can be applied to thinner devices. Furthermore, they are applicable to situations with much higher carrier densities, outside the independent-particle Boltzmann regime, as is relevant to, for example, OLED applications. DI experiments were used extensively to

study charge transport in OLEDs by Poplavskyy et al[123–125]. An early theoretical description of DI transients was given by Many and Rakavy[126]. In their description, space-charge effects are taken into account, but the mobility μ is assumed constant, i.e., no dependence of μ on carrier density and electric field is taken into account and no relaxation. Also, diffusion is not accounted for. Within this description a peak in the transient current occurs at a time $t_{peak} = 0.786\, t_{SCF}$, where t_{SCF} is the space charge-free carrier transit time. The latter is given by $t_{SCF} = L^2 / \mu V$, where L is the thickness of the device and V the applied voltage. An improvement of the Many-Rakavy theory, applicable to organic semiconductor devices, was provided by Knapp and Ruhstaller[127], by using the carrier-density and field dependence of μ from the EGDM. In their description, the 1D time-dependent drift-diffusion (DD) equation for the carrier density is solved in conjunction with the 1D Poisson equation for the electric field, with the diffusion coefficient obtained from the mobility via the generalized Einstein equation[58]. These authors recently applied their technique to the study of traps[128]. Their 1D DD approach is presently considered to be the state of the art in DI modeling. In the present work we will instead use an approach in which a time-dependent 1D master equation (ME) is solved, which treats drift and diffusion on equal footing[129]. Results obtained with this approach are very similar to those obtained from the 1D DD equation, but the application of the 1D ME approach is more convenient and simple[129]. However, neither the 1D DD nor the 1D ME approach accounts for carrier relaxation.

Instead of using the indirect multiple-trapping model of Ref. 87 to take into account relaxation effects, we follow here a direct and more fundamental approach in which the 3D time-dependent master equation for the occupational probabilities of a system of hopping sites representing the full device, including the injecting and collecting electrodes, is solved. This approach was very recently for the first time applied in the calculation of DI transients by Szymański et al.[101] The approach followed by us is in essence an extension of the stationary full-device ME calculations earlier explored by us[59] to include time dependence. We benchmark these 3D ME calculations with 3D MC simulations on the same hopping system, which are only feasible for thin devices and high voltages. In these simulations all effects of Coulomb interactions can be taken into account, whereas in the 3D ME calculations the Coulomb interactions can only be taken into account in a layer-averaged way[59]. The difference turns out to be unimportant.

In Section 3.2, we describe the DI experiments and present their results. We also present the J-V characteristics of the investigated devices, which are used to extract parameters for the DI modeling. The modeling approaches are described in Section 3.3. In Section 3.4 we present the modeling results and the

comparison with the experiments. Section 3.5 contains a summary, discussion, and conclusion.

3.2 EXPERIMENTAL

The experimental setup to perform the dark injection (DI) measurements is shown in Figure 3.1 (a). A voltage $V(t)$ is applied over the device, which is placed in series with a load resistance of 100 Ω. The current through the device is determined by measuring the voltage over the load resistance. The voltage $V(t)$ consists of a pulse train as indicated in Figure 3.1 (b), which allows us to judge the reproducibility of the transients and to increase the signal-to-noise ratio. The load resistance was chosen large enough to allow an accurate measurement of the current, but still such that it only significantly influences the current for short times $t < 2 \times 10^{-6}$ s after the onset of a pulse, which is smaller than the times for which the interesting structures in the transients appear. The load resistance is taken into account in most of our modeling.

The studied hole-only devices have the structure glass | ITO (100 nm) | PEDOT:PSS (100 nm) | LEP | Pd (100 nm). The light-emitting polymer (LEP) consists of polyfluorene with co-polymerized triarylamine units for hole transport (Lumation™Blue series, supplied by Sumation Co., Ltd.); see the inset of Figure 3.1 (c). The devices are the same as those studied in Refs. 62, 130, and 87 and have three different LEP-layer thicknesses: $L = 67$, 98, and 122 nm. The surface area of all three devices is $A = 9 \times 10^{-6}$ m^2.

Without a voltage offset in the DI experiments, the off-time needed to return to the initial state of the device before application of a next voltage pulse turned out to prohibitively long. We attribute this to very slow trapping/detrapping of charge carriers by deep traps. With a finite offset voltage, however, this can be circumvented. The reason is probably that the deep traps then remain filled and that the trapping/detrapping dynamics of the now relevant shallower traps is much faster. We chose to perform all experiments with an offset of 1.5 V, for which the reproducibility of the transients is very good. The shape of the transients was investigated as a function of the duty cycle (pulse duration as a fraction of the repetition time). The measurements discussed here were obtained with a duty cycle of 1%, for which memory effects were found to be negligible. The repetition frequencies ranged from 0.01 to 1 Hz, where the lower frequencies are needed for the measurements of the transients for longer times (10-800 ms).

A typical measured DI transient for the $L = 122$ nm device is given by the solid black line in Figure 3.1 (c) for a pulse amplitude of 8 V. The high current at

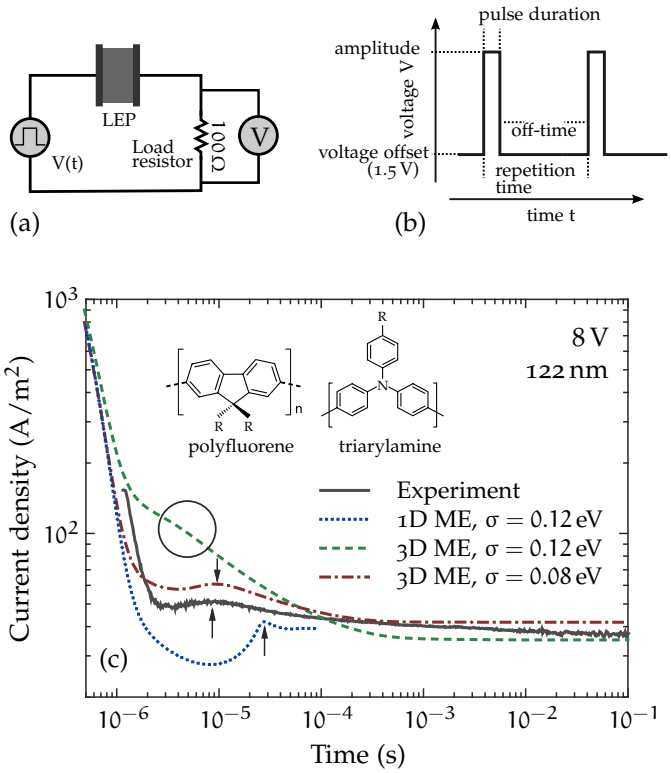

Figure 3.1.: (a) Measurement setup for the dark-injection (DI) experiments. (b) Applied voltage pulse sequence. An offset voltage of 1.5 V is used. (c) DI transients for a device with a 122 nm thick polymer layer and a pulse amplitude of 8 V. Solid lines: measurements. Blue dotted lines: results of the one-dimensional master equation (1D ME) approach. Green dashed and red dash-dotted lines: results of the three-dimensional master equation (3D ME) approach for two different values of the disorder strength σ. The arrows indicate the peak position in the transients, and the circle a shoulder in the 3D ME transient for $\sigma = 0.12$ eV. The error bars of all presented results are negligible. The inset in (c) shows the chemical structure of the used light-emitting polymer (LEP).

short times is mostly due to the rapid charging of the device through the load resistance (the RC-times of our devices are 0.2-0.4$\times 10^{-6}$ s). The current then reaches a minimum at about 3×10^{-6} s, after which a maximum appears at about 8×10^{-6} s. This maximum, indicated by an arrow, is equivalent to the peak in the Many-Rakavy theory, signalling the arrival at the collecting contact (in this case the Pd electrode) of the front of the space charge injected at the onset of the voltage pulse by the injecting contact (in this case PEDOT:PSS). Finally, the current relaxes to the steady-state current at the pulse amplitude

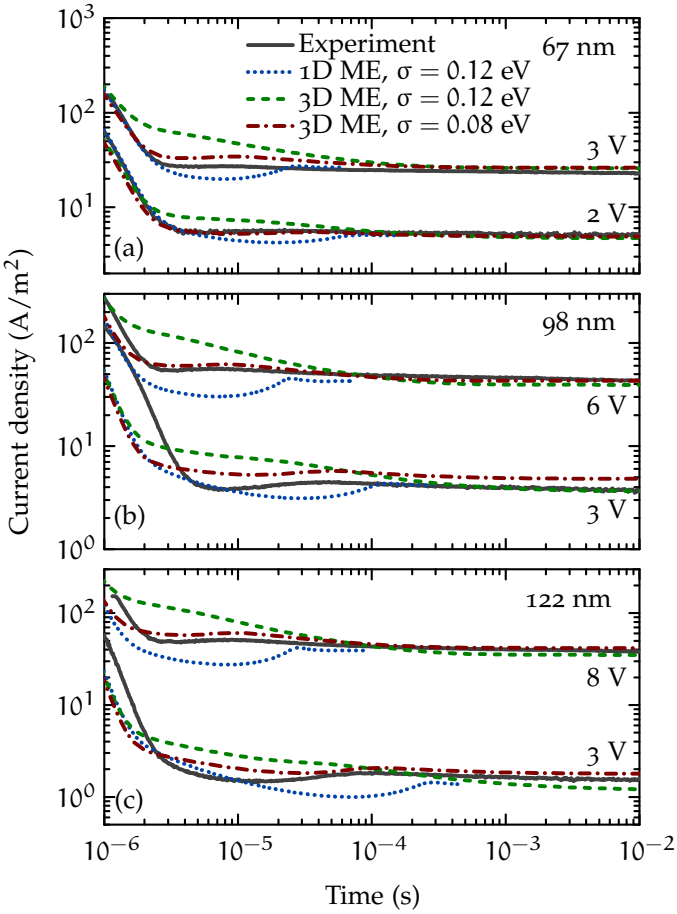

Figure 3.2.: DI transients for different pulse amplitudes for devices with LEP-layer thicknesses of (a) L = 67, (b) 98, and (c) 122 nm. The parameters used in the 1D and 3D ME modeling are given in Table 3.1. The transient presented in (c) for a pulse amplitude of 8 V is the same as in Figure 3.1 (c).

of 8 V. Figures 3.2 (a), (b), and (c) give the transients for the L = 67, 98, and 122 nm devices, respectively, for different pulse amplitudes. The shapes of all transients are roughly equal, but the time at which the peak occurs depends on the pulse amplitude and the device thickness. The peak time as a function of voltage is plotted in Figures 3.4 (a)-(c) for the three devices (black circles). The peak positions of transients at other voltages than those plotted in Figure 3.2 were included in the data.

The current density-voltage (J-V) characteristics of the investigated three devices were measured in Ref. 62 for different temperatures. We re-measured the

room-temperature J-V characteristics of the same devices and the results are displayed in Figure 3.3. They show almost no difference from the results in Ref. 62, demonstrating that the devices are stable over at least five years.

3.3 THEORY AND SIMULATION

One-dimensional master equation (1D ME)

The approach in which the current is calculated by solving a one-dimensional master equation (1D ME) was introduced in Ref. 129. Within the 1D ME approach drift and diffusion are both automatically included, in contrast to the approach in which the one-dimensional drift-diffusion (1D DD) equation is solved, in which drift and diffusion appear as separate terms. Charge transport in the 1D ME approach is described as nearest-neighbor hopping along a linear chain of discrete sites with a site separation a. The hopping rate is chosen such that the carrier concentration-dependent mobility at zero electric field obtained from the extended Gaussian disorder model[79] (EGDM) is reproduced. In the presence of an electric field, exponential hopping rate enhancement and suppression factors are included for down-field and up-field hops, respectively.

The occupational probability c_i at site i satisfies the master equation

$$\frac{dc_i}{dt} = c_{i-1} r_i^+ + c_{i+1} r_{i+1}^- - c_i (r_{i+1}^+ + r_i^-), \tag{3.1}$$

where $r_i^{+(-)}$ is the forward (backward) hopping rate across the interval from $i-1$ to i. The coupled master equations for all sites can be solved numerically by appropriate methods. The time-dependent electric field follows from Poisson's equation and evolves together with the carrier concentration. In this way, time-dependent space-charge effects are taken into account. After the time-dependent carrier concentrations have been found, the time-dependent current density is obtained from

$$J(t) = \sum_i (c_{i-1} r_i^+ - c_i r_i^-) \frac{e}{a^2} + \frac{\epsilon_0 \epsilon_r}{L} \frac{dV}{dt}, \tag{3.2}$$

where e is the electronic charge. The second term on the right-hand side is the displacement current density, where ϵ_0 is the vacuum permittivity and ϵ_r the relative dielectric constant of the LEP, which was determined to be $\epsilon_r = 3.2 \pm 0.1$.[62] In a stationary situation the left-hand side of the master equation Eq. (3.1) is zero and the displacement current density vanishes.

The effect of the load resistance can be accounted for without too much effort. The total applied voltage is a sum of the voltage drop over the device, V_{device},

and the load resistor, V_R. The latter is calculated using Ohm's law, $V_R = AJR$, after obtaining the current density in the device, J, from Eq. (3.2). Since the latter depends on V_{device}, an iterative procedure is followed. We note that carrier-relaxation effects are not included in the 1D ME approach: c_i represents the carrier concentration in a sheet and not the occupation of an actual site in the organic semiconductor. The effect of disorder on the transport is taken into account via the hopping rates r_i, as determined from 3D ME calculations under stationary conditions. They do not show the effective time dependence due to the presence of an out-of-equilibrium density of occupied states that arises under non-stationary conditions.

Three-dimensional master equation (3D ME)

Charge carrier-relaxation effects are included in the three-dimensional master-equation (3D ME) approach. In this approach the LEP is represented by a regular cubic lattice with lattice constant a, where each lattice point is a site that can hold at most one charge carrier. Calculations of the stationary current density in complete single-carrier devices with the 3D ME approach were pioneered in Ref. 59. In a non-stationary situation a time dependence should be added to the occupational probabilities of the sites. In a simulation of a DI experiment, first the occupational probabilities of the sites are determined for the initially applied voltage in exactly the same way as in Ref. 59. After the voltage step, the electric field in the device, and thus the energy of every site, has changed. As a result, the hopping rates between the sites have changed and the system is no longer in a stationary situation: extra carriers are injected from the injecting electrode into the adjacent organic sites and travel to the collecting electrode, while relaxing to lower energies. Furthermore, the field becomes time dependent due to the time-dependent charge-carrier density. This requires extension of the approach of Ref. 59 to include time dependence, as described below.

The x-direction of the simulation box is the direction of current flow. The size of the simulation box is $L \times L_y \times L_z$ and we use periodic boundary conditions in the y- and z-directions. For the lateral size of the simulation box we take $L_y = L_z = 50a$, which was found to be sufficient in steady-state ME calculations for similar devices.[59] The energies of the sites consist of a random contribution due to the energetic disorder in the polymer and a contribution due to the electric potential. The random contribution is chosen from a Gaussian DOS centered at the highest occupied molecular orbital (HOMO) of the LEP:

$$g(E) = \frac{1}{\sqrt{2\pi}\sigma} \exp\left[-(E-\Delta)^2/2\sigma^2\right], \tag{3.3}$$

where the standard deviation σ of the Gaussian is the disorder parameter and Δ is an injection barrier with respect to the injecting contact (PEDOT:PSS).

We assume that charges hop between nearest neighboring sites with a hopping rate given by the Miller-Abrahams formula[65] (Equation 1.10) with $R_{ij} = a$. For α we take $10/a$, as in Ref. 79, but this value only influences the prefactor in the case of nearest-neighbor hopping. A small injection barrier of $\Delta = 0.1$ eV at the injecting contact, found in Ref. 62, is taken into account in our simulations.

The master equation governing the time dependence of the occupational probability p_i of a site i is now

$$\frac{dp_i}{dt} = \sum_{j \neq i} \left[W_{ji} p_j (1 - p_i) - W_{ij} p_i (1 - p_j) \right]. \tag{3.4}$$

The details of how to solve Equation 3.4 were given in Section 2.2. A time-dependent electric field in the x-direction is obtained by solving a one-dimensional Poisson equation, in which a layer-averaged charge density is taken that only depends on x. In this way, the effects of space charge are taken into account in the 3D ME approach.[59] After obtaining the p_i's by solving the coupled master equations of all sites, the current density is obtained from

$$J(t) = \frac{e}{L L_y L_z} \sum_{i,j} W_{ij} p_i (1 - p_j) R_{ij,x} + \frac{\epsilon_0 \epsilon_r}{L} \frac{dV}{dt}, \tag{3.5}$$

where $R_{ij,x}$ is the x-component of the vector between sites i and j.

The time-dependent coupled master equations Eq. (3.4) are solved numerically by an implicit Euler method in discretizing the time derivative, followed by Newton's method to calculate the p_i's at the current time from those a time step earlier. The effect of the load resistance is taken into account in a similar way as in the 1D ME approach.

Three-dimensional Monte Carlo (3D MC)

It has recently been demonstrated that it is feasible to perform three-dimensional Monte Carlo (3D MC) simulations to study stationary charge transport in complete organic devices[11,48]. In these simulations it is possible to include Coulomb interactions explicitly. In the 3D ME approach this is not possible, because in that approach only average occupational probabilities are considered and thus only the effects of space charge can be accounted for. The 3D MC approach can therefore be applied as a check of the validity of the neglect of explicit Coulomb interactions in the 3D ME approach.

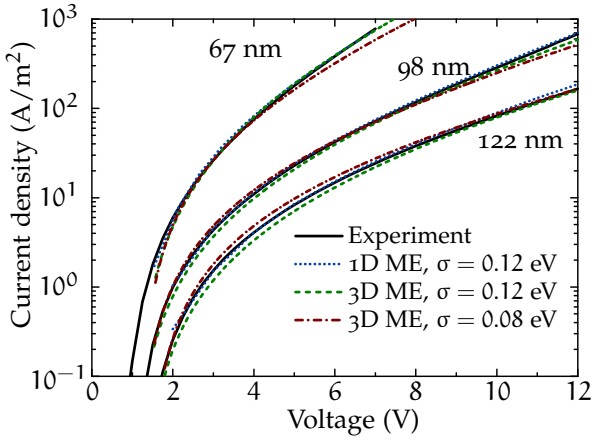

Figure 3.3.: Current density versus voltage, J-V, characteristics of the three devices with different LEP-layer thicknesses. Fits to 1D and 3D ME modeling results lead to the parameters given in Table 3.1.

In the 3D MC approach the same cubic lattice of sites and the same hopping rate (Miller-Abrahams) is considered as in the 3D ME approach. However, now explicit hop events are chosen according to their rates and therefore the approach simulates what would actually happen in a real device. After every hop a charge moves and the 3D electric potential changes, requiring an update of all hopping rates. This makes the approach computationally expensive, although this can be mitigated by updating only hopping rates of charges in a sphere around the charge that hopped.[48] By studying the steady-state current density as a function of sphere radius we concluded that a radius of $8a$ is sufficient.

It is straightforward to extend the stationary 3D MC simulations of Ref. 48 to study transients. The now time-dependent current density is simply calculated by counting the net number of charges in the device that have hopped in the x-direction in a certain time interval. This interval should be smaller than the time scale of the features appearing in the transients, but large enough to obtain sufficient statistics. The transients can be well captured by taking time intervals that grow exponentially with time. Taking into account the effect of the load resistance in the 3D MC simulations is cumbersome, so we refrained from doing that in the comparison with the 3D ME calculations.

3.4 MODELING RESULTS AND COMPARISON WITH EXPERIMENT

Before the DI transients can be modeled, the modeling parameters should be determined. We did this by first performing stationary 1D ME calculations

Parameter	This work	Earlier work[62,130]
N_t [10^{26} m^{-3}]	4.28	6 ± 1
σ [eV]	0.12	0.13 ± 0.01
$\nu_0^{67\,nm}$ [10^{18} s^{-1}]	4.7	
$\nu_0^{98\,nm}$ [10^{18} s^{-1}]	2.8	
$\nu_0^{122\,nm}$ [10^{18} s^{-1}]	2.8	
$\mu_0^{67\,nm}$ [10^{-12} m^2/Vs]	6.3	5 ± 2
$\mu_0^{89\,nm}$ [10^{-12} m^2/Vs]	4.2	5 ± 2
$\mu_0^{122\,nm}$ [10^{-12} m^2/Vs]	4.3	5 ± 2
$V_{bi}^{67\,nm}$ [V]	1.57	1.66 ± 0.05
$V_{bi}^{98\,nm}$ [V]	1.54	1.63 ± 0.05
$V_{bi}^{122\,nm}$ [V]	1.80	1.87 ± 0.05
σ [eV]	0.08	
$\nu_0^{67\,nm}$ [10^{16} s^{-1}]	8.2	
$\nu_0^{98\,nm}$ [10^{16} s^{-1}]	4.9	
$\nu_0^{122\,nm}$ [10^{16} s^{-1}]	4.9	

Table 3.1.: Simulation parameters used in the 1D and 3D ME calculations, based on fits to the experimental J-V characteristics of Figure 3.3. The results of earlier work[62,130] are also given. The parameter values for ν_0 in the bottom part of the table apply to 3D ME calculations with a disorder strength σ that has been reduced to 0.08 eV. All other parameters of these calculations are the same as in the top part.

and fitting the results to the J-V characteristics of Figure 3.3. The parameters with which the best fits were obtained for the three devices are given in Table 3.1. The fit parameters are, next to N_t and σ, the mobility μ_0 at vanishing electric field and charge-carrier concentration, and the built-in voltage V_{bi} (the work function difference between the PEDOT:PSS and the Pd electrode). Excellent fits (blue dotted lines) to the experimental J-V curves are obtained with parameters that are compatible with the parameters determined in the earlier analysis of exactly the same devices in Refs. 62 and 130. Slightly different fabrication conditions between the three devices could have led to the slight differences in μ_0 and V_{bi}. With the parameters of Table 3.1, also excellent fits to the experimental J-V curves can be obtained with stationary 3D ME simulations (green dashed lines), providing values for the intrinsic hopping rates ν_0 in Eq. (1.10). The value for the lattice constant a is obtained from N_t in this table as $a = 1/N_t^{1/3} = 1.33\,nm$.

The predictions for the peak times from the Many-Rakavy theory, $t_{peak} = 0.786L^2/\mu_0 V$,[126] obtained with the values for μ_0 in Table 3.1, are plotted in Figure 3.4 (gray lines). Clearly, the Many-Rakavy theory is unable to predict

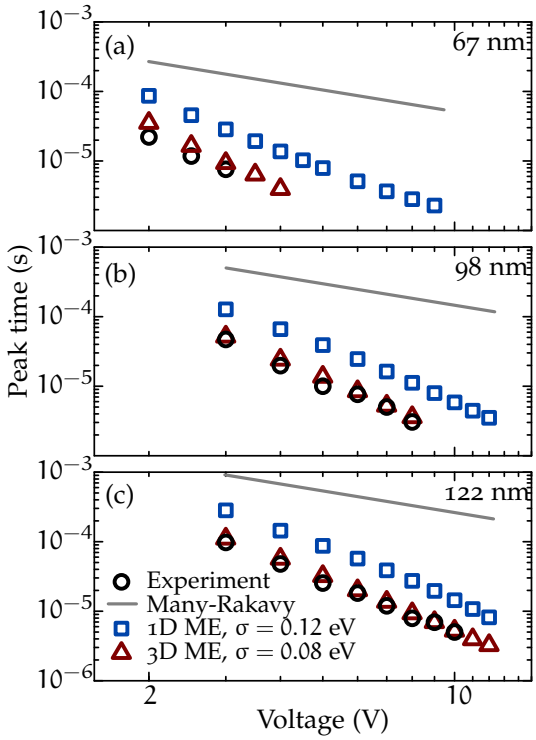

Figure 3.4.: Peak times (see arrows in Figure 3.1 (c)) as a function of pulse amplitude of the DI transients for devices with different LEP-layer thicknesses in (a)-(c). Circles: experiments. Gray lines: Many-Rakavy theory.[126] Squares: 1D ME modeling results with $\sigma = 0.12\,\text{eV}$. Triangles: 3D ME modeling results with $\sigma = 0.08\,\text{eV}$. The 3D ME transients with $\sigma = 0.12\,\text{eV}$ do not show a peak (see Figures 3.1 (c) and 3.2). In addition to the transients shown in Figure 3.2 also the peak times of transients at other pulse amplitudes were included.

the correct peak times: they are more than an order of magnitude too large and their voltage dependence is too weak. This is not a surprise, because the Many-Rakavy does not take into account the mobility-enhancing effects of non-zero carrier densities and electric fields.

Including the time dependence, the DI transients can be obtained with the 1D ME approach, using the parameters in Table 3.1, with, in particular, a disorder strength $\sigma = 0.12\,\text{eV}$. The results are plotted in Figures 3.1 (c) and 3.2, (blue dotted lines), and the resulting peak times are plotted in Figure 3.4 (blue squares). Three observations can be made: (1) the prediction of the peak times is considerably improved with respect to the Many-Rakavy theory, but they are still about a factor of three too large, (2) the voltage dependence of the peak times is right, (3) however, the shape of the transients is not in agreement with exper-

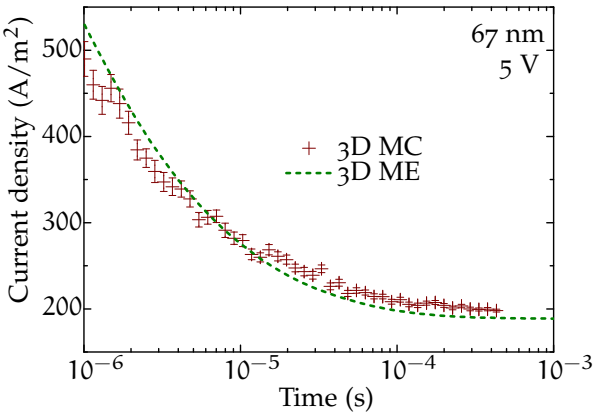

Figure 3.5.: Comparison of the DI transient obtained with the 3D ME approach with that obtained with the 3D Monte Carlo (3D MC) approach, for the device with $L = 67\,nm$, a pulse amplitude of $5\,V$, and $\sigma = 0.12\,eV$. The load resistance is not included. The error bars in the 3D MC results are shown. In the 3D MC simulations explicit effects of Coulomb interactions between the charge carriers are included, but not in the 3D ME calculations. No shoulder is in this case visible in the transients.

iment; in particular, the predicted structures (the depression before the peak and the peak itself) are too pronounced. The dependence of the mobility on carrier concentration and electric field in the 1D ME approach has led to an improvement as compared to the Many-Rakavy theory, but the agreement with experiment is still far from satisfactory. The still too large peak times should be attributed to the absence of carrier relaxation. At the start of the voltage pulse, carriers with high energy are injected into the device that initially have a larger mobility than when they have relaxed. This effect is not accounted for in the 1D ME approach.

With the 3D ME approach these carrier-relaxation effects are included. The green dashed lines in Figures 3.1 (c) and 3.2 show the transients obtained with the 3D ME approach, using the parameters in Table 3.1. Instead of showing a maximum, the transients show a continuous decrease, with sometimes a shoulder present (indicated by the circle in Figure 3.1 (c), but not visible in all transients of Figure 3.2) at a time that may be better in agreement with the experimental peak time than the peak time obtained with the 1D ME approach. Nevertheless, it is clear that with the value $\sigma = 0.12\,eV$ from Table 3.1, the agreement with experiment is still not satisfactory.

In order to check a possible failing of the 3D ME approach due to its neglect of explicit Coulomb interactions, we made a comparison with 3D MC simulations. It turned out to be feasible to perform 3D MC simulations of the DI transients

for the thinnest device with $L = 67\,\text{nm}$ at a relatively high pulse amplitude of 5 V. The comparison with the 3D ME transients is shown in Figure 3.5. The agreement is very good, from which we can conclude that the 3D ME transients are reliable. For thicker devices and lower voltages the charge-carrier density will only be smaller, so that the effects of Coulomb interactions will be even smaller. We note that there is now no shoulder visible in the transients. The reason is the relatively large voltage over a thin device that we had to use in order to reach a sufficiently large signal-to-noise ratio in the MC simulations. This washes out structures in the transients.

We attribute the disappearance of the peak in the DI transients calculated with the 3D ME approach for $\sigma = 0.12\,\text{eV}$ to too strong dispersive effects in the calculations. Dispersive transport leads to a spread in carrier transit times that will wash out features in the transients. To investigate this we decided to deviate from the value of σ found from the fitting of the 1D ME J-V curves and to explore lower values of σ that lead to less dispersion. We tried values of σ between 0.01 and 0.13 eV in steps of 0.01 eV and found that with $\sigma = 0.08\,\text{eV}$ the DI transients agree quite well with experiment (red dash-dotted lines in Figures 3.1 (c) and 3.2), with peak times (red triangles in Figure 3.4) that accurately follow the experimental peak times. Since a smaller σ requires an adjustment of the intrinsic hopping rates ν_0 in Eq. (1.10) to arrive at the same mobility we adjusted these rates to obtain a best fit of the 3D ME J-V curves (red dash-dotted lines in Figure 3.3) to the measured curves. The new values found for ν_0 are given in the bottom part of Table 3.1. We observe from Figure 3.3 that the J-V curves obtained with $\sigma = 0.8$ eV still agree quite well with the experimental curves. Hence, a consistent picture seems to emerge from this analysis.

3.5 SUMMARY, DISCUSSION, AND CONCLUSION

We performed and analyzed room-temperature dark-injection (DI) experiments on hole-only devices of a polyfluorene-based polymer with three different layer thicknesses. The current-density voltage (J-V) characteristics of these devices have been thoroughly investigated in terms of the extended Gaussian disorder model (EGDM). The DI transients show a peak that signals the arrival at the collecting contact of carriers injected by the injecting contact at the moment of the onset of a voltage pulse. A one-dimensional master-equation (1D ME) approach that takes into account the dependence of the mobility on the carrier density and electric field provides an improvement of the prediction of the time at which the peak appears over the Many-Rakavy theory, which assumes a constant mobility. The used parameters are obtained from fits to the J-V characteristics. Because carrier-relaxation effects are not included in the 1D ME

approach, the peak time is still significantly too large. With a three-dimensional master-equation (3D ME) approach that does account for relaxation the peak changes into a shoulder that appears approximately at the experimental peak time. The disappearance of the peak is attributed to too strong dispersive effects caused by the energetic disorder. With a somewhat reduced disorder strength σ, from 0.12 to 0.08 eV, the peak reappears and occurs at the correct time for the investigated devices and pulse amplitudes, while a satisfactory fit to the J-V characteristics is still possible.

It is clear from this work that the investigation of non-stationary charge transport in DI experiments provides an angle of view on charge transport in disordered organic semiconductors that is complementary to that provided by the investigation of stationary transport in J-V characteristics. From both angles of view, information about the disorder strength σ is obtained. An important question is now which of the two obtained values of σ is the appropriate one: the value of 0.12 eV obtained from the J-V characteristics or the value of 0.08 eV that appears to be compatible with the DI transients?

A possible answer to this question is that both values of σ are valid, but apply to different parts of the density of states (DOS). It is possible that the assumption that the density of states can be described as a Gaussian with one standard deviation is too simple. In the stationary transport that determines the J-V characteristics charge carriers have relaxed and probe the tail of the DOS, while during the relaxation in the non-stationary DI experiments charge carriers probe a much larger part of the DOS. This could lead to different apparent values of σ.

Another possible answer is that the value $\sigma = 0.08\,\text{eV}$ obtained from the DI experiments is the appropriate one. We have seen (Figure 3.3) that also with this value a very satisfactory description of the J-V characteristics of the three devices can be obtained at room temperature. However, the larger value $\sigma = 0.12\,\text{eV}$ is compatible with the temperature dependence of the mobility,[118] which was modeled by a factor $\exp\left[-C\,(\sigma/k_BT)^2\right]$, with a value $C = 0.39$ that falls in the range of $C = 0.38$ to 0.46, expected for disordered organic semiconductors.[131] In contrast, for $\sigma = 0.08\,\text{eV}$ the value needed for C (≈ 0.9) would be considerably outside this range. A possible solution could be that the Miller-Abrahams hopping rate Eq. (1.10) is inappropriate. It was found that with Marcus hopping rates, which could be more appropriate in systems with considerable reorganization of the nuclear system upon charging or decharging, the temperature dependence can also be described by a factor $\exp\left[-C\,(\sigma/k_BT)^2\right]$, but with a value of C that depends on the reorganization energy and can exceed the range mentioned above.[50]

The main conclusion of this work is that the consideration of relaxation effects in disordered organic semiconductors in dark-injection experiments provides an important additional tool to investigate charge transport in these semiconductors and has reopened the discussion about the appropriate model for charge transport.

4

STUDY OF CHARGE-CARRIER RELAXATION IN A DISORDERED ORGANIC SEMICONDUCTOR BY SIMULATING IMPEDANCE SPECTROSCOPY*

ABSTRACT Impedance spectroscopy is a very sensitive probe of nonstationary charge transport governed by charge-carrier relaxation in devices of disordered organic semiconductors. We simulate impedance spectroscopy measurements of hole-only devices of a polyfluorene-based disordered organic semiconductor by solving a time-dependent three-dimensional master equation for the occupational probabilities of transport sites in the semiconductor. We focus on the capacitance-voltage characteristics at different frequencies. In order to obtain good agreement with the measured characteristics we have to assume a lower strength of a Gaussian energy disorder than obtained from best fits to the stationary current density-voltage characteristics. This lower disorder strength is in agreement with dark-injection studies of nonstationary charge transport on the same devices. The results add to solving the puzzle of reconciling nonstationary with stationary charge-transport studies of disordered organic semiconductors.

* This chapter is based on the work that has been published: M. Mesta, J. Cottaar, R. Coehoorn, and P.A. Bobbert, *Appl. Phys. Lett.* 104, 213301 (2014).

4.1 INTRODUCTION

In order to improve the performance of organic semiconductor devices such as organic light-emitting diodes (OLEDs), organic field-effect transistors (OFETs), and organic photovoltaic cells (OPVCs), a thorough understanding of charge transport properties of organic semiconductors is crucial. In the amorphous organic-semiconductor thin films in these devices the disorder plays an important role. Stationary charge transport in disordered organic semiconductors has been studied to great depth, both experimentally and theoretically. Energetic disorder gives rise to a strong temperature, T, electric field, F, and charge-carrier density, n, dependence of the charge-carrier mobility μ, which is determined by the shape of the density of states (DOS).[45,61,78,79,132] Nonstationary transport in organic devices, for which the stationary mobility function cannot be used, has not yet been studied to equal depth. An important question, addressed in this chapter, is whether our understanding of nonstationary charge transport in these semiconductors can be reconciled with that of stationary transport.

In Chapter 3 we showed how to measure and simulate dark-injection (DI) current transients of hole-only devices of a polyfluorene-based light-emitting polymer (LEP). In DI experiments a device that is kept in the dark is brought into a state of nonstationary charge transport by a sudden step in the applied voltage. The simulations were performed by solving a time-dependent three-dimensional master equation (3D ME) for the occupational probabilities of sites representing localized states in the LEP. The temperature- and thickness-dependent stationary current density-voltage, J-V, characteristics of these devices had been analyzed before and a very good description was obtained within the extended Gaussian disorder model (EGDM) for the mobility function,[79] using a standard deviation $\sigma = 0.13\,\mathrm{eV}$ of the Gaussian density of states.[62,133,134] However, a proper modeling of the DI transients could only be obtained with a reduced value $\sigma = 0.08\,\mathrm{eV}$. This has brought up the important question whether our understanding of charge transport in disordered organic semiconductors is really complete.

Another important technique to study non-stationary transport in organic devices is impedance spectroscopy. In this technique a dc bias V is applied over a device and on top of that a small ac component $\Delta V(t) = \Delta V \sin(2\pi f t)$. The impedance $Z = Z' + iZ''$ is defined as the zero-amplitude limiting value of the ratio of $\Delta V(t)$ and the response $\Delta I \exp[2\pi i(f + \phi)t]$ in the current, with ϕ a phase difference. In particular, we will be interested in the capacitance-voltage, C-V, characteristics, with the capacitance given by $C = -Z''/2\pi f|Z|^2$. Impedance spectroscopy can be fruitfully used to distinguish different trapping regimes in single-carrier organic-semiconductor

devices[127] and to determine doping densities and built-in voltages in organic solar cells[135].

Modeling of the C-V characteristics with the static mobility function neglects the effects of carrier relaxation in the DOS. Recently, Germs et al.[87] developed a multiple-trapping model for this carrier relaxation that is based on the existence of a conduction-level energy E_c. The idea is that the fraction of carriers around this energy in the DOS determines the conduction. Extra carriers induced by the fluctuating voltage slowly relax from this energy towards their equilibrium distribution. It was found that with a value $E_c = -0.75\sigma$ and the EGDM mobility function for the fraction of carriers at the conduction-level energy a fair description of the C-V characteristics at different frequencies of the polyfluorene-based hole-only devices could be obtained with $\sigma = 0.13\,\mathrm{eV}$[87]. However, E_c was essentially treated as a fit parameter in the modeling, so that hard conclusions about the comparison between stationary and nonstationary charge transport could not be drawn.

In this chapter we follow the same methodology as in our modeling of DI transients[136] and simulate the impedance spectroscopy experiments by explicitly solving a time-dependent 3D ME for a lattice of transport sites representing a complete device. The great advantage of this methodology is that it does not suffer from simplifications inherent to one-dimensional (1D) modeling and provides information at the microscopic level. Like in the modeling of DI transients, this makes a direct comparison between stationary and nonstationary charge transport possible.

4.2 NUMERICAL METHODS

The time-dependent 3D ME for the occupational probabilities p_i of sites i in the device is given by Equation 2.22. We follow the iterative scheme that is described in Section 2.2 in finding the steady-state solution of Equation 2.22: $\mathbf{p}_0$ for $dp_i/dt = g_i(\mathbf{p}) = 0$ at the applied static voltage V. Since a small-amplitude ac-signal with the frequency f induces a small change $\Delta\mathbf{p}$, we write $\mathbf{p}(t) \approx \mathbf{p}_0 + \exp(2\pi i f t)\,\Delta\mathbf{p}$ and $\mathbf{g}(\mathbf{p}) \approx \mathbf{g}(\mathbf{p}_0) + \exp(2\pi i f t)\,[\Delta V\,\partial\mathbf{g}/\partial V + \mathbf{J}\Delta\mathbf{p}]$, with the matrix elements of the Jacobian $\mathbf{J}$ given by Equation 2.30. Substituting these expressions in Equation 2.22 and linearizing leads to the matrix relation

$$(2\pi i f\mathbf{I} + \mathbf{J})\,\Delta\mathbf{p} = -\Delta V\frac{\partial\mathbf{g}}{\partial V}, \tag{4.1}$$

with $\mathbf{I}$ the identity matrix. Equation 4.1 can be solved for $\Delta\mathbf{p}$ and from this the current change ΔI is obtained from Eq. 3.5. The capacitance C is then calculated as explained above from the impedance Z. Like in Ref. 136 we

draw the site energies from a Gaussian DOS with standard deviation σ and assume a Miller-Abrahams hopping rate[65] (Equation 1.10). We assume that the hopping takes place between nearest neighbors. We use a simple cubic (SC) as well as a face-centered cubic (FCC) lattice in our simulations. It is convenient to include the constant factor $\exp(-2\alpha a_{nn})$, with a_{nn} the nearest-neighbor distance, in the prefactor of the Miller-Abrahams rate Equation 1.10 and define this prefactor as $w_0 \equiv \nu_0 \exp(-2\alpha a_{nn})$.

4.3 RESULTS AND DISCUSSION

We performed simulations for the same two devices as studied in Ref. 87. They have the structure glass, indium tin oxide (100 nm), PEDOT:PSS (100 nm), LEP, Pd (100 nm). The LEP consists of polyfluorene with copolymerized triarylamine units (7.5 mol%) for hole transport; see Figure 4.1 (a). The LEP-layer thicknesses are $L = 97$ and 121 nm for the two devices and their areas are $A = 9 \times 10^{-6}\,m^2$. No injection barrier is taken at the anode (PEDOT:PSS) and injection barriers of 1.65 and 1.90 eV are taken at the cathode (Pd) for the $L = 97$ and $L = 121$ nm device, respectively, according to EGDM modeling studies of the J-V characteristics of these devices.[62,130] These modeling studies gave best fits for the J-V characteristics with $\sigma = 0.13$ eV. The relative dielectric constant of the LEP is $\epsilon_r = 3.2$.[62] The simulation boxes have dimensions $L \times L_y \times L_z$, with $L_y = L_z = 50\,a$ and periodic boundary conditions in the y- and z-direction, yielding a sufficient lateral averaging.

Figure 4.1 (b) gives an overview of our main results for the C-V characteristics of the $L = 121$ nm device at a frequency $f = 100$ Hz and room temperature (295 K). We distinguish four regimes.

1) At low voltage all curves converge to the geometrical capacitance, because the number of holes present in the device close to the injecting electrode is then still limited.

2) With increasing voltage, a sheet of holes builds up by diffusion at the anode, but these cannot yet move to the cathode because the electric field is still directed from cathode to anode. As a result, the capacitance rises.

3) When approaching the built-in voltage V_{bi} (1.9 V in this case) these holes start to move to the cathode, leading to a decrease of the capacitance. The result is a peak in the C-V curve before V_{bi} is reached.[137]

4) Beyond V_{bi} a regime starts where the experimental C-V curve rises again and where the different modeling results predict very different behavior. It is this regime we want to focus on.

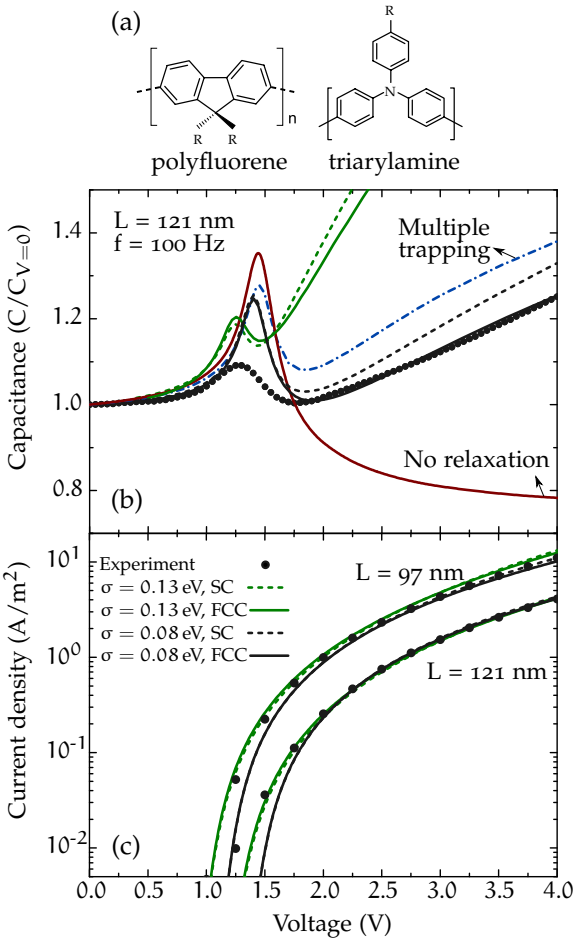

Figure 4.1.: (a) Schematic structure of the polyfluorene-triarylamine copolymer, (b) capacitance C, normalized to its value at $V = 0$, as a function of V at a frequency $f = 100\,\text{Hz}$ and temperature $T = 295\,\text{K}$ for a hole-only device with a layer with thickness $L = 121\,\text{nm}$. Dots: measurements.[87] Red line: 1D DD calculation with an EGDM mobility function for $\sigma = 0.13\,\text{eV}$, neglecting relaxation. Dash-dotted blue line: multiple-trapping result.[87] (c) Current density-voltage, J-V, characteristics of the $L = 121$ and $L = 97\,\text{nm}$ device at $T = 295\,\text{K}$. Dots: measurements.[136] Green lines in both (b) and (c): 3D ME simulations for $\sigma = 0.13\,\text{eV}$. Black lines: 3D ME simulations for $\sigma = 0.08$. Dashed (full) green and black lines: SC (FCC) lattice.

The red curve in Figure 4.1 (b) is a modeling result in which a time-dependent one-dimensional drift-diffusion (1D DD) equation is solved with the EGDM mobility function for $\sigma = 0.13\,\text{eV}$.[87] This model assumes that the mobility at

Table 4.1.: Values for the hopping prefactor $w_0 \equiv \nu_0 \exp(-2\alpha a_{nn})$, with a_{nn} the nearest-neighbor distance, in the Miller-Abrahams rate Equation 1.10 obtained from fits to the measured J-V curves of Figure 4.1 (c).

σ [eV]	w_0 [s^{-1}]	
	SC	FCC
0.13	2.7×10^{10}	3.2×10^{9}
0.08	9.1×10^{7}	2.2×10^{7}

any moment in time is given by the instantaneous carrier density and electric field through this function, and therefore does not account for carrier relaxation. At high voltages the curve deviates strongly from experiment, which should be attributed to the neglect of relaxation. The dash-dotted blue curve is the result of the multiple-trapping model for relaxation, assuming a conduction-level energy $E_c = -0.75\sigma$. The agreement with experiment is in this case fair, not only at the frequency $f = 100\,\text{Hz}$, but also at the other frequencies investigated in Ref. 87 (not shown here).

However, the C-V curves obtained from the 3D ME simulations for $\sigma = 0.13\,\text{eV}$ do not agree at all with experiment. The dashed green curve gives the result obtained for a SC lattice, with a lattice constant $a = 1.19\,\text{nm}$. The latter value was obtained from the value $N_t = 6 \times 10^{26}\,\text{m}^{-3} = 1/a^3$ for the density of transport sites found in the modeling studies of Ref. 62, a value that is compatible with the known density of $1.8 \times 10^{26}\,\text{m}^{-3}$ of triarylamine units in the used copolymer. The effects of carrier relaxation are clearly too strong in this case.

In Figure 4.1 (c) we compare the corresponding result for the J-V curve with experiment, leading to an excellent agreement. The value of the hopping prefactor w_0 found from this comparison is given in Table 4.1. We conclude that there is a strong discrepancy between the description of the stationary charge transport reflected by the J-V curve and the nonstationary charge transport reflected by the C-V curve.

One may argue that carrier relaxation could depend on the type of lattice and in particular on the number of nearest neighbors. To investigate this we also performed simulations for an FCC lattice with a lattice constant of $a = 1.88\,\text{nm}$, corresponding to the same site density as in the SC lattice, but with 12 instead of 6 nearest neighbors. It was found from numerical calculations that the critical energy for percolation within the EGDM is significantly lower for an FCC than for a SC lattice, due to the larger number of nearest neighbors[50]. One may wonder if this could mean that also the conduction level energy E_c is lower, leading to weaker relaxation effects. Figure 4.1 (c) shows that again excellent agreement is obtained with the experimental J-V curve, with an adapted value

of w_0 given in Table 4.1. The full green curve in Figure 4.1 (b) is the C-V result for this case. This curve lies only slightly below the curve for the SC, from which we conclude that the type of lattice only has a minor influence on relaxation.

In the modeling of DI transients in Chapter 3 and Ref. 136 it was also found that unsatisfactory agreement with experiment was found when taking the same value for σ in the DI modeling as in the modeling of the J-V curves. Reducing the value of σ to 0.08 eV, however, led to a very good agreement. We tested whether taking this reduced value of σ leads also to an improvement in the modeling of the C-V curves. To this end, we first refitted the J-V curves with $\sigma = 0.08$ eV. Figure 4.1 (c) shows that very satisfactory fits are obtained at higher voltages, both for the SC and FCC lattice. Only at low voltages (< 2 V) the fits are inferior to those with $\sigma = 0.13$ eV. The results obtained for w_0 are again given in Table 4.1. Figure 4.1 (b) shows that indeed the C-V curves are now in very good agreement with experiment, with the FCC curve even falling on top of the experimental curve for voltages > 2 V. The only clear disagreement is in the peak, which is more pronounced in the modeling than in the experiment. In Ref. 87 it was suggested that lateral variations in V_{bi} will lead to widening of the experimental peak, which may partially explain the disagreement.

Figure 4.2 shows comparisons between experimental and simulated C-V curves for $\sigma = 0.08$ eV and for both SC and FCC lattices, at frequencies of 100, 250, and 1000 Hz, for the $L = 97$ nm (Figure 4.2 (a)) and $L = 121$ nm (Figure 4.2 (b)) device. The conclusion is that the overall agreement is very satisfactory. At the highest frequency of 1000 Hz relaxation effects are the least significant. This can be understood from Equation 4.1, in which at high frequency f the first, "direct", term on the left-hand side becomes dominant with respect to the second, "indirect", term, which accounts for the relaxation effects.

To exclude the possibility that the obtained agreement with the experimental C–V curves using $\sigma = 0.08$ eV is fortuitous we considered other factors that could influence carrier relaxation. Specifically, we looked at variable-range instead of nearest-neighbor hopping and Marcus[138] instead of Miller-Abrahams hopping rates. In the case of variable-range hopping (VRH) we should specify the inverse wave function decay length α in the prefactor $\exp(-2\alpha R_{ij})$ in Equation 1.10. We have no information about α for our case, but taking $\alpha = 4/a$ leads to considerable rates for further than nearest-neighbor hops. For this value and taking hopping up to the fourth nearest-neighbor into account on an SC lattice we found that some effect of VRH is visible on the C-V curves at high voltage, but the effect is significantly smaller than the difference between the results for $\sigma = 0.13$ and 0.08 eV in Figure 4.1 (b). Regarding Marcus hopping rates it has been found that the mobility function and hence the stationary charge transport is not significantly different than for Miller-Abrahams

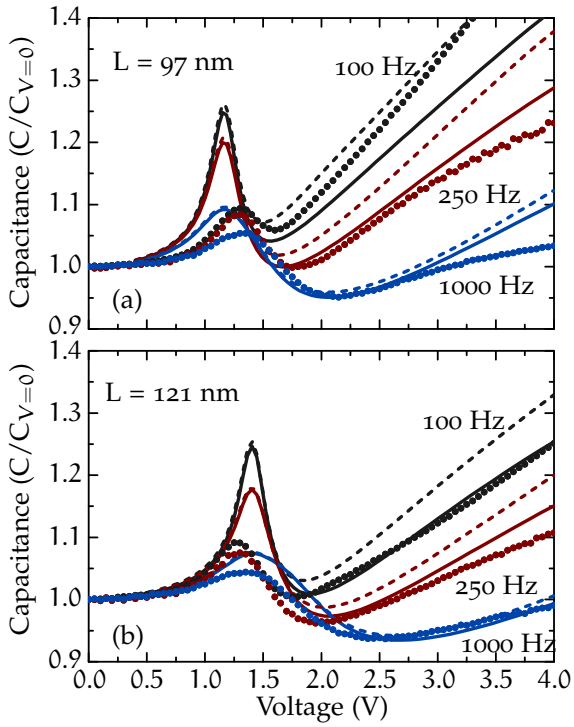

Figure 4.2.: Capacitance C, normalized to its value at V = 0, as a function of V at different frequencies for (a) the L = 97 nm and (b) the L = 121 device. Dots: measurements.[87] Full (dashed) lines: simulation results for σ = 0.08 eV and a SC (FCC) lattice.

hopping rates[50], but it is not a priori clear that the same holds for carrier relaxation. Information about the reorganization energy E_r in the Marcus hopping rate is lacking in our case. Our master-equation solver allowed the study of Marcus hopping on an SC lattice for reorganization energies down to $E_r \approx 3\sigma$. For all considered cases we found that the difference with Miller-Abrahams hopping rates is small.

The puzzling question remains why there is such a discrepancy between the description of stationary and nonstationary charge transport. A possible explanation was suggested in Chapter 3 and Ref. 136: maybe in the stationary transport the low-energy tail of the DOS is important, represented by a relatively large σ, while in nonstationary transport relaxing carriers probe a larger part of the DOS, represented by a smaller σ. In other words, the shape of the DOS could be more complicated than a single Gaussian. This explanation seems to be corroborated by the J-V curves in Figure 4.1 (c). At low voltage, σ = 0.13 eV gives a better description, while at higher voltage σ = 0.08 eV gives

an excellent and even a slightly better description. A value of $\sigma = 0.13\,\mathrm{eV}$ at low voltage could also explain the lower peak in the C-V curve as compared to the simulations with $\sigma = 0.08\,\mathrm{eV}$ in Figures 4.1 (b) and 4.2. We remark here that the positions of the peak could be improved by adapting the built-in voltages V_{bi} used in the calculations. We recall that these voltages were obtained from an EGDM fit of the J-V characteristics with $\sigma = 0.13\,\mathrm{eV}$, but the obtained values are probably not optimal for $\sigma = 0.08\,\mathrm{eV}$.

It was remarked in Chapter 3 and Ref. 136 that a single-Gaussian DOS with $\sigma = 0.08\,\mathrm{eV}$ will lead to a temperature dependence of the mobility in the limit of vanishing carrier density that is too weak as compared to experiment. In the scenario of a more complicated DOS sketched here, however, it would be the value $\sigma = 0.13\,\mathrm{eV}$ that determines the temperature dependence in this limit, which is known to lead to a good agreement with experiment.[62] We suggest that other types of experiments are performed on our system that can more directly probe the shape of the DOS. Specifically, we think of thermally stimulated current (TSC) measurements, which have originally been used to extract information about trap levels,[139–141] but could also be employed more generally to study DOS tails.

5

MOLECULAR-SCALE SIMULATION OF ELECTROLUMINESCENCE IN A MULTILAYER WHITE OLED*

ABSTRACT In multilayer white OLEDs the electronic processes in the various layers –injection and motion of charges as well as generation, diffusion, and radiative decay of excitons– should be concerted such that efficient, stable, and colour-balanced electroluminescence occurs. We show that it is feasible to carry out Monte Carlo simulations including all these molecular-scale processes, as demonstrated for a hybrid multilayer OLED combining red and green phosphorescent layers with a blue fluorescent layer. The simulated current density and emission profile agree well with experiment. The experimental emission profile was obtained with nanometer resolution from the measured angle- and polarization-dependent emission spectra. The simulations elucidate the crucial role of exciton transfer from green to red and the efficiency loss due to excitons generated in the interlayer between the green and blue layer. The perpendicular and lateral confinement of the exciton generation to regions of molecular-scale dimensions, revealed by this study, demonstrate the necessity of molecular-scale instead of conventional continuum simulation.

* This chapter is based on the work that has been published: M. Mesta, M. Carvelli, R. J. de Vries, H. van Eersel, J. J.M. van der Holst, M. Schober, M. Furno, B. Lüssem, K. Leo, P. Loebl, R. Coehoorn, and P.A. Bobbert, *Nature Mater.*, 12(7), 652 (2013)

5.1 INTRODUCTION

Organic light-emitting diodes (OLEDs) hold great promise for energy-efficient light sources with unique properties. In contrast to inorganic LEDs they have a large light-emitting area and can be fabricated on flexible substrates. The development of white OLEDs for lighting applications is particularly challenging, since these require the combination of emitters of different colors. They should function such that 1) electrical energy is efficiently converted into light, 2) the right colour balance is obtained, and 3) long-term stability of the efficiency and color balance is guaranteed. A well-established strategy to achieve these goals is the use of multilayer stacks, where each layer performs a specific function[142]. Control of all the electronic processes occurring in such stacks –injection and transport of charges as well as generation, diffusion, and radiative decay of excitons– is necessary, but at the same time extremely complex. The development of predictive modeling of these processes is imperative, but has not yet been realized.

The efficiency of white OLEDs has been increased by introducing highly n- and p-doped organic-semiconductor layers at the injecting contacts in combination with layers transporting electrons and holes to the emission layers[143], and phosphorescent triplet emitters harvesting almost all singlet and triplet excitons formed in the emission layers[30]. Full-phosphorescent OLEDs use red, green, and blue triplet emitters, and are among the most efficient[10]. An issue with these OLEDs, however, is the long-term instability of the available blue triplet emitters. Therefore, most present commercial white OLEDs are hybrid, generating the blue component of the emitted light by fluorescence[144,145]. Nevertheless, long-term stability of OLEDs remains a concern and it is of utmost importance to identify causes for their degradation.

Charge transport in the organic semiconductors used in OLEDs occurs by hopping between sites with an energy disorder that is often taken to be Gaussian[43]. Advanced OLED simulation methods have been developed based on this concept that treat the device as a continuous one-dimensional (1D) system, with properties depending only on the distance to the electrodes[79,83,146,147]. For a single-layer OLED with a thick organic layer such a method was applied with considerable success[147]. In white OLED stacks, molecular-scale inhomogeneities in the stacking direction caused by sublayer thicknesses of only a few molecular diameters prevent the use of these methods. 1D approaches with discretization in the stacking direction[129,148] would then be more appropriate. However, these cannot capture the lateral molecular-scale inhomogeneities in the exciton generation revealed by the present study.

Here, we carry simulation of OLED electroluminescence to a next level by presenting the first three-dimensional (3D) molecular-scale Monte Carlo simula-

tions of all relevant electronic processes in a white OLED. Apart from charge injection, charge transport, and exciton formation, the simulations contain for the first time effects of 3D exciton diffusion. As demonstration and validation we apply the simulations to a white hybrid OLED stack that we have fabricated. We compare the simulation results for the current-voltage characteristics and the emission profile to experiments on this stack. The results provide a unique view on where and how luminescence occurs, on molecular-scale inhomogeneities in the exciton generation, on efficiency-loss processes, and on possible causes for degradation. The range of applicability of the developed simulation tools is broad and we foresee their use in future optimized OLED stack design.

5.2 THE OLED STACK: ELECTRICAL AND OPTICAL CHARACTERISTICS

Figure 5.1 (a) shows the schematic layer structure of the investigated OLED stack and the materials used in the different layers (see Appendix A for its fabrication). Its working principle is as follows. Holes reach the inner part of the stack by injection from an ITO layer into a p-doped injection layer and transport through a hole-transporting and electron-blocking layer of α-NPD, and electrons do so by injection from an aluminium cathode into an n-doped electron-injection layer and transport through an electron-transporting and hole-blocking layer of NET5. In the inner part of the stack, blue light is generated in a fluorescent Spiro-DPVBi layer adjacent to the NET5 layer. Green light is generated in a TCTA layer doped with the green phosphorescent dye $Ir(ppy)_3$ and red light in an α-NPD layer doped with the red phosphorescent dye $Ir(MDQ)_2(acac)$.

The green phosphorescent layer is separated from the blue fluorescent layer by an interlayer consisting of a mixture of an electron and a hole transporter, TPBi and TCTA, respectively. The purpose of this interlayer is twofold[144]. Firstly, it blocks the transfer of singlet excitons from the blue to the green layer and of triplet excitons from the green to the blue layer (Spiro-DPVBi has a triplet energy lower than that of $Ir(ppy)_3$). Secondly, the interlayer allows passage of electrons from the blue to the green layer and of holes from the green to the blue layer. There is no equivalent interlayer between the green and red phosphorescent layers. Therefore, triplet excitons can diffuse from the green to the red layer and this is in fact an important process in establishing the right color balance.

The measured room-temperature current density-voltage characteristic of the OLED is shown in Figure 5.1 (b). At a bias around 2.5 V the OLED switches on

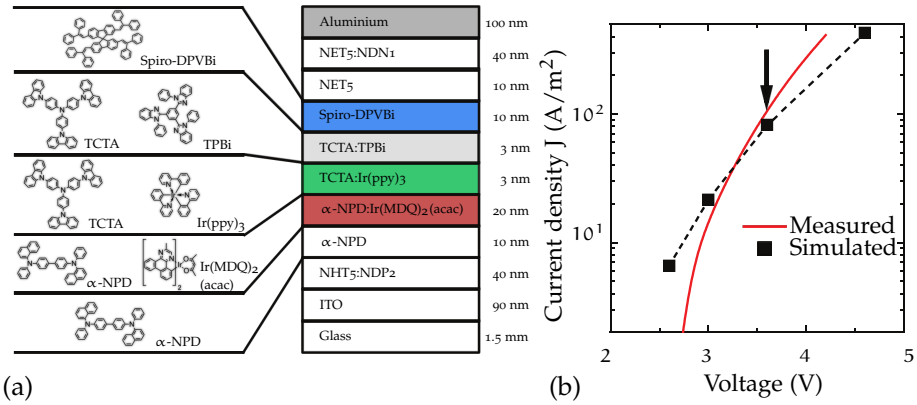

Figure 5.1.: OLED stack and its electrical characteristics. (a) Layer structure of the hybrid OLED stack studied in this work (surface area: 2.7 by 2.5 mm). The layers and the used organic materials are, from bottom to top: p-doped hole-injecting layer of NHT5 with 4 mol% NDP2 [149], hole-transporting layer of N,N′-di(naphthalen-1-yl)-N,N′-diphenyl-benzidine (α-NPD), layer of α-NPD with 5 mol% of the red phosphorescent dye (acelylacetonate)bis(2-methyldibenzo[f,h]quinoxinalate)iridium ($Ir(MDQ)_2(acac)$), layer of 4,4′,4"-tris(N-carbazoyl)-triphenylamine (TCTA) with 8 mol% of the green phosphorescent dye factris(2-phenylpyridyl)iridium ($Ir(ppy)_3$), interlayer consisting of a mixture of the hole transporter TCTA with 33 mol% of the electron transporter 1,3,5-tris(N-phenylbenzimidazol-2-yl)benzene (TPBi), blue fluorescent layer of 2,2′,7,7′-tetrakis(2,2-diphenylvinyl)Spiro-9,9′-bi fluorene (Spiro-DPVBi), electron-transporting layer of NET5 [149], and n-doped electron-injecting layer of NET5 with 4 mol% NDN1 [149]. (b), Measured (full) and simulated (symbols, error: ~10%, and dashed curve as guide to the eye) current density-voltage characteristics. The arrow indicates the current density-voltage point at which most reported experimental and simulation studies were performed.

and the current is measured up to 4.2 V. At higher voltages, there is a risk of permanently damaging the OLED by excessive heating. Unless stated otherwise, for all other presented results the bias is 3.6 V. The CIE 1931 color point of the perpendicularly emitted light at this bias was measured to be $[x, y] = [0.47, 0.45]$. It corresponds to warm-white emission, slightly shifted to the yellow/orange. The external quantum efficiency (EQE) –the fraction of emitted photons per injected electron-hole pair– is $5 \pm 1\%$, as measured in an integrating sphere setup.

The color-resolved emission profile of the OLED is shown in Figure 5.2 (a). The profile was reconstructed from the measured angle and polarization dependent

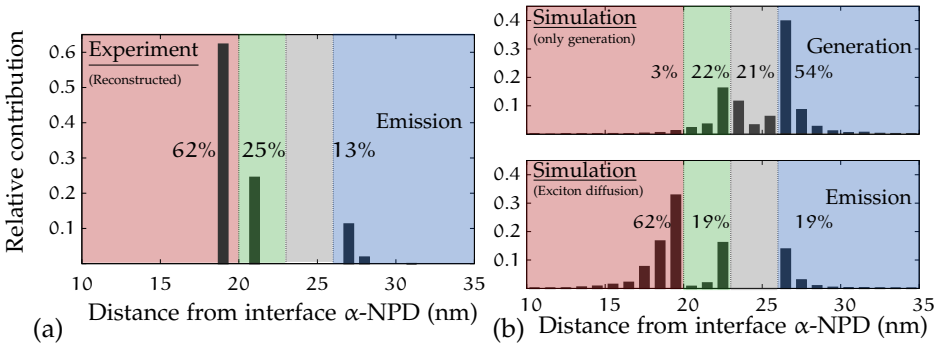

Figure 5.2.: Light-emission and exciton-generation profiles. (a), Reconstructed experimental light-emission profile. (b), Simulated exciton-generation (top) and light-emission (bottom) profile, with the difference caused by excitonic processes. The numbers indicate the fractions in the various layers (errors: ~1% or smaller).

emission spectra, as pioneered in Ref. 150 for a single-layer OLED and here applied for the first time to an OLED stack (see Appendix A). The nanometer-scale resolution of the reconstruction method fully pays off in the present context, since the emission occurs in each layer in a region of only a few nanometers thick. In the blue layer, the emission occurs close to the interface with the interlayer. Detailed resolution of the emission profile within the very thin green layer (3 nm) is beyond the accuracy of the reconstruction method. The emission from the red layer occurs close to the interface with the green layer and can be due to excitons generated in this layer as well as to exciton transfer from the green to the red layer. The emission percentages in the different emission layers are indicated in the figure. Almost no dependence of the color point and reconstructed emission profile on the bias was found in a range of about 1 V around 3.6 V. Using the outcoupling properties of the stack, the expected color point was calculated from the reconstructed emission profile. The result, again $[0.47, 0.45]$, perfectly agrees with the directly measured color point, demonstrating the internal consistency of the reconstruction procedure.

By using the radiative decay probabilities η_r of the different emitters, the reconstructed emission profile also allows a calculation of the expected EQE. We take $\eta_r = 0.35$ for the blue fluorescent emitter[151], and 0.84 and 0.76 for the red and green phosphorescent emitter in their respective hosts[152]. The exciton generation efficiency can be assumed to be unity because of the effective confinement of electrons and holes to the inner part of the stack by the charge-blocking layers. By assuming that in the blue fluorescent layer singlet and triplet excitons are generated in a quantum-statistical ratio of 1:3, and using the calculated light-outcoupling efficiency, we find an EQE of $9 \pm 1\%$. This is substantially

larger than the measured EQE of $5 \pm 1\%$, which indicates that, apart from the limited outcoupling efficiency ($20 \pm 1\%$), the quantum-statistically limited number of singlet excitons formed in the blue layer, and the limited radiative decay probabilities of the emitters, there are other factors that limit the efficiency of this OLED. Simulation of the electronic processes occurring in the OLED provides a unique tool to investigate this.

5.3 MONTE CARLO SIMULATION OF CHARGE AND EXCITON DYNAMICS

The feasibility of performing Monte Carlo simulations at the molecular level of charge injection and transport in single-layer single-carrier devices of disordered organic semiconductors has recently been demonstrated[48]. Here, we carry such simulations to a next level by applying them to the OLED stack of Figure 5.1 (a) and including exciton generation and diffusion (see Appendix A). The molecules in the stack are represented by point sites arranged on a cubic lattice with a lattice constant $a = 1$ nm, the typical intermolecular distance of the materials comprising the stack. We assume the presence of correlated disorder in the electron and hole energies, which was found to be present in various small-molecule materials[116,117]. The disorder is assumed to be caused by random dipoles and has a strength $\sigma = 0.1$ eV, corresponding to the value found for hole transport in α-NPD[116]. We expect that with this the hole transport in α-NPD is properly described and that also a reasonable description is obtained for the charge transport in the other materials in the stack. Red and green emitting guests are introduced according to the known concentration of the emitters, with appropriately adapted energy levels.

Electron traps are ubiquitous in organic semiconductors and are introduced in the layers in which electron transport is important: the blue fluorescent layer and the electron-transporting layer. Their presence is modeled using an exponential distribution of trap energies[153–155] with a concentration c_{trap} and a trap energy $k_B T_0$. Transport in electron-only devices of the electron transporter BAlq could be modeled well using correlated disorder with $\sigma = 0.09$ eV, $c_{trap} = 7 \times 10^{-4}$, and a trap temperature $T_0 = 1200$ K[117], demonstrating the applicability of our method of introducing traps in molecular semiconductors.

We take Miller-Abrahams rates for the nearest-neighbor hopping of charges on the lattice[65]. Modeling of charge transport in devices of small-molecule semiconductors based on these rates has been very successful[116,117]. It was recently demonstrated that the charge-transport properties found with these rates are very similar to those with the often used Marcus hopping rates[50] (the latter rates would require the introduction of another parameter, the reorganization energy[138]). The energy differences in the hopping rates contain, apart from the

Material	E_{HOMO} (eV)	E_{LUMO} (eV)	$\mu_{0,h}$ (m^2/Vs)	$\mu_{0,e}$ (m^2/Vs)	c_{trap}	T_0 (K)
NHT5:NDP2	−5.10					
α-NPD	−5.33	−2.23	6.0×10^{-9}	6.0×10^{-10}		
α-NPD	−5.43	−2.33	6.0×10^{-9}	6.0×10^{-10}		
$Ir(MDQ)_2(acac)$	−5.13	−2.93	6.0×10^{-9}	6.0×10^{-10}		
TCTA	−5.60	−2.20	2.0×10^{-8}	2.0×10^{-9}		
$Ir(ppy)_3$	−5.20	−2.70	2.0×10^{-8}	2.0×10^{-9}		
TCTA	−5.60	−2.20	2.0×10^{-8}	2.0×10^{-9}		
TPBi	−6.20	−2.60	2.0×10^{-8}	2.0×10^{-9}		
Spiro-DPVBi	−5.70	−2.80	6.0×10^{-9}	8.0×10^{-9}	0.001	2350
NET5	−6.00	−2.50	1.5×10^{-11}	1.5×10^{-10}	0.005	1400
NET5:NDN1		−2.50				

Table 5.1.: Material parameters: charge dynamics. HOMO and LUMO energies, room-temperature hole- and electron-mobilities $\mu_{0,h}$ and $\mu_{0,e}$ at low field and low carrier density, electron-trap concentration c_{trap}, and trap temperature T_0 of the trap distribution in the different layers of the stack, as used in the Monte Carlo simulations.

random site energies, an electrostatic contribution due to the bias applied to the OLED and the Coulomb energy due to all present charges. We treat the doped injection layers as metallic, injecting and collecting charges with an energy according to a given work function. Exciton generation occurs by hopping of an electron to a site where a hole resides, or vice versa.

In Table 5.1 we give the parameters of the stack materials as used in the simulations of the charge dynamics. Figure 5.3 pictures the level scheme of the centers of the HOMO (highest occupied molecular orbital) and LUMO (lowest unoccupied molecular orbital) energy distributions for holes and electrons. The parameters were determined from charge-transport and spectroscopic studies of the various materials. Appendix B contains a detailed explanation of how the parameters in Table 5.1 were obtained and Appendix C a sensitivity analysis of the simulation results to variations in these parameters.

Exciton diffusion within and in between the green and red layers is included in the simulations (see Appendix A). Because the red and green triplet emitters trap electrons as well as holes (see Figure 5.3), most excitons in the red and green layer are generated on the emitters. We describe the diffusion of excitons among the emitters by Förster transfer, made possible by mixing in of spin-singlet character into the exciton wave function due to the spin-orbit coupling of the heavy iridium atoms. The Förster transfer rate between two emitters i and j is[156]

$$k_{ij} = \frac{1}{\tau_{r,i}} \left(\frac{R_{0,ij}}{R} \right)^6 , \tag{5.1}$$

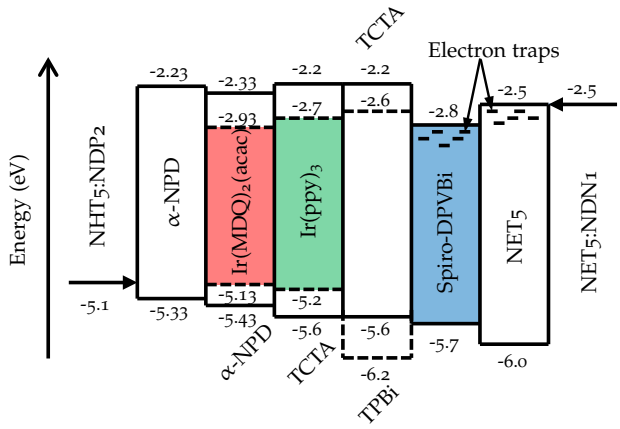

Figure 5.3.: Energy-level diagram. HOMO and LUMO energies in eV of the materials in the OLED stack of Figure 5.1 (a) as used in the simulations, in each case defined as the energy at the top of a Gaussian density of states with standard deviation $\sigma = 0.1$ eV. The horizontal arrows indicate the work functions used for the doped hole and electron injecting layers. The concentrations of the red and green dye are 5×10^{-2} and 8×10^{-2}, respectively. The electron traps in the Spiro-DPVBi and NET5 have concentrations of 10^{-3} and 5×10^{-3}, and trap energies of $k_B T_0 = 0.2$ and 0.12 eV, respectively.

with $\tau_{r,i}$ the radiative lifetime of emitter i, R the distance between the two emitters, and $R_{0,ij}$ the Förster radius for transfer from i to j. The latter accounts for the spectral overlap between the emission spectrum of i and the absorption spectrum of j. Apart from undergoing transfer, the excitons can decay radiatively with a rate $k_{r,i} = 1/\tau_{r,i}$, or non-radiatively with a rate $k_{nr,i} = 1/\tau_{nr,i}$. These rates are related to the radiative decay probabilities by $\eta_{r,i} = k_{r,i}/(k_{r,i} +$

Material	k_r (μs^{-1})	k_{nr} (μs^{-1})	R_o (nm)	E_T (eV)
$Ir(MDQ)_2(acac)$	0.588	0.112	1.5	2.0
$Ir(ppy)_3$	0.816	0.249	1.5	2.4

Table 5.2.: Material parameters: exciton dynamics. Radiative and non-radiative exciton decay rates k_r and k_{nr}, Förster radii R_0 for exciton transfer between triplet emitter molecules, and triplet energies E_T. For the green emitting $Ir(ppy)_3$ k_r and k_{nr} are taken from Ref. 157 while for the red emitting $Ir(MDQ)_2(acac)$ k_r is obtained from Ref. 158 and k_{nr} from η_r given in Ref. 152 and the relation $\eta_r = k_r/(k_r + k_{nr})$. A typical value is taken for the value of R_0 for transfer between the same emitter molecules from Ref. 156. For the transfer from a green to a red emitter we take $R_{0,GR} = 3.5$, according to the estimate in Ref. 159. The triplet energies are taken from Ref. 160.

$k_{nr,i}$). The parameters used in the exciton dynamics, taken from literature, are given in Table 5.2. The large Förster radius $R_{0,GR} = 3.5$ nm taken for transfer from green to red [159] reflects the large spectral overlap for this transfer. Transfer from red to green is neglected since it will only occur with a very small rate.

Simulation of exciton diffusion is performed for each exciton generated in the red or green layer and proceeds independently from all other processes, which means that exciton-exciton and exciton-charge interactions are neglected. The excitons generated on host sites in the red and green layer (a minority) are assumed to transfer instantaneously to triplet emitter guests in their neighborhood. Diffusion of excitons generated in the blue layer is not taken into account, because their diffusion length will be short and because transfer to the green layer is blocked by the interlayer. Excitons generated in the interlayer are assumed to be lost by non-radiative decay or emission outside the visible spectrum.

5.4 SIMULATION RESULTS: CURRENT DENSITY, EXCITON GENERATION, AND LIGHT EMISSION

The simulation results for the current density in the OLED at several voltages, using the parameters of Table 5.1, are given by the symbols in Figure 5.1 (b). The simulated current density curve is close to the measured one. We stress that the parameters of Table 5.1 come from separate studies of the materials or material combinations in the stack, so that the simulated current density can really be considered as a prediction. The overall agreement between the simulated and measured current density indicates that the charge transport through the stack is well described by the simulations. The larger experimental current density at high voltage could result from a heating effect. The discrepancy at low voltage could be due to a slight underestimation of the trapping of holes by $Ir(MDQ)_2(acac)$ in the α-NPD:$Ir(MDQ)_2(acac)$ layer. Figures 5.1 (b) and (c) in Appendix B show that with a typical experimental uncertainty of about 0.1 eV in the HOMO energies of α-NPD and $Ir(MDQ)_2(acac)$ the calculated current density has an uncertainty of about one order of magnitude. We note that the effects of trapping are strongest at small voltages, when the traps are only partially filled, giving rise to an enhanced steepness of the $J(V)$ curve.

In Figure 5.2 (b) we display the simulated exciton-generation and light-emission profiles. The emission profile is obtained from the exciton-generation profile and the simulation of exciton diffusion. As in the construction of the experimental emission profile, in the blue layer a 1:3 singlet-triplet exciton-generation ratio was assumed, the radiative decay probability in this layer was taken into

account, and no emission from the interlayer was assumed. The resulting emission fractions of the three colours agree well with those of the reconstructed profile in Figure 5.2 (a). The simulated profile is more broadened than the reconstructed profile, but this is probably due to the limited accuracy of the reconstruction procedure, which tends to produce δ-function shaped profiles when the profile width approaches the resolution limit. From the difference between the simulated exciton-generation and light-emission profiles in the green and red layers the crucial role of interlayer exciton transfer becomes clear. Only a small amount of excitons is generated in the red layer, but due to exciton transfer the emission in the red layer is greatly enhanced to a value that is in agreement with experiment.

A sizable amount, 21%, of the excitons in the simulations is generated in the interlayer in between the green phosphorescent and blue fluorescent layer. Accounting for these excitons, which are assumed not to contribute to the luminescence, the calculated EQE drops from the aforementioned 9±1 to 7±1%. When comparing this to the measured EQE of 5±1% we can say that at least a large part of the difference can be explained by excitons generated in the interlayer. Because of the uncertainty in the measured and calculated EQE, it is hard judge about other possible factors causing the difference. However, we expect that the following factors can play an additional role: 1) exciton quenching due to exciton-exciton and exciton-charge interactions, 2) insufficient blocking by the interlayer of transfer of triplet excitons from the green layer to energetically lower-lying triplet-exciton states in the blue fluorescent layer, and 3) a singlet-triplet generation ratio in the blue fluorescent layer that is smaller than the assumed 1:3 ratio. The narrowness of the profiles in Figure 5.2 suggests that exciton quenching could play a role, because of high exciton and charge densities in the exciton-generation and light-emission regions. Simulations in which the dynamics of an exciton is no longer decoupled from that of other excitons and charges should shed light on this.

Inhomogeneities in exciton generation

The simulations provide access to statistical information about electronic processes that cannot be obtained from a continuum treatment. An analysis of the inhomogeneity in the exciton generation can help in assessing the validity of a continuum treatment for describing this process. Also, it can help in assessing material degradation, since a strongly inhomogeneous distribution will likely lead to local material degradation. The inhomogeneity in the exciton generation in the three emission layers and the interlayer is quantified in Figure 5.4, where the fraction of exciton-generation events is plotted as a function of the fraction of sites participating in these events. The strong deviations from a

homogeneous distribution (dashed line) points at an extreme inhomogeneity. Figure 5.4 (a) shows the distribution for the host sites and Figure 5.4 (b) that for the phosphorescent guest sites and the traps in the blue layer. The reason for the occurrence of the inhomogeneity is the fact that exciton generation occurs predominantly at sites that either trap electrons or holes[161]. Because in the green and red layer the triplet emitters act as strong traps for both electrons and holes (see Figure 5.3), most exciton-generation events take place on the emitters, as corroborated by comparing the numbers of these events indicated in Figure 5.4. In these layers, the fraction of host sites on which exciton generation occurs is very low, leading to the observed strong inhomogeneity for these sites.

For the electron traps in the blue layer the inhomogeneity is least pronounced. This is because the fraction of these traps is so low that a sizable fraction of them traps an electron and participates in exciton generation. Most exciton-generation events in the blue layer occur on the host sites, however, and as a result the inhomogeneity in the blue host is not as strong as in the red and green host.

The spatial inhomogeneity in the exciton generation is visualized in Figure 5.5. This figure displays the position-dependent exciton generation in six different slices of sites. In line with Figure 5.4 it is observed that most exciton-generation events occur on a small fraction of the sites. The inhomogeneity is strongest in the green and red layer, because of the guests in these layers. In the blue layer, the trap fraction is so low that it hardly influences the spatial distribution of the exciton generation (one active trap is visible in Figure 5.5 (f)). In addition, strong clustering of exciton generation is observed in all layers, which is due to the correlation in the disorder. This clustering occurs within each slice, but also between adjacent slices in different layers, as becomes clear from comparing Figures 5.5 (a) with (b), (c) with (d), and (e) with (f).

5.5 SUMMARY, CONCLUSIONS, AND OUTLOOK

We have shown in this chapter that it is possible to perform realistic three-dimensional Monte Carlo simulations at the molecular level of electronic processes leading to electroluminescence in multilayer OLED stacks relevant for lighting applications. The focus was on a particular OLED stack, but the developed simulation tools have a broad range of applicability. We stress that the molecular-scale treatment of the electronic processes in this work was essential, for the following reasons: 1) some of the layers in the stack have a thickness of only a few nanometers, i.e., a few molecular diameters, leading to strong

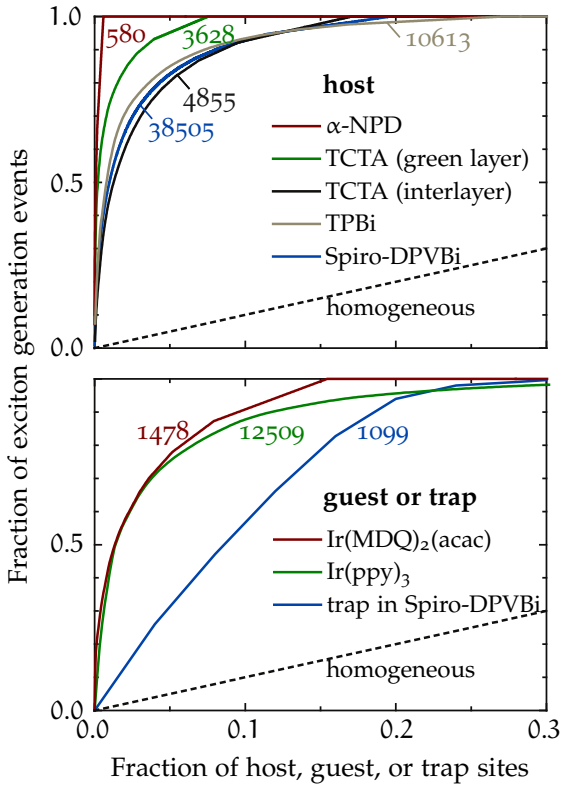

Figure 5.4.: Inhomogeneity in exciton generation. (a),(b), Fraction of exciton generation events in the three emission layers and the interlayer as a function of involved fraction of sites. **a**, For the host sites. **b**, For the phosphorescent guest sites in the red and green layers and the electron traps in the blue layer. The total number of generation events is indicated for each type of site. The straight line segments visible in the final parts of the curves are due to the sites at which only a few generation events occur. A homogeneous distribution of generation events would follow the dashed line.

perpendicular gradients in the electric field and the concentrations of charge-carriers and excitons, 2) the exciton-generation and light-emission profiles have a width of only a few nanometers, even in the layers that are much thicker than a few nanometers, 3) the distribution of exciton-generation events shows large inhomogeneities at the molecular scale, in the perpendicular and lateral directions, and 4) the presence of phosphorescent guests and traps further enhances the effects of these inhomogeneities. Conventional continuum approaches to simulate electronic processes cannot capture these aspects.

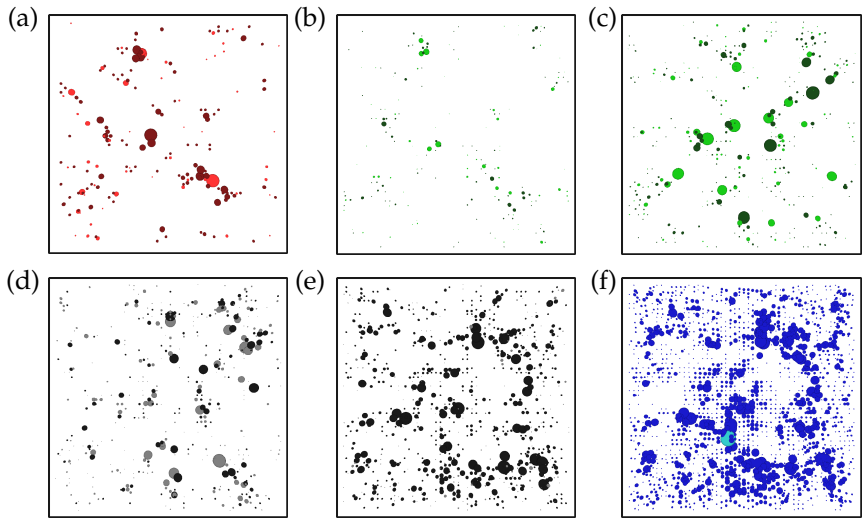

Figure 5.5.: Spatial distribution of exciton generation. (a)-(f), Distribution of exciton generation in six slices of sites, at positions in the stack indicated by the black lines in the bars at the top of each panel. The dark and bright colors indicate host and phosphorescent guest sites (a)-(c) or traps (f), respectively. Black and grey (d), (e) indicate TCTA (hole transporter) and TPBi (electron transporter) sites, respectively.

The work described in this chapter can be considered as the opening of the road towards rational design of multilayer OLED stacks based on molecular-scale modeling of electronic processes. Extensions of the work in various directions are possible. Inclusion of exciton-exciton and exciton-charge quenching processes will be important to assess efficiency loss and material degradation by these processes. Another important extension is the incorporation of information about the microscopic morphology of the stack materials, including the molecular packing and possible dye aggregation, obtained with molecular dynamics or Monte Carlo modeling, and about hopping rates obtained from quantum-chemical calculations [162,163]. This may eventually lead to fully predictive modeling of electroluminescence in OLED stacks. Including these extensions is expected to be feasible without a need for computational resources far exceeding that used in the present work.

A

EXPERIMENTAL AND NUMERICAL METHODS

OLED fabrication and layer-thickness control

The OLED was fabricated by thermal evaporation of the organic materials onto ITO-coated, structured glass substrates in an UHV chamber (Kurt J. Lesker Company) with a base pressure around $10-8$ mbar. The thickness of the organic film is monitored during evaporation by quartz crystal microbalances. This allows for a precise control of the organic layer thickness with nanometre precision, which is in particular important for the deposition of the green emission layer and the interlayer (both 3 nm thick). Furthermore, due to the design of our deposition tool, we observe a very good homogeneity of our films on large areas (less than 5% variation in layer thickness on a $100\times100\,\mathrm{mm}^2$ plate), making us confident that the thickness variation of each layer on the length scale of the OLED is very small. Immediately after preparation the OLED was encapsulated under nitrogen atmosphere using epoxy glue and glass lids.

Reconstruction of the emission profile

The technique to reconstruct the emission profile in the OLED is similar to that introduced in Ref. 150. It is based on the solution of an inverse outcoupling problem and makes use of the calculated angle, polarization, and wavelength dependence of the emission of the radiation of a dipole in the layer stack, averaged over a uniform distribution of orientations. The complex refractive index dispersion curves and photoluminescence spectra (describing the 'source spectra' for the red, green, and blue emission) entering the calculation of the outcoupling were measured or were obtained from the material library of SETFOS (a commercial software program distributed by Fluxim AG, Switzerland). The discretisation step in the reconstruction procedure was 1 nm. It was assumed that the dipoles of each 'colour' are located in the corresponding emission layer and that no emission takes place at organic-organic interfaces and within

the TCTA:TPBi interlayer (the charge-transfer excitons that might be present in these regions are expected to decay non-radiatively or by emitting photons outside the visible spectrum). Since the thickness of the green layer is close to the resolution limit of the reconstruction method, the emission from this layer was assumed to come from its centre. The light emission under an angle θ with the sample normal was measured through a glass hemisphere applied to the glass side of the OLED, with an index-matching fluid in between.

The shape of the emission profile is obtained in the following way using a least-mean-squares fitting method. As a first step, the experimental *s*- and p-polarized emission intensities $I^{expt}_{s(p)}(\lambda,\theta)$, measured at M values of the wavelength λ and N values of the emission angle θ, are normalized using the expression

$$I^{expt}_{norm,s(p)}(\lambda,\theta) = \frac{I^{expt}_{s(p)}(\lambda,\theta)}{S^{expt}_{s(p)}(\lambda)}\ , \tag{A.1}$$

with

$$S^{expt}_{s(p)}(\lambda) \equiv \max(I^{expt}_{s(p)}(\lambda,\theta)). \tag{A.2}$$

The maximum $\max(I^{expt}_{s(p)}(\lambda,\theta))$ is calculated over the entire wavelength and angle range, separately for *s*- and *p*-polarized light.

As a second step, trial intensity functions are calculated. A normalized fixed source spectrum $S^{source}_{k}(\lambda)$, a trial emission profile $P_{k,\delta}$ depending on layer (k) and position (δ, in 1 nm steps), and a trial dipole orientation θ_d are assumed. The emission profile is normalized such that:

$$\sum_{k=1}^{k_{max}} \sum_{\delta} P_{k,\delta} = 1. \tag{A.3}$$

The trial calculated intensity is then:

$$I^{calc,trial}_{s(p)}(\lambda,\theta) = \sum_{k=1}^{k_{max}} \sum_{\delta} P_{k,\delta} S^{source}_{k}(\lambda) I^{calc}_{s(p)}(\lambda,\theta,k,\delta,\theta_d). \tag{A.4}$$

The intensity due to emission from a single dipole at position δ in layer k, $I^{calc}_{s(p)}(\lambda,\theta,k,\delta,\theta_d)$, includes the radiative decay probability in layer k, corrected for microcavity effects. Subsequently, the trial intensity is normalized:

$$I^{calc,trial}_{norm,s(p)}(\lambda,\theta) = \frac{I^{calc,trial}_{s(p)}(\lambda,\theta)}{\max(I^{calc,trial}_{s(p)}(\lambda,\theta))}, \tag{A.5}$$

where the maximum $\max(I^{\text{calc,trial}}_{s(p)}(\lambda,\theta))$ is calculated in the same way as $\max(I^{\text{expt}}_{s(p)}(\lambda,\theta))$. As a final step, the optimal emission profile and dipole orientation are determined by iteratively minimizing the quantity

$$\chi^2 \equiv \sum_{i=1}^{M}\sum_{j=1}^{N}\sum_{s,p}\{I^{\text{calc,trial}}_{\text{norm},s(p)}(\lambda_i,\theta_j) - I^{\text{expt}}_{\text{norm},s(p)}(\lambda_i,\theta_j)\}^2 \,. \tag{A.6}$$

Simulation procedure

The Monte Carlo simulations were performed on a cubic lattice of $50\times50\times56$ sites representing the molecules in the OLED stack, with periodic boundary conditions in the lateral (x- and y-) directions. An energy landscape with correlated disorder was generated by taking a cubic lattice of sites, with a size in the z-direction larger than the thickness of the stack, placing on each site a randomly oriented static dipole, and calculating the resulting electrostatic field at each site (excluding the dipole at that site). Normalization is such that the nearly Gaussian density of states has a standard deviation $\sigma = 0.1\,\text{eV}$*. The red and green emitting guests were introduced in the simulations by offsets, with respect to the surrounding host material, of the HOMO and LUMO energies of sites that were randomly selected according to the concentration of the emitters. Electron traps were introduced by random site selection according to the concentration c_{trap} in the blue fluorescent layer (Spiro-DPVBi) and the electron-transporting layer (NET5). The LUMO energies of the assigned electron traps were drawn from an exponential distribution, $(k_B T_0)^{-1}\exp([E - E_{\text{LUMO,host}}]/k_B T_0)$ if $E < E_{\text{LUMO,host}}$ and otherwise 0, where $E_{\text{LUMO,host}}$ is the centre energy of the Gaussian distribution of the LUMO energies of the surrounding host sites. The HOMO energies of the trap sites were not changed.

Miller-Abrahams rates[65] (Equation 1.10) were taken for the hopping of charges on the lattice. In the case of nearest-neighbour hopping considered by us, the prefactor ν_0 (representing a typical phonon frequency) together with the factor $\exp(-2\alpha a)$ yield a prefactor that was adjusted to reproduce the room-temperature charge-carrier mobility μ_0 at vanishing electric field and charge-carrier concentration of the material under consideration. The energy difference ΔE for a hop of a charge from one site to another contains, apart from the random site energies discussed above, an electrostatic contribution due to the applied bias over the OLED and the Coulomb interaction with all other charges. The latter contribution was calculated as in Ref. 48 by a separation

* The resulting energetic disorder is not perfectly Gaussian, because the precise conditions for the validity of the central-limit theorem are not met. However, this leads to only subtle differences[164]

into a short-range part due to charges within a sphere of radius R_c and a long-range part due to charges outside this sphere, for which a layer-average was taken. A cut-off radius of $R_c = 8$ sufficed in our case. The relative dielectric constants of the layers in the stack are all quite similar and we took them all equal to $\epsilon_r = 3.5$, simplifying the calculation of electrostatic energies. We treated the doped injection layers as metals with a given work function. Injection of holes and electrons from these layers into the adjacent hole and electron transporting layers was treated in the same way as in Ref. 48, with inclusion of an image-charge potential. Exciton generation occurs by hopping of an electron to a site where a hole resides, or vice versa, and is assumed to be always an energetically downward process.

From the room-temperature mobilities μ_0 of holes (h) and electrons (e) of the host materials at low field and low carrier density the hopping frequencies ν_0 were determined using the parameterization in Ref. 83 of the mobility. The precise values of $\nu_{0,h,e}$ for hops in between host sites and guest or trap sites are found not to be important[165] and for simplicity we took them equal to the values in the host. For ν_0 involving hops between sites across an organic-organic interface we took the geometric mean of the bulk values at either side of the interface.

All simulations started with an empty device and an applied bias. A steady-state situation was obtained after typically 2×10^9 Monte Carlo steps, which was judged from the uniformity of the charge current in the z-direction. Subsequently, the current density and the exciton-generation profile were determined from typically another 2×10^9 Monte Carlo steps. For voltages below 2.6 V it was not possible to obtain a statistically significant value for the current density. By repeating the simulations for different disorder configurations we conclude that the error in the reported current density in Figure 5.1 (b) is about 10% and that the error in the reported fractions of exciton generation and light emission in the various layers in Figure 5.2 is about 1% or smaller.

Exciton diffusion was simulated for excitons generated in the green and red layer and started from the calculated exciton generation distribution. An exciton on a triplet emitter was either removed with a probability according to its total (radiative and non-radiative) decay rate or transferred to another emitter. In the latter case an exciton-accepting emitter was selected according to Eq. (5.1). The process continued until each exciton was removed, after which the number of excitons decaying radiatively in each layer was counted. An exciton initially generated on a host site was instantaneously transferred to a guest emitter site selected according to Eq. (5.1).

B

DETERMINATION OF THE MATERIAL PARAMETERS

In this appendix we discuss the determination of the material parameters in the OLED stack, given in Table 5.1. This table is reproduced below as Table 5.1 and includes in addition the main information extracted from a parameter-sensitivity analysis (see next section below). Ultraviolet photoemission spectroscopy (UPS) and optical absorption measurements provided HOMO energies and optical band gaps of most of the materials. The LUMO energies were subsequently obtained by adding the optical gaps. This approach disregards the exciton binding energy, but is nevertheless expected to yield relative LUMO energies with reasonable accuracy because the exciton binding energies are expected to be rather similar for the used materials. Several p-i-p and n-i-n single-carrier devices, with p- and n-doped injection layers and i the intrinsic layer or layer combination to be studied, were prepared. The prepared p-i-p stacks contained parts of the stack structure of Figure 5.1 (a) (excluding the electron-transporter NET5). The analysis of hole transport in these stacks led to the HOMO energies reported in Ref. 146. In n-i-n devices of Spiro-DPVBi and NET5 the electron transport properties were determined from analyses of the current-voltage characteristics, in a similar way as described in Ref. 116 for BAlq. Electron transport in these materials can only be properly described by assuming the presence of electron traps, which appear to have a universal character in organic semiconductors[166]. We model the presence of electron traps using an exponential distribution of trap energies with a concentration c_{trap} and a trap energy $k_B T_0$. We discuss the layers in the stack structure of Figure 5.1 (a) of the main chapter from bottom to top:

NHT5:NDP2 – hole-injecting layer: The HOMO energy of NHT5 was measured by UPS to be located at −5.1 eV with respect to the vacuum level. The p-doped NHT5:NDP2 layer is treated in the simulations as a metal with a work function for hole injection equal to this energy.

α-NPD – hole-transporting layer: Hole transport in p-i-p stacks[146] could be properly modelled with an α-NPD HOMO energy of −5.33 eV. By adding the mea-

sured optical gap of 3.1 eV we put the LUMO energy at −2.23 eV. Modelling of charge transport at various temperatures in 100 and 200 nm thick hole-only devices of α-NPD within an extended version of the correlated disorder model (ECDM)[83] led to $\mu_{0,h} = 9 \times 10^{-9}\,m^2/Vs$. Analysis of hole transport in a p-i-p device with α-NPD as the intrinsic layer led to $\mu_{0,h} = 3 \times 10^{-9}\,m^2/Vs$[167]. We decided to use the average of these two values for the hole mobility of α-NPD: $\mu_{0,h} = 6 \times 10^{-9}\,m^2/Vs$. The value taken for the electron mobility in α-NPD is not critical. We take it 10 times smaller than the hole mobility: $\mu_{0,e} = 6 \times 10^{-10}\,m^2/Vs$.

α-NPD:Ir(MDQ)$_2$(acac) – phosphorescent red layer: Hole transport in p-i-p stacks[146] could only be properly modelled by assuming a dipole layer at the α-NPD/α-NPD:Ir(MDQ)$_2$(acac) interface, leading to an offset of 0.1 eV and a HOMO energy of α-NPD in this layer of −5.43 eV. Adding the measured optical gap of 3.1 eV we put the LUMO energy at −2.33 eV. For $\mu_{0,h}$ and $\mu_{0,e}$ we take the same values as in the pure α-NPD layer. UPS measurements put the HOMO energy of Ir(MDQ)$_2$(acac) 0.3 eV higher than that of α-NPD, so we put this energy at −5.13 eV. The LUMO energy of Ir(MDQ)$_2$(acac) is obtained by adding the measured optical gap of 2.2 eV, so we put this energy at −2.93 eV.

TCTA:Ir(ppy)$_3$ – phosphorescent green layer: Hole transport in p-i-p stacks[146] could be properly modelled by taking the HOMO energy of TCTA at −5.6 eV. Adding the optical gap of 3.4 eV we put the LUMO energy of TCTA at −2.2 eV. For the hole mobility of TCTA we take the literature value $\mu_{0,h} = 2 \times 10^{-8}\,m^2/Vs$[168]. No literature value of the electron mobility is known to us. The presence of electron traps (which we do not explicitly consider in this layer) will reduce the electron mobility as compared to the hole mobility. We take the electron mobility 10 times lower: $\mu_{0,e} = 2 \times 10^{-9}\,m^2/Vs$. UPS measurements put the HOMO energy of Ir(ppy)$_3$ 0.4 eV higher than that of TCTA, so we take −5.2 eV for this energy. The LUMO energy of Ir(ppy)$_3$ is obtained by adding the measured optical gap of 2.5 eV, leading to −2.7 eV.

TCTA:TPBi – interlayer: We take the parameters of TCTA in this layer equal to those in the phosphorescent green layer. UPS measurements put the HOMO energy of TPBi 0.6 eV lower than the HOMO energy of TCTA, so we take −6.2 eV for this energy. The LUMO energy of TPBi is obtained by adding the measured optical gap of 3.6 eV, leading to −2.6 eV. We take the electron and hole mobilities of TPBi equal to those of TCTA.

Spiro-DPVBi – fluorescent blue layer: Hole transport in p-i-p stacks[146] could be properly modelled by taking the HOMO energy of Spiro-DPVBi at −5.7 eV. Adding the measured optical gap of 2.9 eV leads to a LUMO energy of −2.8 eV. Modelling studies within the ECDM in n-i-n electron-only devices with Spiro-DPVBi as intrinsic layer led to a description of electron transport with an electron mobility $\mu_{0,e} = 8 \times 10^{-9}\,m^2/Vs$, an electron-trap concentration $c_{trap} =$

10^{-3}, and a trap temperature $T_0 = 2350$ K of the trap distribution. We take the hole mobility in Spiro-DPVBi equal to the hole mobility in α-NPD, so $\mu_{0,h} = 6 \times 10^{-9}\,m^2/Vs$.

NET5 – electron-transporting layer: In modelling studies of electron transport within the ECDM in n-i-n electron-only devices with NET5 as intrinsic layer a description could be obtained with a LUMO energy of NET5 at -2.5 eV. Subtracting the measured optical gap of 3.5 eV leads to a HOMO energy of -6.0 eV. This modelling led to an electron mobility of $\mu_{0,e} = 1.5 \times 10^{-10}\,m^2/Vs$, an electron trap concentration $c_{trap} = 5 \times 10^{-3}$, and a trap temperature $T_0 = 1400$ K of the electron trap distribution. We take the non-critical hole mobility a factor of 10 smaller than the electron mobility, so $\mu_{0,h} = 1.5 \times 10^{-11}\,m^2/Vs$.

NET5:NDN1 – electron-injecting layer: We model this layer as a metal with a work function equal to the LUMO energy of NET5: -2.5 eV.

C

PARAMETER-SENSITIVITY ANALYSIS

The material parameters in Table C.1 were varied in order to determine the sensitivity of the current density J and the fractions of excitons generated in the various layers to these parameters. This sensitivity is indicated by a coding in Table C.1. Several parameters have no or only a small influence on J and/or on the exciton-generation fractions. We show here the most interesting dependences. The bias applied over the OLED stack was 3.6 V in the investigation of most of the parameter dependences. In a few cases the current became too small to systematically investigate the dependence on a particular parameter and in those cases we applied a bias of 7.6 V in the simulations.

Figure C.1 shows the dependence of J on various parameters. It was found that the largest voltage drop in the simulations occurs over the red phosphorescent layer (α-NPD:Ir(MDQ)$_2$(acac)). Therefore, J depends mostly on the material parameters of this layer. Since the hole-transporting layer also consists of α-NPD, we decided to change the HOMO energy of the α-NPD in the hole-transporting layer and in the red phosphorescent layer independently in the simulations. Figure C.1 (a) shows the dependence of J on the HOMO energy of the α-NPD in the hole-transporting layer and Figure C.1 (b) the dependence on the HOMO energy in the hole-transporting layer. The dependence in the former case is clearly weaker than in the latter case. A maximum in J is found in Figure C.1 (a) for the nominal value of the HOMO energy, indicated by the dashed line. The reason for the occurrence of this maximum is that for this value a compromise is established between the barrier for hole transport across the energy barrier for holes at the NHT5:NDP2/α-NPD interface and the α-NPD/α-NPD:Ir(MDQ)$_2$(acac) interface; see Figure 5.3 in main chapter. In the α-NPD:Ir(MDQ)$_2$(acac) layer the hole transport is strongly influenced by trapping at the Ir(MDQ)$_2$(acac) sites. This is clear from Figures C.1 (b) and c, the latter showing the dependence of J on the HOMO energy of Ir(MDQ)$_2$(acac). The highest current is obtained if the HOMO energies of α-NPD and Ir(MDQ)$_2$(acac) are the same, for which case no trapping occurs. Finally, Figure C.1 (d) shows the dependence of J on

Material	E_{HOMO} (eV)	E_{LUMO} (eV)	$\mu_{0,h}$ (m^2/Vs)	$\mu_{0,e}$ (m^2/Vs)	c_{trap}	T_0 (K)
NHT5:NDP2	−5.10					
α-NPD	−5.33	−2.23	6.0×10^{-9} cri	6.0×10^{-10}		
α-NPD	−5.43 CR	−2.33	6.0×10^{-9} cri	6.0×10^{-10}		
$Ir(MDQ)_2(acac)$	−5.13 CRib	−2.93 r	6.0×10^{-9} cri	6.0×10^{-10}		
TCTA	−5.60 RGiB	−2.20 Rgib	2.0×10^{-8} Rgib	2.0×10^{-9} Rgib		
$Ir(ppy)_3$	−5.20 RGib	−2.70 Rg	2.0×10^{-8} Rgib	2.0×10^{-9} Rgib		
TCTA	−5.60 RGiB	−2.20 Rgib	2.0×10^{-8} Rgib	2.0×10^{-9} Rgib		
TPBi	−6.20	−2.60 RGIb	2.0×10^{-8} Rgib	2.0×10^{-9} Rgib		
Spiro-DPVBi	−5.70	−2.80 rGib	6.0×10^{-9} rib	8.0×10^{-9} ri	0.001	2350
NET5	−6.00	−2.50	1.5×10^{-11}	1.5×10^{-10} r	0.005	1400
NET5:NDN1		−2.50				

Table C.1.: HOMO and LUMO energies, room-temperature hole and electron mobilities $\mu_{0,h}$ and $\mu_{0,e}$ at low field and low carrier density, electron-trap concentration c_{trap}, and trap temperature T_0 of the trap distribution in the different layers of the stack, as used in the Monte Carlo simulations. The sensitivity of the current density and the exciton recombination fraction in the emission layers and the interlayer to a change in HOMO or LUMO energy by ±0.1 eV or in the mobility by a factor 10 or 0.1 is indicated by a code. C (c): change in current density by more than a factor ten (by a factor between two and ten). R, G, I, and B (r, g, i, and b): change by more than 50% (change between 20 and 50%) in the fraction of excitons generated in the red layer, green layer, interlayer, and blue layer. No indication in case of a smaller change.

the hole mobility of α-NPD. This dependence is close to linear, which is consistent with the picture that the current is determined by hole transport in the α-NPD:$Ir(MDQ)_2(acac)$ layer.

Figure C.2 shows the dependence of the fractions of the number of excitons generated in the red phosphorescent layer, the green phosphorescent layer, the interlayer, and the blue fluorescent layer on several HOMO energies. Figure C.2 (a) shows that the dependence of the exciton fractions on the HOMO energy of α-NPD is rather weak. However, if the HOMO energy gets close the HOMO energy of TCTA (−5.6 eV) the barrier for hole injection from the red into the green layer disappears and so does the fraction of excitons generated in the red layer. The dependences of the exciton fractions on the HOMO energy of the red emitter ($Ir(MDQ)_2(acac)$, Figure C.2 (b)), the HOMO energy of the hole transporter in the interlayer (TCTA, Figure C.2 (c)), and the HOMO energy of the green emitter ($Ir(ppy)_3$, Figure C.2 (d)) are very strong. The dependence of the exciton fractions on the HOMO energy of $Ir(MDQ)_2(acac)$ in Figure C.2 (b) could only be systematically investigated at a bias of 7.6 V. Figure C.2 (d) shows that the fraction of excitons generated in the interlayer (TCTA:TPBi) has a peak at the nominal value of the HOMO energy of $Ir(ppy)_3$. Precisely at this value, the balance between excitons generated in the green and the blue layer changes and the fraction of excitons generated in the red layer takes off. The reason

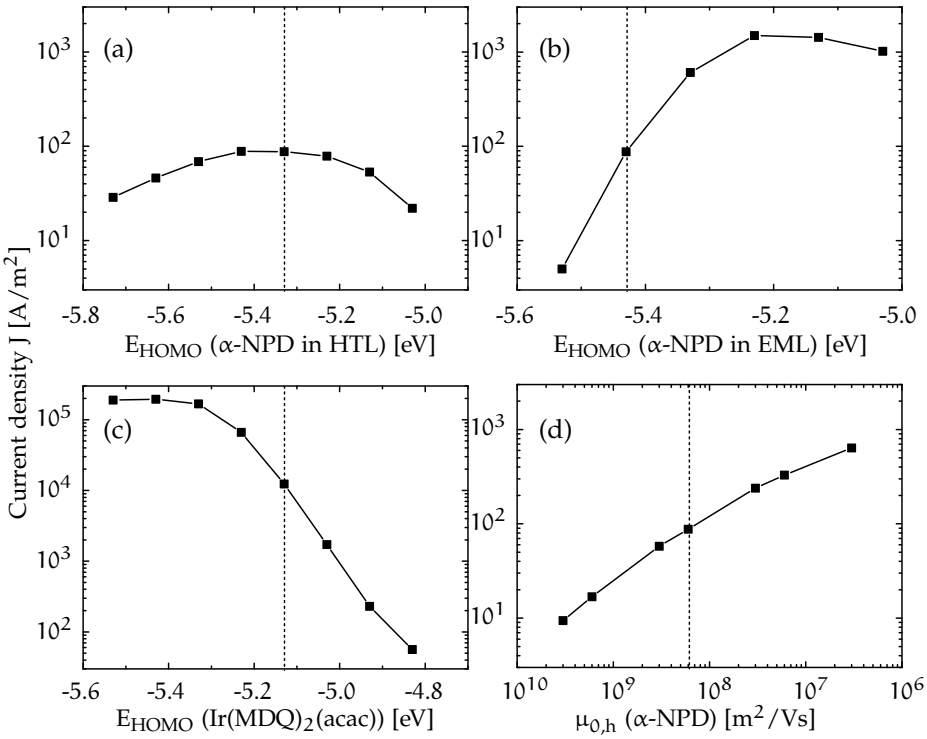

Figure C.1.: Dependence of the current density J on **a**, the HOMO energy of the α-NPD in the hole-transporting layer (HTL), **b**, the HOMO energy of the α-NPD in the red phosphorescent emission layer (EML), **c**, the HOMO energy of the red phosphorescent guest $Ir(MDQ)_2(acac)$, and **d**, the hole mobility of α-NPD (the same in the HTL and EML). The dependence on the HOMO energy of $Ir(MDQ)_2(acac)$ in **c** was investigated at a bias of 7.6 V. In the other cases the bias was 3.6 V. The error in J is of the order of 10% or less. The dashed lines indicate the nominal values in Table C.1.

is that at this value there is substantial transport of both holes and electrons through the interlayer. This is as required for a proper colour balance of this OLED, but at the same it leads to substantial exciton generation in the interlayer, causing a loss of efficiency.

Figure C.3 shows the dependence of the exciton generation fractions on several LUMO energies. The dependence on the LUMO energy of the green emitter ($Ir(ppy)_3$, Figure C.3 (b)) around its nominal value is moderate, but the dependences on the LUMO energies of the hole transporter in the interlayer (TCTA, Figure C.3 (a)), of the electron transporter in the interlayer (TPBi, Figure C.3 (c)), and of the blue fluorescent electron transporter (Spiro-DPVBi, Figure C.3 (d)) are very strong. In particular, it is observed from Figure C.3 (c) that the value

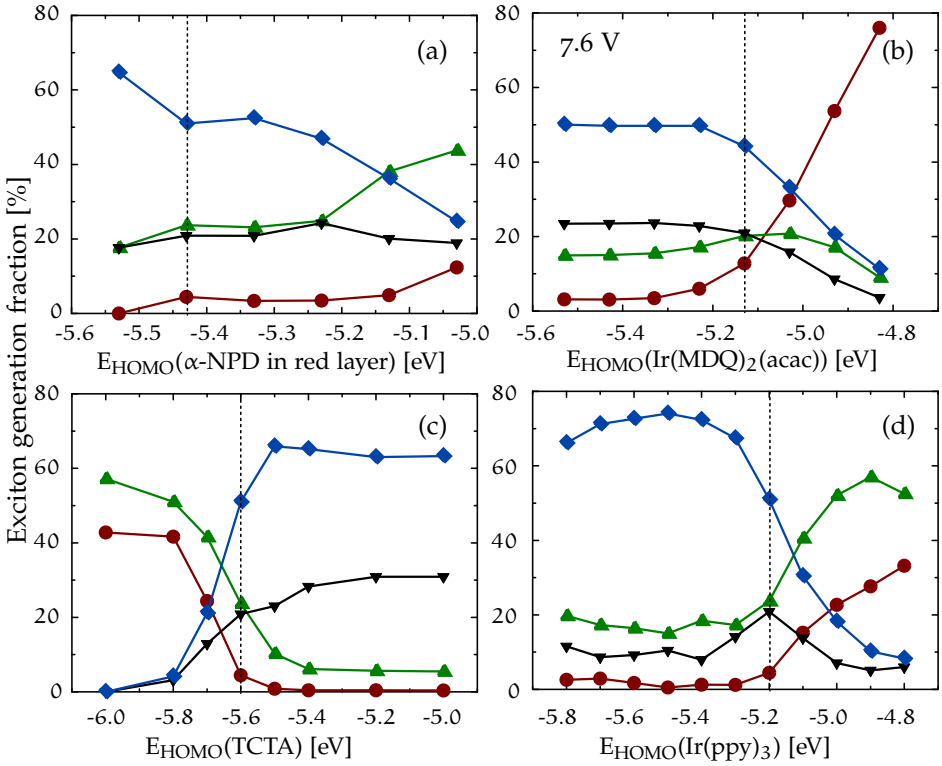

Figure C.2.: Dependence of the fractions of excitons generated in the red layer (discs), green layer (up triangles), interlayer (down triangles), and blue layer (diamonds) on the HOMO energy of **a**, α-NPD in the red emission layer, **b**, the red phosphorescent guest $Ir(MDQ)_2(acac)$, **c**, the hole transporter in the interlayer TCTA, and **d**, the green phosphorescent guest $Ir(ppy)_3$. In **b** the applied bias was 7.6 V, while for the other cases it was 3.6 V. The error in the fractions is of the order of 1%. The dashed lines indicate the nominal values.

of the LUMO energy of TPBi is extremely critical: a deviation of only 0.2 eV from its nominal value leads to a dramatic suppression of excitons generated in the red and green layer. From Figure 5.3 in the main chapter it follows that if the LUMO energy is too low, the energy barrier for transport of electrons from the interlayer to the green layer becomes too high, whereas if this energy is too high, the energy barrier for transport of electrons from the blue layer to the interlayer becomes too high. In both cases, the result is that electrons cannot reach the green and red layers to form excitons with the holes present in these layers. These findings makes clear that small changes in energy levels of the

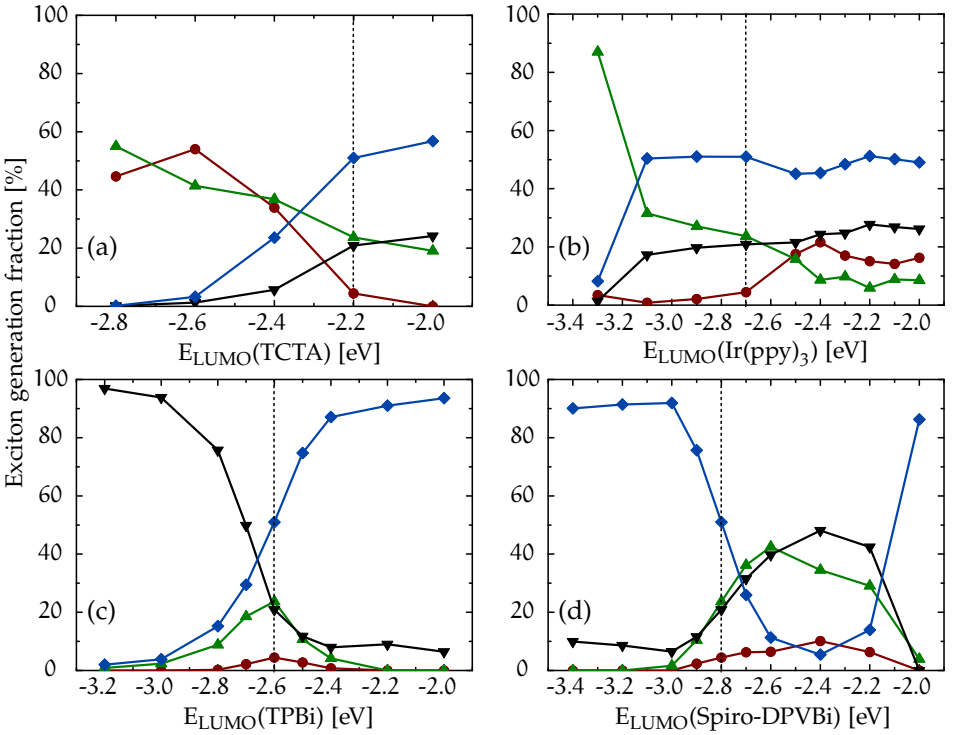

Figure C.3.: Dependence of the fractions of excitons generated in the various layers on the LUMO energy of **a**, the hole transporter in the interlayer TCTA, **b**, the green phosphorescent guest $Ir(ppy)_3$, **c**, the electron transporter in the interlayer TPBi, and **d**, the blue fluorescent electron transporter Spiro-DPVBi.

materials in the stack can have a dramatic influence on the performance of the OLED.

Finally, Figure C.4 shows the dependences of the exciton generation fractions on the hole (Figure C.4 (a)) and electron (Figure C.4 (b)) mobilities of the hole (TCTA) and electron (TPBi) transporter in the interlayer, and on the hole (Figure C.4 (c)) and electron (Figure C.4 (d)) mobilities of the blue fluorescent electron transporter (Spiro-DPVBi). It is seen that these dependences are rather gradual and far less dramatic than the dependences on HOMO and LUMO energies in Figures C.2 and C.3. The trends in Figures C.4 (a) and (b) are readily understood from an increase of the number of holes that can reach the electrons in the blue layer if the hole mobility in the interlayer increases, and from an increase of the number of electrons that can reach the holes in the red and green layer if the electron mobility in the interlayer increases. From Figures C.4 (c) and (d) it can be seen that changes in the mobilities in the blue layer have only

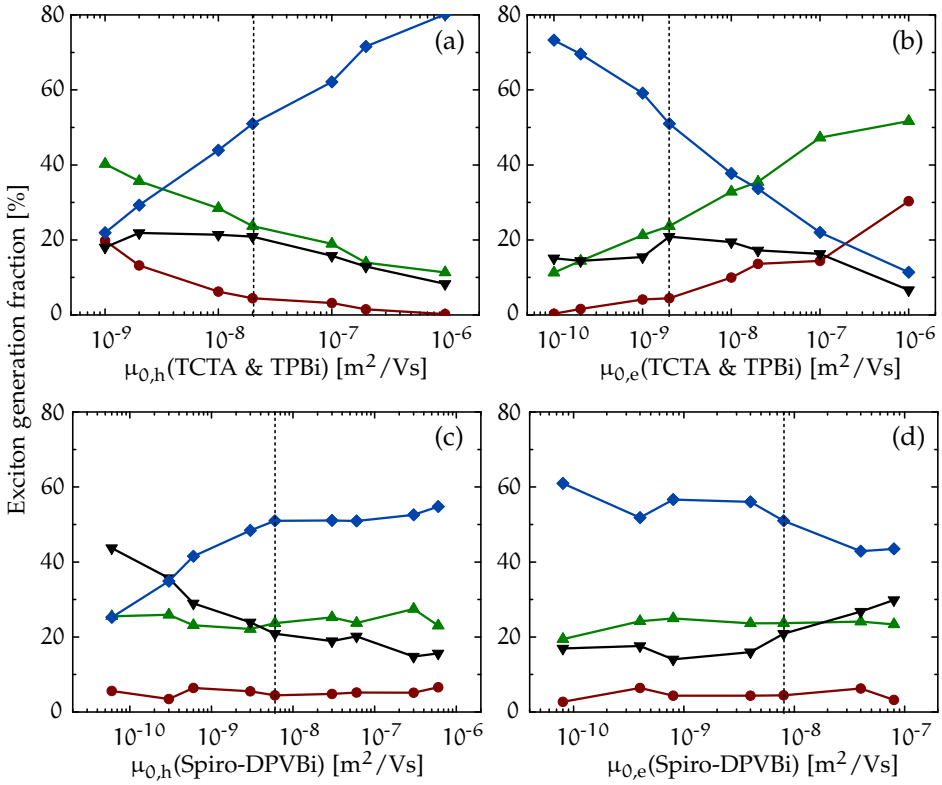

Figure C.4.: Dependence of the fractions of excitons generated in the various layers on **a**, the hole mobilities of the TCTA and TPBI in the interlayer, **b**, their electron mobilities, **c**, the hole mobility of the blue fluorescent electron transporter DPVBi, and **d**, its electron mobility.

a small influence on the exciton generation fractions. The influence of changes in the mobilities in other layers were found to be even less important.

The general conclusion that can be drawn is that energy-level differences in OLED stacks appear to be very critical and mobilities moderately critical for the OLED performance. Changes in some energy levels in the stack materials of only 0.1 eV can lead to changes in exciton generation fractions of over 50%. On the other hand, changes in the mobilities of the stack materials of more than an order of magnitude have a modest (between 20 and 50%) or small (less than 20%) influence on the fractions of generated green and blue excitons (disregarding red excitons for reasons mentioned earlier). Changes in energy levels of 0.1 eV in the red emitting layer can also considerably change the current density (by more than an order of magnitude), while changes in the mobilities of more than an order of magnitude have a moderate influence on the current

density (changes by less than an order of magnitude and for several mobilities by less than a factor of two). An important conclusion is that the results presented in the main chapter are relatively insensitive to changes in the mobilities that could not be experimentally determined and for which we had to make assumptions.

6

MODELING OF EXCITON PROCESSES IN A MULTILAYER WHITE OLED

ABSTRACT In the present chapter we further investigate exciton processes in the multilayer white OLED stack of Chapter 5 by kinetic Monte Carlo simulations. In particular, we study the dependence of the internal quantum efficiency (IQE) on the current density. The measured increase of the IQE at low current density, the roll-on, can be qualitatively modeled without including exciton quenching processes. We explain the roll-on by a decrease in the fraction of non-radiative excitons generated in the interlayer between the blue fluorescent and green phosphorescent layer with increasing current density. We model the triplet-polaron quenching (TPQ) and triplet-triplet annihilation (TTA) that occur at high current density by assuming that such quenching occurs instantaneously when the triplet exciton and the polaron (for TPQ), or the two triplet excitons (for TTA), are on nearest-neighbor sites. With this assumption we find that in the modeling TPQ is the dominant quenching process up to very high current densities. The decrease of the IQE at high current density, the roll-off, is found to be weaker than in experiment. This indicates that our simple nearest-neighbor modeling for exciton quenching is insufficient and suggests that taking into account long-range exciton quenching processes might be necessary.

6.1 INTRODUCTION

The introduction of phosphorescent emitters in white OLED designs has gained much interest due to the possibility of obtaining a very high internal quantum efficiency (IQE)[14,26,30]. A purely fluorescent OLED is expected to reach a maximum IQE of 25% due to the restrictions imposed by quantum-mechanical selection rules on spin states, which only allow singlet excitons to decay radiatively. The presence of spin-orbit coupling in phosphorescent emitters also allows triplet excitons to decay radiatively, providing the possibility of reaching an IQE of close to 100%. However, triplet excitons have a lifetime that is at least two orders of magnitude longer than that of singlet excitons[13]. As a consequence, they are more vulnerable to exciton quenching. Exciton quenching will increase in importance when the current density and the brightness level of the OLED increases, since the densities of charge carriers and excitons are then higher. The drop in the efficiency with increasing current density as a result of exciton quenching is known as the efficiency roll-off. A better understanding of the factors that determine this roll-off is crucial, because in practice one would like to use white OLEDs for lighting at the highest possible brightness levels. Moreover, exciton-quenching processes may also be a source for material degradation, because the involved high excitation energies may lead to breaking of chemical bonds and therefore to loss of functionality of the semiconducting molecules.

In the previous chapter we showed that it is possible to study the processes that lead to electroluminescence in a hybrid multilayer white OLED by kinetic Monte Carlo simulations. We followed a two-step approach in these simulations. First, the dynamics of electrons and holes and the generation of excitons was simulated. The sites at which excitons were generated were recorded. Next, in the green and red phosphorescent layer, excitons were released at those sites and their dynamics was simulated. The interaction of these excitons among each other and with charges was neglected. We considered Förster-type resonance energy transfer between phosphorescent guests in the green and red layer and from the green to the red layer. This resonance energy transfer was found to be crucial for obtaining the right color of this OLED. In the present chapter we continue our analysis of electronic processes leading to electroluminescence by investigating the effects of exciton quenching processes.

One of the challenges in OLED technology is to prevent efficiency roll-off at the operating current density and brightness values. Three exciton-quenching mechanisms[31,169,170] accounting for efficiency roll-off have been identified: triplet-triplet annihilation (TTA), triplet-polaron quenching (TPQ), and field-induced exciton dissociation. Complicating aspects in the analysis of exciton quenching are that the dominant quenching process may depend on the particu-

lar system and that a predictive description of quenching processes is presently lacking. Reineke et al.[170] argue that field-induced dissociation does not play an important role in state-of-the-art OLEDs. Baldo et al.[31] claim that TTA is the only process responsible for efficiency roll-off in the case of $Ir(ppy)_3$ and octaethylporphine platinum (PtOEP) dyes. On the other hand, Kalinowski et al.[32] claim that field-induced dissociation and TPQ are the main mechanisms behind the efficiency roll-off. In the present chapter we will make a first attempt to analyse exciton quenching for the case of the multilayer white OLED stack investigated in Chapter 5.

6.2 METHODS

The kinetic Monte Carlo code that was used in Chapter 5 had to be modified in order to treat charge-carrier and exciton dynamics in an integrated way. We want to focus on the excitonic processes taking place in and in between the green and red phosphorescent layers. In the blue fluorescent layer, light emission occurs by radiative decay of short-lived ($\sim$ ns) singlet excitons, which are not expected to suffer from quenching processes. The triplet excitons formed in this layer might be involved in quenching processes. However, these excitons are assumed not to contribute to the luminescence and are hence disregarded. Therefore, singlet and triplet excitons formed in the blue fluorescent layer are immediately removed in the simulations. We assume that all excitons formed in the interlayer between the blue fluorescent and green phosphorescent layer are lost and therefore we also immediately remove these excitons after formation. We have to keep in mind the possible errors introduced by this drastically simplified treatment of excitons in these layers. For example, TTA in the blue layer may result in the production of singlet excitons and could therefore increase the blue component of the light. However, lack of information about the lifetime of triplet excitons in the blue layer presently prevents a useful modeling of this process.

In Chapter 5 exciton formation was assumed to be always an energetically downward process. Here, we refine this approach by taking into account the binding energy of an exciton. An exciton is then modeled as an electron-hole pair at a site with an energy equal to its HOMO-LUMO energy difference minus the binding energy. In contrast to Chapter 5, exciton dissociation is thus possible. However, charge carriers generated from dissociated excitons can again participate in exciton formation, so that exciton dissociation is in our case no loss channel. In the blue fluorescent layer we take an exciton binding energy of 0.5 eV, corresponding to a typical singlet exciton binding energy. We assume, like in Chapter 5, that 25% of the excitons formed in this layer are singlets. In the interlayer and in the green and red phosphorescent layers we take

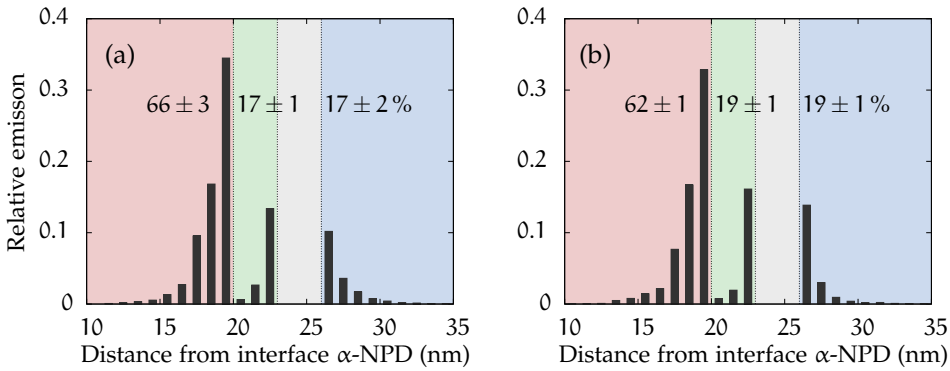

Figure 6.1.: (a) Simulated light-emission profile of the OLED of Chapter 5 at a bias of 3.6 V using the integrated approach of treating charge-carrier and exciton dynamics. Exciton quenching is disregarded. (b) Profile using the non-integrated approach, reproduced from Figure 5.2 b.

an exciton binding energy of 1.0 eV, corresponding to a typical triplet exciton binding energy. Like in Chapter 5, an exciton initially generated on a host site in the green or red layer is instantaneously transferred as a triplet exciton to a guest emitter according to Equation (5.1). After that, radiative or non-radiative decay, dye-to-dye transfer, dissociation, or quenching may occur. Radiative and non-radiative decay and dye-to-dye transfer is modeled in the same way as in Chapter 5, disregarding disorder in the exciton energies. Exciton dissociation is modeled as a hop of either the electron or hole of the exciton to a neighboring site. The quenching processes leading to TPQ and TTA have been discussed in Section 2.1. We have, however, no information about the rates of these processes and we therefore choose a drastically simplified approach: a quenching process is assumed to take place instantaneously when a charge and a triplet exciton (TPQ) or two triplet excitons (TTA) are on nearest-neighbor sites. In the case of TPQ, the triplet exciton is removed and the charge remains. In the case of TTA, one of the two, arbitrarily chosen, triplet excitons is removed, and the other one remains. This simplified approach was recently presented by van Eersel et al.[113] in their study of the efficiency roll-off in PtOEP and $Ir(ppy)_3$ based prototypical OLEDs.

6.3 RESULTS AND DISCUSSION

In order to cross-check the results of the integrated approach of treating charge-carrier and exciton dynamics with the results of the non-integrated approach used in Chapter 5, we show in Figure 6.1 a the simulated emission profile of the OLED of Chapter 5 at a bias of 3.6 V obtained with the integrated approach

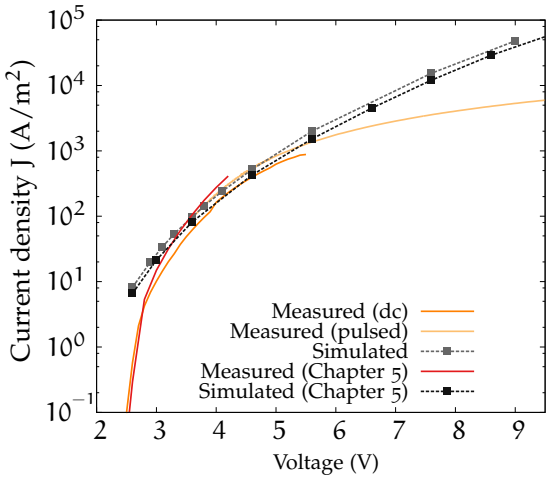

Figure 6.2.: Measured and simulated current density–voltage (J–V) curves. The red line is the original J–V curve from Figure 5.1 b. The dark orange line is the remeasured J–V curve. The light orange line is the J–V curve obtained with pulsed measurements. The black squares are the simulation results of the non-integrated approach for describing charge-carrier and exciton dynamics, copied from Figure 5.1 b. The grey squares are the simulation results of the integrated approach. Inclusion of exciton-quenching effects has no discernible influence on the simulated J–V curve.

when TPQ and TTA are disregarded. Comparing this figure with Figure 5.2 b (lower panel), which is reproduced as Figure 6.1 b, we conclude that, within the error bars, the results are the same. The corresponding current density–voltage curve is plotted in Figure 6.2, together with the curve of the non-integrated approach from Figure 5.1 b. Again, we observe that the results are essentially the same. We note that, apart from the neglect of exciton dissociation, the non-integrated approach also neglects the fact that a charge and an exciton, or two excitons, cannot occupy the same site. Apparently, neither has a significant influence on the simulation results. Figure 6.2 also shows a remeasured current–voltage curve, together with the original measurement from Figure 5.1 b. We notice that at high voltage the current density has decreased somewhat, pointing at a possible slight degradation during the approximately three-and-a-half years in between the measurement in Figure 5.1 b and the repeated measurement.

In addition, current density-voltage data obtained with a pulsed approach are given in Figure 6.2. Using such an approach, it is possible to reach higher voltages and currents than with a dc approach, because the effects of heating are suppressed. The pulsed measurements were performed in three voltage regions with different pulse duration: 1) For $V < 4\,\mathrm{V}$ pulses of 1 s were used.

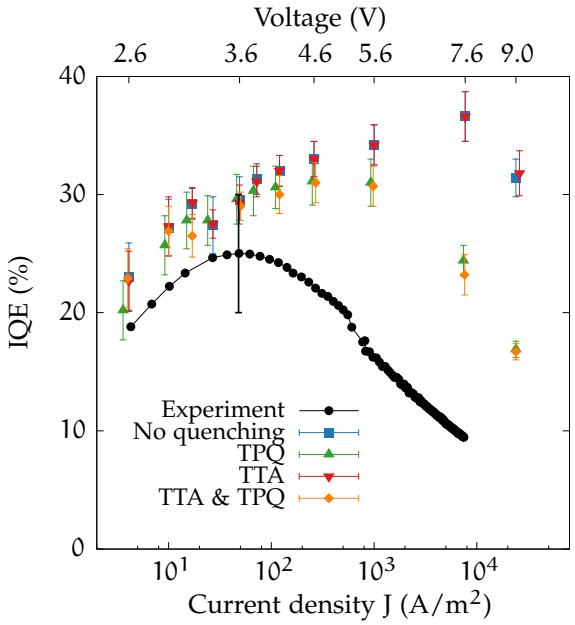

Figure 6.3.: Experimental and simulated internal quantum efficiency (IQE) as a function of current density. The corresponding voltages of the simulated J–V curve of Figure 6.2 (grey squares) are given at the top axis. The experimental IQE was obtained by dividing the measured luminescence perpendicular to the OLED pixel by the current density and normalizing such that the IQE of 25±5% at 3.6 V agrees with the measured external quantum efficiency (EQE) and the outcoupling efficiency reported in Chapter 5. The simulated results are for the cases of no quenching, triplet-polaron quenching (TPQ), triplet-triplet annihilation (TTA), and combined TPQ and TTA.

2) For $4 < V < 6\,\mathrm{V}$ pulses of 0.1 s were used. 3) For $V > 6\,\mathrm{V}$ pulses of $50\,\mu\mathrm{s}$ were used with a duty cycle of 1%. Since all data connect smoothly, we can conclude that relaxation effects due to the use of pulses are small. We observe that at high voltage the experimental current densities are significantly lower than the simulated ones. The deviations at low voltage were already discussed in Chapter 5.

The simulated results for the IQE (the fraction of generated excitons decaying radiatively) is plotted as a function of the current density in Figure 6.3, together with the experimental IQE. The experimental IQE was obtained by dividing the luminescence as measured by a photodiode perpendicular to the OLED pixel by the current density and scaling the result such that at 3.6 V the IQE is 25±5%, corresponding to the measured external quantum efficiency (EQE) of 5±1% and the light-outcoupling efficiency of 20±1%, as reported in Chapter 5. In the

region of $4-6\,\mathrm{V}$, hysteresis effects are found to be present in the luminescence: forward and backward voltage sweep produce scattered efficiency values. The plotted results are an average of several measurements of forward an backward sweeps, connecting smoothly to the results in the voltage regions where such hysteresis is absent. The efficiency is obtained by pulsed measurements in the high current density region $J > 500\,\mathrm{A/m^2}$, where the transition between dc and pulsed measurements can be seen in Figure 6.3. We observe that at low current density the experimental IQE is somewhat lower than the simulated IQE, while at high current density the experimental IQE is considerably smaller.

The increase of the IQE at low current density, the roll-on, is qualitatively reproduced by the simulations. An analysis of the color balance shows that at low current density the fraction of blue light slightly increases with voltage in the experiment, while it slightly decreases in the simulations. The slight decrease of the fraction of blue light in the simulations leads to a slight increase of the IQE due to the fact that the efficiency of the blue emission is smaller than that of the green and red emission. This increase is, however, not sufficient to explain the observed increase in the IQE. It turns out that a larger part of the observed increase in the IQE can be explained by the fact that with increasing current density significantly less non-emissive excitons are produced in the interlayer. The slight shift to the blue in the experiment can possibly be attributed to the formation of singlets due to the TTA processes in the blue fluorescent layer, which is not included in the simulations.

We now investigate the effects of exciton quenching by considering three quenching scenarios: 1) only TPQ, 2) only TTA, 3) combined TPQ and TTA. The resulting current density–voltage curves fall on top of the curve without quenching in Figure 6.2. We can conclude from this that quenching effects have no influence on the current density for this OLED. The results for the IQE are shown in Figure 6.3. We observe that in the whole voltage range considered the influence of TTA is negligible as compared to TPQ. However, the role-off in the simulations sets in at a too high current density. We attribute this to the too simple model for exciton quenching used by us. In particular, we suggest that the nearest-neighbor quenching approximation is too simple and that long-range quenching effects by a Förster-type transfer should be considered.

CONCLUSIONS AND OUTLOOK

CONCLUSIONS

The work described in this thesis had two goals: (1) To come to a description and understanding of non-stationary charge dynamics in disordered organic semiconductors (Chapters 3 and 4). (2) To come to a characterization of the factors controlling the electroluminescence in a multilayer white OLED (Chapter 5). We tried to reach these goals by making use of two advanced simulation methods, described in Chapter 2: (i) Solving a three-dimensional time-dependent master equation for the occupational probabilities of sites in the organic semiconductor by charges. (ii) Explicitly simulating the charge and exciton dynamics by kinetic Monte Carlo. The disorder was modeled by a spatially uncorrelated or correlated (nearly) Gaussian density of states (DOS) of the on-site energies. Our general strategy has been, first, to obtain agreement with measured (opto)electronic properties of actual organic devices and, second, to understand from the comparison of simulations and experiment the role of the involved electronic processes at the molecular scale on the establishment of these properties. With our molecular-scale simulations we went beyond the present state-of-the-art in the following ways. Our work extended previous molecular-scale simulations of charge transport in unipolar devices by including the time dependence, thereby obtaining for the first time a complete description of charge-carrier relaxation in these devices. By combining charge dynamics with exciton dynamics, our work also provided for the first time a complete molecular-scale description of all electronic processes leading to electroluminescence and exciton quenching in a realistic white OLED. The main conclusions of the work are the following.

In *Chapter 3* we studied charge-carrier relaxation effects in hole-only devices of a polyfluorene-based light-emitting polymer by simulating dark-injection experiments. In these experiments, a peak in the current transient that signals the arrival of injected charge carriers at the collecting electrode appears earlier than predicted by simplified device simulations using the equilibrium charge-carrier mobility. We attributed this disagreement to charge-carrier relaxation effects, which lead to a mobility directly after injection that is higher than the equilibrium mobility. Simulating the current transients by solving the three-dimensional time-dependent master equation with the same width of the

(uncorrelated) Gaussian DOS as obtained from modeling of the steady-state current density–voltage characteristics significantly improves the agreement with the measured current transient. However, the peak in these simulations has been washed out. Taking a somewhat smaller Gaussian width leads to a very good agreement. We concluded from this that the modeling of the DOS by a single Gaussian may be too simple and that the discussion about the appropriate model for charge transport in disordered organic semiconductors should be reopened.

In *Chapter 4* we continued our analysis of charge-carrier relaxation effects by simulating impedance-spectroscopy measurements performed on the same hole-only devices as in Chapter 3. The capacitance–voltage characteristics obtained from these measurements does not agree with simplified device simulations that use the equilibrium charge-carrier mobility. We again concluded that this is due to the neglect of charge-carrier relaxation. Simulating the capacitance–voltage characteristics by solving the three-dimensional time-dependent master equation with the same width of the DOS as obtained from steady-state modeling does not lead to agreement either. Using a different type of lattice or a different type of hopping rate did not lead to any significant improvement. However, taking the same reduced width of the Gaussian DOS as obtained in the dark-injection modeling of Chapter 3 leads to a very satisfactory agreement at all considered frequencies. We therefore concluded that the picture about charge-carrier relaxation obtained from impedance-spectroscopy modeling is very similar to that obtained from dark-injection modeling. The consistency of both pictures emphasizes the apparent difference in the modeling of stationary and non-stationary charge transport in disordered organic semiconductors and the need of a better understanding of the shape of the DOS.

In *Chapter 5* we showed that kinetic Monte Carlo modeling of the molecular-scale electronic processes leading to electroluminescence in a multilayer white hybrid OLED stack is feasible. A satisfactory description of the current-density voltage characteristics was obtained using a set of device parameters obtained from separate studies of the materials in the stack. We presented results for the color-resolved emission profile reconstructed with nanometer-scale precision from the measured angle- and polarization-dependent emission. After including exciton transfer from the red- to the green-emitting layer, the simulated emission profile agreed quite well with the reconstructed profile. We therefore concluded that exciton transfer from red to green is essential to obtain the white emission of this OLED. We could obtain an estimate of the efficiency loss of the OLED due to lost excitons generated in the interlayer that separates the green phosphorescent from the blue fluorescent layer. However, this efficiency loss appears to be insufficient to account for the difference in the calculated and measured external quantum efficiency. We concluded therefore that it is

likely that another loss channel is present. We found that the emission profile is confined to nanometer-sized regions at interfaces and that the exciton generation is strongly inhomogeneous. Both are expected to make this OLED prone to degradation. From an analysis of the sensitivity of the current and the color of the light emission to the specific values of the material parameters we concluded that only a few parameters are relevant, but that the sensitivity to these parameters can then be very large.

In *Chapter 6* we continued our investigation of exciton processes in the OLED of Chapter 5 by including exciton quenching. Exciton-quenching processes decrease the efficiency of OLEDs at high current density and brightness, an effect that is called roll-off. In particular, we included triplet exciton-polaron quenching (TPQ) and triplet-triplet exciton annihilation (TTA) by assuming that immediate exciton quenching occurs when a triplet exciton and a polaron (TPQ), or two triplet excitons (TTA), appear on nearest-neighbor sites. From our simulations we concluded that the initial increase of the internal quantum efficiency (IQE) with increasing current density at low current density, the roll-on, can be largely attributed to the decreased formation of non-radiative excitons in the interlayer separating the blue and green layer. The included exciton quenching indeed leads to a roll-off in the IQE at high current density, which is in the considered current-density range completely dominated by TPQ. However, this roll-off occurs at a much larger current density than found in the experiment. We concluded that for a better description of the roll-off long-range exciton-quenching processes should be accounted for.

OUTLOOK

In the last twenty years, the Gaussian disorder model has been established as the most successful model for charge transport in disordered organic semiconductors. The most important parameters in this model are the width of the Gaussian DOS, the intersite hopping rate, and the intersite distance. These parameters are usually found from fits of calculated to measured charge transport properties. Our investigation of charge-carrier relaxation in Chapter 3 and Chapter 4 shows that the shape of the DOS may, at least for the organic semiconductor considered by us, be more complicated than a single Gaussian. It appears that non-stationary transport, for which charge-carrier relaxation is important, should be described with a narrower DOS than stationary transport. We suggested that states with energies in the tail of the DOS are important for transport close to equilibrium, while states with energies at the center of the DOS control charge-carrier relaxation effects. The discrepancy between the modeling of stationary and non-stationary transport could then be resolved by a DOS composed of a narrow Gaussian at its center and a tail described by a

broader Gaussian. We propose that other types of experiments, like thermally stimulated current measurements[139–141], by which the tail of the DOS can be studied directly, or transient photocurrent measurements, are performed to shed additional light on this matter[135].

A full *ab-initio* description of charge transport in disordered organic semiconductors appears to be within reach. The influence of a realistic (molecular scale) morphology obtained by *ab-initio* modeling on charge transport has been investigated[162]. In the Gaussian disorder model, the influence of the morphology is only accounted for by assigning random energies to the sites taken from a Gaussian DOS. In the correlated Gaussian disorder model, spatial correlations in the energies are included, supposedly cause by randomly oriented dipoles. Ideally, one should obtain the morphology and the resulting site energies from molecular-dynamics simulations of the thin-film growth of the organic semiconductor[171]. However, considering the typical organic layer thickness of 100 nm, such molecular-dynamics simulations will be too time-consuming for a complete OLED stack. A recently developed stochastic approach[172] may allow one to use the information about the morphology obtained by molecular-dynamics simulations for a small (typically $10\times10\times10$ nm^3) system to generate realistic morphologies for much larger systems. In addition, *ab-initio* calculations of charge-transfer rates can be performed by using density-functional theory or other modern quantum-chemistry methods. Also in this case, one can apply a stochastic approach to use the information about charge-transfer rates calculated for small systems in the generation of rates for much larger systems[172]. Similar approaches can in principle be used to calculate Förster and Dexter transfer rates for excitons as well as transfer rates that involve exciton quenching, although such calculations will have a much higher level of complexity. The ultimate goal in OLED modeling would be to combine morphologies, rates for charge transfer, exciton transfer, and exciton quenching obtained from *ab-initio* calculations in fully predictive kinetic Monte Carlo simulations of all relevant electronic processes in complete OLED stacks.

BIBLIOGRAPHY

[1] T. Sekitani, H. Nakajima, H. Maeda, T. Fukushima, T. Aida, K. Hata, and T. Someya. Stretchable active-matrix organic light-emitting diode display using printable elastic conductors. *Nat. Mater.*, 8(6):494–499, 2009. doi:10.1038/nmat2459. (p. 1)

[2] M. Pope, H. P. Kallmann, and P. Magnante. Electroluminescence in organic crystals. *J. Chem. Phys.*, 38(8):2042–2043, 1963. doi:10.1063/1.1733929. (p. 1)

[3] W. Helfrich and W. G. Schneider. Recombination radiation in anthracene crystals. *Phys. Rev. Lett.*, 14:229–231, 1965. doi:10.1103/PhysRevLett.14.229. (p. 1)

[4] C. W. Tang and S. A. VanSlyke. Organic electroluminescent diodes. *Appl. Phys. Lett.*, 51(12):913–915, 1987. doi:10.1063/1.98799. (p. 1)

[5] J. H. Burroughes, D. D. C. Bradley, A. R. Brown, R. N. Marks, K. Mackay, R. H. Friend, P. L. Burns, and A. B. Holmes. Light-emitting diodes based on conjugated polymers. *Nature*, 347(6293):539–541, 1990. doi:10.1038/347539a0. (p. 1)

[6] R. Friend, J. Burroughes, and T. Shimoda. Polymer diodes. *Physics world*, 12(6):35–40, 1999. (p. 1)

[7] J. Kido. Organic displays. *Physics World*, 12(3):27–29, 1999. (p. 1)

[8] C. K. Chiang, C. R. Fincher, Y. W. Park, A. J. Heeger, H. Shirakawa, E. J. Louis, S. C. Gau, and A. G. MacDiarmid. Electrical conductivity in doped polyacetylene. *Phys. Rev. Lett.*, 39:1098–1101, 1977. doi:10.1103/PhysRevLett.39.1098. (p. 1)

[9] W. Brütting, J. Frischeisen, B. J. Schmidt, Tobias D. andScholz, and C. Mayr. Device efficiency of organic light-emitting diodes: Progress by improved light outcoupling. *Physica Status Solidi A*, 210(1):44–65, 2013. ISSN 1862-6319. doi:10.1002/pssa.201228320. (p. 2, 6)

[10] S. Reineke, F. Lindner, G. Schwartz, N. Seidler, K. Walzer, B. Lussem, and K. Leo. White organic light-emitting diodes with fluorescent tube efficiency. *Nature*, 459(7244):234–238, 2009. doi:10.1038/nature08003. (p. 2, 68)

[11] M. Mesta, M. Carvelli, R. J. de Vries, H. van Eersel, J. J. M. van der Holst, M. Schober, M. Furno, B. Lüssem, K. Leo, P. Loebl, R. Coehoorn, and P. A. Bobbert. Molecular-scale simulation of electroluminescence in a multilayer white organic light-emitting diode. *Nature Mater.*, 12:652, 2013. doi:10.1038/nmat3622. (p. 2, 48)

[12] S. Reineke, M. Thomschke, B. Lüssem, and K. Leo. White organic light-emitting diodes: Status and perspective. *Rev. Mod. Phys.*, 85:1245–1293, 2013. doi:10.1103/RevModPhys.85.1245. (p. 2, 7)

[13] M. Pope and C. E. Swenberg. *Electronic processes in organic crystals and polymers*. Oxford University Press, 1999. (p. 2, 9, 13, 26, 29, 98)

[14] Y. Kawamura, K. Goushi, J. Brooks, J. J. Brown, H. Sasabe, and C. Adachi. 100% phosphorescence quantum efficiency of ir(iii) complexes in organic semiconductor films. *Appl. Phys. Lett.*, 86(7):071104, 2005. doi:10.1063/1.1862777. (p. 2, 5, 98)

[15] S.-J. Su, E. Gonmori, H. Sasabe, and J. Kido. Highly efficient organic blue- and white-light-emitting devices having a carrier- and exciton-confining structure for reduced efficiency roll-off. *Advanced Materials*, 20(21):4189–4194, 2008. doi:10.1002/adma.200801375. (p. 2)

[16] H. Ishii and K. Seki. *Conjugated polymer and molecular interfaces*, chapter Energy level alignment at organic-metal interfaces. CRC Press, 2001. ISBN 978-0-8247-0588-6. doi:10.1201/9780203910870.ch10. (p. 3)

[17] I. D. Parker. Carrier tunneling and device characteristics in polymer light-emitting diodes. *J. Appl. Phys.*, 75(3):1656–1666, 1994. doi:10.1063/1.356350. (p. 3)

[18] N. Koch, S. Duhm, J. P. Rabe, A. Vollmer, and R. L. Johnson. Optimized hole injection with strong electron acceptors at organic-metal interfaces. *Phys. Rev. Lett.*, 95:237601, 2005. doi:10.1103/PhysRevLett.95.237601. (p. 3)

[19] J. Guo, N. Koch, S. L. Bernasek, and J. Schwartz. Enhanced hole injection in a polymer light emitting diode using a small molecule monolayer bound to the anode. *Chem. Phys. Lett.*, 426(4-6):370 – 373, 2006. doi:10.1016/j.cplett.2006.05.129. (p. 3)

[20] J. Kido and T. Matsumoto. Bright organic electroluminescent devices having a metal-doped electron-injecting layer. *Appl. Phys. Lett.*, 73(20):2866–2868, 1998. doi:10.1063/1.122612. (p. 3)

[21] B. Lüssem, M. Riede, and K. Leo. Doping of organic semiconductors. *physica status solidi (a)*, 210(1):9–43, 2013. doi:10.1002/pssa.201228310. (p. 3)

[22] P. K. H. Ho, J.-S. Kim, J. H. Burroughes, H. Becker, S. F. Y. Li, T. M. Brown, F. Cacialli, and R. H. Friend. Molecular-scale interface engineering for polymer light-emitting diodes. *Nature*, 404(6777):481–484, 2000. ISSN 0028-0836. doi:10.1038/35006610. (p. 4)

[23] M. Knupfer. Exciton binding energies in organic semiconductors. *Applied Physics A*, 77(5):623–626, 2003. doi:10.1007/s00339-003-2182-9. (p. 4)

[24] C. Kittel. *Introduction to Soild State Physics*. John Wiley and Sons, Inc., New York, USA, 7 edition, 1995. ISBN 0-471-11181-3. (p. 4)

[25] J.-L. Brédas, D. Beljonne, V. Coropceanu, and J. Cornil. Charge-transfer and energy-transfer processes in π-conjugated oligomers and polymers: A molecular picture. *Chem. Rev.*, 104(11):4971–5004, 2004. doi:10.1021/cr040084k. (p. 4)

[26] C. Adachi, M. A. Baldo, M. E. Thompson, and S. R. Forrest. Nearly 100% internal phosphorescence efficiency in an organic light-emitting device. *J. Appl. Phys.*, 90(10):5048–5051, 2001. doi:10.1063/1.1409582. (p. 5, 98)

[27] N. C. Greenham, R. H. Friend, and D. D. C. Bradley. Angular dependence of the emission from a conjugated polymer light-emitting diode: Implications for efficiency calculations. *Advanced Materials*, 6(6):491–494, 1994. doi:10.1002/adma.19940060612. (p. 6)

[28] C.-H. Hsiao, Y.-H. Chen, T.-C. Lin, C.-C. Hsiao, and J.-H. Lee. Recombination zone in mixed-host organic light-emitting devices. *Appl. Phys. Lett.*, 89(16):163511, 2006. doi:10.1063/1.2361266. (p. 6)

[29] C. Murawski, K. Leo, and M. C. Gather. Efficiency roll-off in organic light-emitting diodes. *Advanced Materials*, 25(47):6801–6827, 2013. doi:10.1002/adma.201301603. (p. 6)

[30] M. A. Baldo, D. F. O'Brien, Y. You, A. Shoustikov, S. Sibley, M. E. Thompson, and S. R. Forrest. Highly efficient phosphorescent emission from organic electroluminescent devices. *Nature*, 395(6698):151–154, 1998. doi:10.1038/25954. (p. 6, 68, 98)

[31] M. A. Baldo, C. Adachi, and S. R. Forrest. Transient analysis of organic electrophosphorescence. ii. transient analysis of triplet-triplet annihilation. *Phys. Rev. B*, 62:10967–10977, 2000. doi:10.1103/PhysRevB.62.10967. (p. 6, 98, 99)

[32] J. Kalinowski, W. Stampor, J. Szmytkowski, D. Virgili, M. Cocchi, V. Fattori, and C. Sabatini. Coexistence of dissociation and annihilation of excitons on charge carriers in organic phosphorescent emitters. *Phys. Rev. B*, 74:085316, 2006. doi:10.1103/PhysRevB.74.085316. (p. 6, 99)

[33] A. Köhler and H. Bässler. Triplet states in organic semiconductors. *Materials Science and Engineering: R: Reports*, 66(4–6):71–109, 2009. doi:10.1016/j.mser.2009.09.001. (p. 7, 20)

[34] J. Kido, K. Hongawa, K. Okuyama, and K. Nagai. White light-emitting organic electroluminescent devices using the poly(n-vinylcarbazole) emitter layer doped with three fluorescent dyes. *Appl. Phys. Lett.*, 64(7):815–817, 1994. doi:10.1063/1.111023. (p. 7)

[35] Y.-H. Niu, M. Liu, J.-W. Ka, J. Bardeker, M. Zin, R. Schofield, Y. Chi, and A.-Y. Jen. Crosslinkable hole-transport layer on conducting polymer for high-efficiency white polymer light-emitting diodes. *Advanced Materials*, 19(2):300–304, 2007. doi:10.1002/adma.200502769. (p. 7)

[36] R. J. Holmes, B. W. D'Andrade, S. R. Forrest, X. Ren, J. Li, and M. E. Thompson. Efficient, deep-blue organic electrophosphorescence by guest charge trapping. *Appl. Phys. Lett.*, 83(18):3818–3820, 2003. doi:10.1063/1.1624639. (p. 7)

[37] B. Hu and F. E. Karasz. Blue, green, red, and white electroluminescence from multichromophore polymer blends. *J. Appl. Phys.*, 93(4):1995–2001, 2003. doi:10.1063/1.1536018. (p. 7)

[38] A. Köhnen, M. Irion, M. C. Gather, N. Rehmann, P. Zacharias, and K. Meerholz. Highly color-stable solution-processed multilayer woleds for lighting application. *J. Mater. Chem.*, 20:3301–3306, 2010. doi:10.1039/B924968K. (p. 7)

[39] M. Berggren, O. Inganas, G. Gustafsson, J. Rasmusson, M. R. Andersson, T. Hjertberg, and O. Wennerstrom. Light-emitting diodes with variable colours from polymer blends. *Nature*, 372(6505):444–446, 1994. doi:10.1038/372444a0. (p. 7)

[40] A. Szabo and N. S. Ostlund. *Modern quantum chemistry: introduction to advanced electronic structure theory*. Dover Publications, Mineola, New York, 1996. ISBN 0-486-69186-1. (p. 7, 25)

[41] W. Barford. *Electronic and optical properties of conjugated polymers*. Oxford University Press, New York, 2005. (p. 8)

[42] D. J. Griffiths. *Introduction to quantum mechanics*. Pearson Education, New Jersey, second edition, 2005. ISBN 0-13-191175-9. (p. 8, 22, 23)

[43] H. Bässler and A. Köhler. Charge transport in organic semiconductors. In *Unimolecular and Supramolecular Electronics I*, volume 312 of *Topics in Current Chemistry*, pages 1–65. Springer Berlin Heidelberg, 2012. doi:10.1007/128_2011_218. (p. 9, 10, 13, 15, 68)

[44] H. Böttger and V. V. Bryksin. Hopping conductivity in ordered and disordered solids (i). *Phys. Stat. Sol. B*, 78:9–56, 1976. doi:10.1002/pssb.2220780102. (p. 9)

[45] V. Coropceanu, J. Cornil, D. A. da Silva Filho, Y. Olivier, R. Silbey, and J.-L. Brédas. Charge transport in organic semiconductors. *Chem. Rev.*, 107 (4):926–952, 2007. doi:10.1021/cr050140x. (p. 9, 11, 58)

[46] Y. C. Cheng, R. J. Silbey, D. A. da Silva Filho, J. P. Calbert, J. Cornil, and J. L. Brédas. Three-dimensional band structure and bandlike mobility in oligoacene single crystals: A theoretical investigation. *J. Chem. Phys.*, 118 (8):3764–3774, 2003. doi:10.1063/1.1539090. (p. 9)

[47] S. Fratini and S. Ciuchi. Bandlike motion and mobility saturation in organic molecular semiconductors. *Phys. Rev. Lett.*, 103:266601, 2009. doi:10.1103/PhysRevLett.103.266601. (p. 9)

[48] J. J. M. van der Holst, F. W. A. van Oost, R. Coehoorn, and P. A. Bobbert. Monte Carlo study of charge transport in organic sandwich-type single-carrier devices: Effects of coulomb interactions. *Phys. Rev. B*, 83:085206, 2011. doi:10.1103/PhysRevB.83.085206. (p. 10, 36, 48, 49, 72, 83, 84)

[49] A. V. Nenashev, F. Jansson, J. O. Oelerich, D. Huemmer, A. V. Dvurechenskii, F. Gebhard, and S. D. Baranovskii. Advanced percolation solution for hopping conductivity. *Phys. Rev. B*, 87:235204, 2013. doi:10.1103/PhysRevB.87.235204. (p. 10)

[50] J. Cottaar, L. J. A. Koster, R. Coehoorn, and P. A. Bobbert. Scaling theory for percolative charge transport in disordered molecular semiconductors. *Phys. Rev. Lett.*, 107:136601, 2011. doi:10.1103/PhysRevLett.107.136601. (p. 10, 54, 62, 64, 72)

[51] M. A. Lampert and P. Mark. *Current injection in solids*. Electrical science series. Academic Press, New York, NY, 1970. (p. 10, 12)

[52] N. F. Mott and R. W. Gurney. *Electronic processes in ionic crystals*. Oxford University Press, New York, 1940. (p. 11)

[53] R. Coehoorn and P. A. Bobbert. Effects of Gaussian disorder on charge carrier transport and recombinationin organic semiconductors. *Phys. Status Solidi A*, 209(12):2354–2377, 2012. doi:10.1002/pssa.201228387. (p. 11, 12, 13, 16)

[54] B. Ruhstaller, S. A. Carter, S. Barth, H. Riel, W. Riess, and J. C. Scott. Transient and steady-state behavior of space charges in multilayer organic light-emitting diodes. *J. Appl. Phys.*, 89(8):4575–4586, 2001. doi:10.1063/1.1352027. (p. 11, 12)

[55] W. Brütting, S. Berleb, and A. G. Mückl. Device physics of organic light-emitting diodes based on molecular materials. *Organic Electronics*, 2(1):1 – 36, 2001. ISSN 1566-1199. doi:10.1016/S1566-1199(01)00009-X. (p. 12)

[56] P. N. Murgatroyd. Theory of space-charge-limited current enhanced by frenkel effect. *J. Phys. D: Appl. Phys.*, 3(2):151, 1970. doi:10.1088/0022-3727/3/2/308. (p. 12)

[57] N. W. Ashcroft and N. D. Mermin. *Solid state physics*. Holt, Rinehart and Winston, New York, 1976. (p. 12, 33)

[58] Y. Roichman and N. Tessler. Generalized einstein relation for disordered semiconductors - implications for device performance. *Appl. Phys. Lett.*, 80(11):1948, 2002. doi:10.1063/1.1461419. (p. 12, 42)

[59] J. J. M. van der Holst, M. A. Uijttewaal, B. Ramachandhran, R. Coehoorn, P. A. Bobbert, G. A. de Wijs, and R. A. de Groot. Modeling and analysis of the three-dimensional current density in sandwich-type single-carrier devices of disordered organic semiconductors. *Phys. Rev. B*, 79(8):085203, 2009. doi:10.1103/physrevb.79.085203. (p. 13, 18, 30, 31, 42, 47, 48)

[60] E. Knapp. *Numerical methods for comprehensive characterization of charge transport in organic light-emitting devices*. PhD thesis, Eidgenössische Technische Hochschule (ETH), Zürich, 2013. (p. 13)

[61] H. Bässler. Charge transport in disordered organic photoconductors. *Phys. Stat. Sol. B*, 175:15, 1993. doi:10.1002/pssb.2221750102. (p. 13, 14, 15, 34, 40, 58)

[62] S. L. M. van Mensfoort, S. I. E. Vulto, R. A. J. Janssen, and R. Coehoorn. Hole transport in polyfluorene-based sandwich-type devices: Quantitative analysis of the role of energetic disorder. *Phys. Rev. B*, 78:085208, 2008. doi:10.1103/PhysRevB.78.085208. (p. 13, 15, 40, 41, 43, 45, 46, 48, 50, 58, 60, 62, 65)

[63] E. Knapp, R. Häusermann, H. U. Schwarzenbach, and B. Ruhstaller. Numerical simulation of charge transport in disordered organic semiconductor devices. *J. Appl. Phys.*, 108(5):054504, 2010. doi:10.1063/1.3475505. (p. 13)

[64] I. N. Hulea, H. B. Brom, A. J. Houtepen, D. Vanmaekelbergh, J. J. Kelly, and E. A. Meulenkamp. Wide energy-window view on the density of states and hole mobility in poly(p-phenylene vinylene). *Phys. Rev. Lett.*, 93:166601, 2004. doi:10.1103/PhysRevLett.93.166601. (p. 13)

[65] A. Miller and E. Abrahams. Impurity conduction at low concentrations. *Phys. Rev.*, 120:745–755, 1960. doi:10.1103/PhysRev.120.745. (p. 13, 48, 60, 72, 83)

[66] I. I. Fishchuk, A. Kadashchuk, S. T. Hoffmann, S. Athanasopoulos, J. Genoe, H. Bässler, and A. Köhler. Unified description for hopping transport in organic semiconductors including both energetic disorder and polaronic contributions. *Phys. Rev. B*, 88:125202, 2013. doi:10.1103/PhysRevB.88.125202. (p. 14)

[67] S. T. Hoffmann, F. Jaiser, A. Hayer, H. Bässler, T. Unger, S. Athanasopoulos, D. Neher, and A. Köhler. How do disorder, reorganization, and localization influence the hole mobility in conjugated copolymers? *J. Am. Chem. Soc.*, 135(5):1772–1782, 2013. doi:10.1021/ja308820j. (p. 14)

[68] J. Veres, S. Ogier, S. Leeming, D. Cupertino, and S. Mohialdin Khaffaf. Low-k insulators as the choice of dielectrics in organic field-effect transistors. *Adv. Funct. Mater.*, 13(3):199–204, 2003. doi:10.1002/adfm.200390030. (p. 15)

[69] P. W. M. Blom, M. J. M. de Jong, and M. G. van Munster. Electric-field and temperature dependence of the hole mobility in poly(p-phenylene vinylene). *Phys. Rev. B*, 55:R656–R659, 1997. doi:10.1103/PhysRevB.55.R656. (p. 15)

[70] S. Gambino, I. Samuel, H. Barcena, and P. Burn. Electric field and temperature dependence of the hole mobility in a bis-fluorene cored dendrimer. *Org. Electron.*, 9(2):220–226, 2008. doi:10.1016/j.orgel.2007.11.002. (p. 15)

[71] H. C. F. Martens, P. W. M. Blom, and H. F. M. Schoo. Comparative study of hole transport in poly(p-phenylene vinylene) derivatives. *Phys. Rev. B*, 61:7489–7493, 2000. doi:10.1103/PhysRevB.61.7489. (p. 15)

[72] J. C. Blakesley, H. S. Clubb, and N. C. Greenham. Temperature-dependent electron and hole transport in disordered semiconducting polymers: Analysis of energetic disorder. *Phys. Rev. B*, 81:045210, 2010. doi:10.1103/PhysRevB.81.045210. (p. 15)

[73] A. J. Mozer, P. Denk, M. C. Scharber, H. Neugebauer, N. S. Sariciftci, P. Wagner, L. Lutsen, and D. Vanderzande. Novel regiospecific mdmo-ppv copolymer with improved charge transport for bulk heterojunction solar cells. *J. Phys. Chem. B*, 108(17):5235–5242, 2004. doi:10.1021/jp049918t. (p. 15)

[74] J. X. Mack, L. B. Schein, and A. Peled. Hole mobilities in hydrazone-polycarbonate dispersions. *Phys. Rev. B*, 39:7500–7508, 1989. doi:10.1103/PhysRevB.39.7500. (p. 15)

[75] P. E. Parris, V. M. Kenkre, and D. H. Dunlap. Nature of charge carriers in disordered molecular solids: Are polarons compatible with observations?

Phys. Rev. Lett., 87:126601, 2001. doi:10.1103/PhysRevLett.87.126601. (p. 15)

[76] M. R. Cavallari, V. R. Zanchin, C. A. Amorim, G. dos Santos, F. J. Fonseca, A. M. Andrade, and S. Mergulhão. Time-of-flight technique limits of applicability for thin-films of π-conjugated polymers. In *Symposium U – Charge Generation/Transport in Organic Semiconductor Materials*, volume 1402 of *MRS Online Proceedings Library*, 2012. doi:10.1557/opl.2012.262. (p. 15)

[77] K. D. Meisel, H. Vocks, and P. A. Bobbert. Polarons in semiconducting polymers: Study within an extended holstein model. *Phys. Rev. B*, 71: 205206, 2005. doi:10.1103/PhysRevB.71.205206. (p. 15)

[78] C. Tanase, E. J. Meijer, P. W. M. Blom, and D. M. de Leeuw. Unification of the hole transport in polymeric field-effect transistors and light-emitting diodes. *Phys. Rev. Lett.*, 91:216601, 2003. doi:10.1103/PhysRevLett.91.216601. (p. 15, 40, 58)

[79] W. F. Pasveer, J. Cottaar, C. Tanase, R. Coehoorn, P. A. Bobbert, P. W. M. Blom, D. M. de Leeuw, and M. A. J. Michels. Unified description of charge-carrier mobilities in disordered semiconducting polymers. *Phys. Rev. Lett.*, 94:206601, 2005. doi:10.1103/PhysRevLett.94.206601. (p. 16, 30, 40, 46, 48, 58, 68)

[80] Y. Gartstein and E. Conwell. High-field hopping mobility in molecular systems with spatially correlated energetic disorder. *Chem. Phys. Lett.*, 245:351–358, 1995. doi:10.1016/0009-2614(95)01031-4. (p. 16, 40)

[81] D. H. Dunlap, P. E. Parris, and V. M. Kenkre. Charge-dipole model for the universal field dependence of mobilities in molecularly doped polymers. *Phys. Rev. Lett.*, 77:542–545, 1996. doi:10.1103/PhysRevLett.77.542. (p. 16)

[82] S. V. Novikov, D. H. Dunlap, V. M. Kenkre, P. E. Parris, and A. V. Vannikov. Essential role of correlations in governing charge transport in disordered organic materials. *Phys. Rev. Lett.*, 81:4472–4475, 1998. doi:10.1103/physrevlett.81.4472. (p. 16, 40)

[83] M. Bouhassoune, S. van Mensfoort, P. Bobbert, and R. Coehoorn. Carrier-density and field-dependent charge-carrier mobility in organic semiconductors with correlated Gaussian disorder. *Org. Elec.*, 10:437 – 445, 2009. doi:10.1016/j.orgel.2009.01.005. (p. 16, 40, 68, 84, 86)

[84] H. Scher and E. W. Montroll. Anomalous transit-time dispersion in amorphous solids. *Phys. Rev. B*, 12:2455–2477, 1975. doi:10.1103/PhysRevB.12.2455. (p. 17, 41)

[85] J. Nelson. Continuous-time random-walk model of electron transport in nanocrystalline tio$_2$ electrodes. *Phys. Rev. B*, 59:15374–15380, 1999. doi:10.1103/PhysRevB.59.15374. (p. 17)

[86] S. D. Baranovskii, H. Cordes, F. Hensel, and G. Leising. Charge-carrier transport in disordered organic solids. *Phys. Rev. B*, 62:7934–7938, 2000. doi:10.1103/PhysRevB.62.7934. (p. 17)

[87] W. C. Germs, J. J. M. van der Holst, S. L. M. van Mensfoort, P. A. Bobbert, and R. Coehoorn. Modeling of the transient mobility in disordered organic semiconductors with a Gaussian density of states. *Phys. Rev. B*, 84: 165210, 2011. doi:10.1103/PhysRevB.84.165210. (p. 17, 41, 42, 43, 59, 60, 61, 62, 63, 64)

[88] J. M. Martin Klessinger. *Excited States and Photo-Chemistry of Organic Molecules*. Wiley-VCH, 1995. ISBN 0471185760. (p. 21, 22)

[89] M. Kasha. Characterization of electronic transitions in complex molecules. *Discuss. Faraday Soc.*, 9:14–19, 1950. doi:10.1039/DF9500900014. (p. 21)

[90] A. Einstein. Strahlungs-Emission und Absorption nach der Quantentheorie. *Deutsche Physikalische Gesellschaft*, 18:318–323, 1916. (p. 22)

[91] S. J. Strickler and R. A. Berg. Relationship between absorption intensity and fluorescence lifetime of molecules. *The Journal of Chemical Physics*, 37 (4):814–822, 1962. doi:10.1063/1.1733166. (p. 23)

[92] T. Förster. 10th spiers memorial lecture. transfer mechanisms of electronic excitation. *Discuss. Faraday Soc.*, 27:7–17, 1959. doi:10.1039/DF9592700007. (p. 24)

[93] T. Förster. Zwischenmolekulare energiewanderung und fluoreszenz. *Annalen der Physik*, 437(1-2):55–75, 1948. doi:10.1002/andp.19484370105. (p. 24, 26)

[94] B. Valeur and M. N. Berberan-Santos. *Excitation Energy Transfer*, pages 213–261. Wiley-VCH Verlag GmbH & Co. KGaA, 2012. ISBN 9783527650002. doi:10.1002/9783527650002.ch8. (p. 25)

[95] D. L. Dexter. A theory of sensitized luminescence in solids. *J. Chem. Phys.*, 21(5):836–850, 1953. doi:10.1063/1.1699044. (p. 27)

[96] E. Wigner and E. Witmer. About the structure of the diatomic mulecule spectra according to quantum mechanics. *Z. Phys*, 51:859–886, 1928. (p. 28)

[97] R. E. Kellogg. Radiationless intermolecular energy transfer. iv. triplet—triplet annihilation. *J. Chem. Phys.*, 41(10):3046–3047, 1964. doi:10.1063/1.1725673. (p. 29)

[98] W. Staroske, M. Pfeiffer, K. Leo, and M. Hoffmann. Single-step triplet-triplet annihilation: An intrinsic limit for the high brightness efficiency of phosphorescent organic light emitting diodes. *Phys. Rev. Lett.*, 98:197402, 2007. doi:10.1103/PhysRevLett.98.197402. (p. 29)

[99] J. Kalinowski. *Organic Light-Emitting Diodes: Principles, Characteristics, and Processes*. Marcel Dekker, New York, 2005. ISBN 0-8247-5947-8. (p. 29)

[100] S. Alexander, J. Bernasconi, W. R. Schneider, and R. Orbach. Excitation dynamics in random one-dimensional systems. *Rev. Mod. Phys.*, 53:175–198, 1981. doi:10.1103/RevModPhys.53.175. (p. 30)

[101] M. Szymański, B. Łuszczyńska, and D. Djurado. Modeling the transient space-charge-limited current response of organic semiconductor diodes using the master equation approach. *IEEE J. Sel. Topics Quantum Electron.*, 19:7800107, 2013. doi:10.1109/jstqe.2013.2246775. (p. 31, 42)

[102] J. Cottaar. *Modeling of charge-transport processes for predictive simulation of OLEDs*. PhD thesis, Eindhoven University of Technology, 2012. (p. 31)

[103] H. van der Vorst. Bi-CGSTAB: A fast and smoothly converging variant of bi-cg for the solution of nonsymmetric linear systems. *SIAM Journal on Scientific and Statistical Computing*, 13(2):631–644, 1992. doi:10.1137/0913035. (p. 33)

[104] The NAG Fortran Library, The Numerical Algorithms Group (NAG), Oxford, United Kingdom. www.nag.com. (p. 33)

[105] N. Metropolis and S. Ulam. The Monte Carlo method. *J. Am. Stat. Assoc.*, 44(247):pp. 335–341, 1949. doi:10.2307/2280232. (p. 34)

[106] N. Metropolis, A. W. Rosenbluth, M. N. Rosenbluth, A. H. Teller, and E. Teller. Equation of state calculations by fast computing machines. *J. Chem. Phys.*, 21(6):1087–1092, 1953. doi:10.1063/1.1699114. (p. 34)

[107] W. M. Young and E. W. Elcock. Monte Carlo studies of vacancy migration in binary ordered alloys: I. *Proceedings of the Physical Society*, 89(3):735, 1966. doi:10.1088/0370-1328/89/3/329. (p. 34)

[108] A. Bortz, M. Kalos, and J. Lebowitz. A new algorithm for Monte Carlo simulation of ising spin systems. *J. Comput. Phys.*, 17(1):10 – 18, 1975. doi:10.1016/0021-9991(75)90060-1. (p. 34)

[109] D. T. Gillespie. A general method for numerically simulating the stochastic time evolution of coupled chemical reactions. *J. Comput. Phys.*, 22(4): 403 – 434, 1976. doi:10.1016/0021-9991(76)90041-3. (p. 34)

[110] B. Meng and W. H. Weinberg. Monte Carlo simulations of temperature programmed desorption spectra. *J. Chem. Phys.*, 100(7):5280–5289, 1994. doi:10.1063/1.467192. (p. 34)

[111] G. Schönherr, H. Bässler, and M. Silver. Dispersive hopping transport via sites having a Gaussian distribution of energies. *Philosophical Magazine Part B*, 44(1):47–61, 1981. doi:10.1080/01418638108222366. (p. 34)

[112] H. Houili, E. Tutiš, I. Batistić, and L. Zuppiroli. Investigation of the charge transport through disordered organic molecular heterojunctions. *J. Appl. Phys.*, 100(3):033702, 2006. doi:10.1063/1.2222041. (p. 34)

[113] H. van Eersel, P. A. Bobbert, R. A. J. Janssen, and R. Coehoorn. Monte carlo study of efficiency roll-off of phosphorescent organic light-emitting diodes: Evidence for dominant role of triplet-polaron quenching. *Appl. Phys. Lett.*, 105(14):143303, 2014. doi:10.1063/1.4897534. (p. 37, 100)

[114] Y. Roichman and N. Tessler. Charge transport in conjugated polymers: The influence of charge concentration. *Synth. Met.*, 135:443, 2003. doi:10.1016/s0379-6779(02)00596-9. (p. 40)

[115] O. Rubel, S. D. Baranovskii, P. Thomas, and S. Yamasaki. Concentration dependence of the hopping mobility in disordered organic solids. *Phys. Rev. B*, 69:014206, 2004. doi:10.1103/PhysRevB.69.014206. (p. 40)

[116] S. van Mensfoort, R. de Vries, V. Shabro, H. Loebl, R. Janssen, and R. Coehoorn. Electron transport in the organic small-molecule material BAlq – the role of correlated disorder and traps. *Organic Electronics*, 11(8):1408 – 1413, 2010. doi:10.1016/j.orgel.2010.05.014. (p. 40, 72, 85)

[117] S. van Mensfoort, R. de Vries, V. Shabro, H. Loebl, R. Janssen, and R. Coehoorn. Electron transport in the organic small-molecule material BAlq: the role of correlated disorder and traps. *Org. Elec.*, 11(8):1408 – 1413, 2010. doi:10.1016/j.orgel.2010.05.014. (p. 40, 72)

[118] S. L. M. van Mensfoort, J. Billen, S. I. E. Vulto, R. A. J. Janssen, and R. Coehoorn. Electron transport in polyfluorene-based sandwich-type devices: Quantitativeanalysis of the effects of disorder and electron traps. *Phys. Rev. B*, 80:033202, 2009. doi:10.1103/PhysRevB.80.033202. (p. 40, 41, 54)

[119] G. Pfister. Hopping transport in a molecularly doped organic polymer. *Phys. Rev. B*, 16:3676, 1977. doi:10.1103/physrevb.16.3676. (p. 41)

[120] T. Kreouzis, D. Poplavskyy, S. M. Tuladhar, M. Campoy-Quiles, J. Nelson, A. J. Campbell, and D. D. C. Bradley. Temperature and field dependence of hole mobility in poly(9,9-dioctylfluorene). *Phys. Rev. B*, 73:235201, 2006. doi:10.1103/PhysRevB.73.235201. (p. 41)

[121] B. Movaghar, M. Grünewald, B. Ries, H. Bassler, and D. Würtz. Diffusion and relaxation of energy in disordered organic and inorganic materials. *Phys. Rev. B*, 33:5545–5554, 1986. doi:10.1103/PhysRevB.33.5545. (p. 41)

[122] P. M. Borsenberger, L. T. Pautmeier, and H. Bässler. Nondispersive-to-dispersive charge-transport transition in disordered molecular solids. *Phys. Rev. B*, 46:12145, 1992. doi:10.1103/physrevb.46.12145. (p. 41)

[123] D. Poplavskyy and J. Nelson. Nondispersive hole transport in amorphous films of methoxy-spirofluorene-arylamine organic compound. *J. Appl. Phys.*, 93:341, 2003. doi:10.1063/1.1525866. (p. 42)

[124] D. Poplavskyy, W. Su, and F. So. Bipolar charge transport, injection, and trapping studies in a model green-emitting polyfluorene copolymer. *J. Appl. Phys.*, 98:014501, 2005. doi:10.1063/1.1941482. (p. 42)

[125] D. Poplavskyy and F. So. Bipolar carrier transport in a conjugated polymer by complex admittance spectroscopy. *J. Appl. Phys.*, 99:033707, 2006. doi:10.1063/1.2149495. (p. 42)

[126] A. Many and G. Rakavy. Theory of transient space-charge limited currents in solids in the presence of trapping. *Phys. Rev.*, 126:1980–1988, 1962. doi:10.1103/physrev.126.1980. (p. 42, 50, 51)

[127] E. Knapp and B. Ruhstaller. Numerical impedance analysis for organic semiconductors with exponential distribution of localized states. *Appl. Phys. Lett.*, 99(9):–, 2011. doi:10.1063/1.3633109. (p. 42, 59)

[128] E. Knapp and B. Ruhstaller. The role of shallow traps in dynamic characterization of organic semiconductor devices. *J. Appl. Phys.*, 112(2):024519, 2012. doi:10.1063/1.4739303. (p. 42)

[129] R. Coehoorn and S. L. M. van Mensfoort. Effects of disorder on the current density and recombination profile in organic light-emitting diodes. *Phys. Rev. B*, 80:085302, 2009. doi:10.1103/PhysRevB.80.085302. (p. 42, 46, 68)

[130] R. J. de Vries, S. L. M. van Mensfoort, R. A. J. Janssen, and R. Coehoorn. Relation between the built-in voltage in organic light-emitting diodes and the zero-field voltage as measured by electroabsorption. *Phys. Rev. B*, 81: 125203, 2010. doi:10.1103/PhysRevB.81.125203. (p. 43, 50, 60)

[131] R. Coehoorn, W. F. Pasveer, P. A. Bobbert, and M. A. J. Michels. Charge-carrier concentration dependence of the hopping mobility in organic materials with Gaussian disorder. *Phys. Rev. B*, 72:155206, 2005. doi:10.1103/PhysRevB.72.155206. (p. 54)

[132] M. C. J. M. Vissenberg and M. Matters. Theory of the field-effect mobility in amorphous organic transistors. *Phys. Rev. B*, 57:12964–12967, 1998. doi:10.1103/PhysRevB.57.12964. (p. 58)

[133] R. J. de Vries, S. L. M. van Mensfoort, V. Shabro, S. I. E. Vulto, R. A. J. Janssen, and R. Coehoorn. Analysis of hole transport in a polyfluorene-based copolymer - evidence for the absence of correlated disorder. *Appl. Phys. Lett.*, 94(16):–, 2009. doi:http://dx.doi.org/10.1063/1.3119317. (p. 58)

[134] R. J. de Vries, A. Badinski, R. A. J. Janssen, and R. Coehoorn. Extraction of the materials parameters that determine the mobility in disordered organic semiconductors from the current-voltage characteristics: Accuracy and limitations. *J. Appl. Phys.*, 113(11):–, 2013. doi:http://dx.doi.org/10.1063/1.4795588. (p. 58)

[135] R. C. I. MacKenzie, C. G. Shuttle, G. F. Dibb, N. Treat, E. von Hauff, M. J. Robb, C. J. Hawker, M. L. Chabinyc, and J. Nelson. Interpreting the density of states extracted from organic solar cells using transient photocurrent measurements. *The Journal of Physical Chemistry C*, 117(24): 12407–12414, 2013. doi:10.1021/jp4010828. (p. 59, 108)

[136] M. Mesta, C. Schaefer, J. de Groot, J. Cottaar, R. Coehoorn, and P. A. Bobbert. Charge-carrier relaxation in disordered organic semiconductors studied by dark injection: Experiment and modeling. *Phys. Rev. B*, 88: 174204, 2013. doi:10.1103/PhysRevB.88.174204. (p. 59, 61, 63, 64, 65)

[137] S. L. M. van Mensfoort and R. Coehoorn. Determination of injection barriers in organic semiconductor devices from capacitance measurements. *Phys. Rev. Lett.*, 100:086802, 2008. doi:10.1103/PhysRevLett.100.086802. (p. 60)

[138] R. A. Marcus. Electron transfer reactions in chemistry. theory and experiment. *Rev. Mod. Phys.*, 65:599–610, 1993. doi:10.1103/RevModPhys.65.599. (p. 63, 72)

[139] A. G. Werner, J. Blochwitz, M. Pfeiffer, and K. Leo. Field dependence of thermally stimulated currents in alq3. *J. Appl. Phys.*, 90(1):123–125, 2001. doi:10.1063/1.1378813. (p. 65, 108)

[140] W. Weise, T. Keith, N. von Malm, and H. von Seggern. Trap concentration dependence of thermally stimulated currents in small molecule organic materials. *Phys. Rev. B*, 72:045202, 2005. doi:10.1103/PhysRevB.72.045202. (p. 65, 108)

[141] P. Yu, A. Migan-Dubois, J. Alvarez, A. Darga, V. Vissac, D. Mencaraglia, Y. Zhou, and M. Krueger. Study of traps in p3ht:pcbm based organic

solar cells using fractional thermally stimulated current (ftsc) technique. *J. Non-Cryst. Solids*, 358(17):2537 – 2540, 2012. (p. 65, 108)

[142] J. Kido, M. Kimura, and K. Nagai. Multilayer white light-emitting organic electroluminescent device. *Science*, 267(0):1332–1334, 1995. doi:10.1126/science.267.5202.1332. (p. 68)

[143] K. Walzer, B. Maennig, M. Pfeiffer, and K. Leo. Highly efficient organic devices based on electrically doped transport layers. *Chem. Rev.*, 107(4): 1233–1271, 2007. doi:10.1021/cr050156n. (p. 68)

[144] G. Schwartz, K. Fehse, M. Pfeiffer, K. Walzer, and K. Leo. Highly efficient white organic light emitting diodes comprising an interlayer to separate fluorescent and phosphorescent regions. *Appl. Phys. Lett.*, 89(0):083509, 2006. doi:10.1063/1.2338588. (p. 68, 69)

[145] S. Reineke and M. Baldo. Recent progress in the understanding of exciton dynamics within phosphorescent oleds. *Phys. Stat. Sol. A*, pages 1 – 13, 2012. doi:10.1002/pssa.201228292. (p. 68)

[146] M. Schober, M. Anderson, M. Thomschke, J. Widmer, M. Furno, R. Scholz, B. Lüssem, and K. Leo. Quantitative description of charge-carrier transport in a white organic light-emitting diode. *Phys. Rev. B*, 84:165326, 2011. doi:10.1103/PhysRevB.84.165326. (p. 68, 85, 86)

[147] S. L. M. van Mensfoort, J. Billen, M. Carvelli, S. I. E. Vulto, R. A. J. Janssen, and R. Coehoorn. Predictive modeling of the current density and radiative recombination in blue polymer-based light-emitting diodes. *J. Appl. Phys.*, 109(6):064502, 2011. doi:10.1063/1.3553412. (p. 68)

[148] H. Houili, E. Tutiš, H. Lütjens, M. Bussac, and L. Zuppiroli. Moled: Simulation of multilayer organic light emitting diodes. *Comput. Phys. Commun.*, 156(1):108, 2003. doi:10.1016/S0010-4655(03)00435-1. (p. 68)

[149] Material supplied by Novaled, AG. (p. 70)

[150] S. L. M. van Mensfoort, M. Carvelli, M. Megens, D. Wehenkel, M. Bartyzel, H. Greiner, R. A. J. Janssen, and R. Coehoorn. Measuring the light emission profile in organic light-emitting diodes with nanometre spatial resolution. *Nature Photonics*, 4(0):329–335, 2010. doi:10.1038/nphoton.2010.32. (p. 71, 81)

[151] G. Li, C. H. Kim, Z. Zhou, J. Shinar, K. Okumoto, and Y. Shirota. Combinatorial study of exciplex formation at the interface between two wide band gap organic semiconductors. *Appl. Phys. Lett.*, 88(25):253505, 2006. doi:10.1063/1.2202391. (p. 71)

[152] M. Furno, R. Meerheim, S. Hofmann, B. Lüssem, and K. Leo. Efficiency and rate of spontaneous emission in organic electroluminescent devices. *Phys. Rev. B*, 85:115205, 2012. doi:10.1103/PhysRevB.85.115205. (p. 71, 74)

[153] M. M. Mandoc, B. de Boer, G. Paasch, and P. W. M. Blom. Trap-limited electron transport in disordered semiconducting polymers. *Phys. Rev. B*, 75(19):193202, 2007. doi:10.1103/PhysRevB.75.193202. (p. 72)

[154] F. May, B. Baumeier, C. Lennartz, and D. Andrienko. Can lattice models predict the density of states of amorphous organic semiconductors? *Phys. Rev. Lett.*, 109:136401, 2011. doi:10.1103/PhysRevLett.109.136401. (p. 72)

[155] S. Olthof, S. Mehraeen, S. K. Mohapatra, S. Barlow, V. Coropceanu, J.-L. Brédas, S. R. Marder, and A. Kahn. Ultralow doping in organic semiconductors: Evidence of trap filling. *Phys. Rev. Lett.*, 109:176601, 2012. doi:10.1103/PhysRevLett.109.176601. (p. 72)

[156] Y. Kawamura, J. Brooks, J. J. Brown, H. Sasabe, and C. Adachi. Intermolecular interaction and a concentration-quenching mechanism of phosphorescent ir(iii) complexes in a solid film. *Phys. Rev. Lett.*, 96(1):017404, 2006. doi:10.1103/PhysRevLett.96.017404. (p. 73, 74)

[157] S. Mladenovski, S. Reineke, and K. Neyts. Measurement and simulation of exciton decay times in organic light-emitting devices with different layer structures. *Opt. Lett.*, 34(9):1375–1377, 2009. doi:10.1364/OL.34.001375. (p. 74)

[158] K.-C. Tang, K. L. Liu, and I.-C. Chen. Rapid intersystem crossing in highly phosphorescent iridium complexes. *Chem.Phys. Lett.*, 386(4–6):437–441, 2004. doi:10.1016/j.cplett.2004.01.098. (p. 74)

[159] F. S. Steinbacher, R. Krause, A. Hunze, and A. Winnacker. Triplet exciton transfer mechanism between phosphorescent organic dye molecules. *Phys. Stat. Sol. (a)*, 209(2):340–346, 2012. doi:10.1002/pssa.201127451. (p. 74, 75)

[160] G. Schwartz, S. Reineke, T. Rosenow, K. Walzer, and K. Leo. Triplet harvesting in hybrid white organic light-emitting diodes. *Adv. Funct. Mater.*, 19(0):1319–1333, 2009. doi:10.1002/adfm.200801503. (p. 74)

[161] J. J. M. van der Holst, F. W. A. van Oost, R. Coehoorn, and P. A. Bobbert. Electron-hole recombination in disordered organic semiconductors: Validity of the langevin formula. *Phys. Rev. B*, 80:235202, 2009. doi:10.1103/PhysRevB.80.235202. (p. 77)

[162] J. J. Kwiatkowski, J. Nelson, H. Li, J. L. Bredas, W. Wenzel, and C. Lennartz. Simulating charge transport in tris(8-hydroxyquinoline)

aluminium (alq3). *Phys. Chem. Chem. Phys.*, 10:1852–1858, 2008. doi:10.1039/b719592c. (p. 79, 108)

[163] V. Rühle, A. Lukyanov, F. May, M. Schrader, T. Vehoff, J. Kirkpatrick, B. Baumeier, and D. Andrienko. Microscopic simulations of charge transport in disordered organic semiconductors. *J. Chem. Theor. Comp.*, 7(10): 3335–3345, 2011. doi:10.1021/ct200388s. (p. 79)

[164] J. Cottaar, R. Coehoorn, and P. A. Bobbert. Scaling theory for percolative charge transport in molecular semiconductors: Correlated versus uncorrelated energetic disorder. *Phys. Rev. B*, 85:245205, 2012. doi:10.1103/PhysRevB.85.245205. (p. 83)

[165] J. Cottaar, R. Coehoorn, and P. A. Bobbert. Field-induced detrapping in disordered organic semiconducting host-guest systems. *Phys. Rev. B*, 82: 205203, 2010. doi:10.1103/PhysRevB.82.205203. (p. 84)

[166] H. Nicolai, M. Kuik, G. Wetzelaer, B. de Boer, C. Campbell, C. Risko, J. Brédas, and P. Blom. Unification of trap-limited electron transport in semiconducting polymers. *Nature Mater.*, 11:882, 2012. doi:10.1038/nmat3384. (p. 85)

[167] R. Nitsche. Sim4tec AG, Germany, private communication. (p. 86)

[168] S. Noh, C. K. Suman, Y. Hong, and C. Lee. Carrier conduction mechanism for phosphorescent material doped organic semiconductor. *J. Appl. Phys.*, 105(3):033709, 2009. doi:10.1063/1.3072693. (p. 86)

[169] J. Kalinowski, W. Stampor, J. Mężyk, M. Cocchi, D. Virgili, V. Fattori, and P. Di Marco. Quenching effects in organic electrophosphorescence. *Phys. Rev. B*, 66:235321, 2002. doi:10.1103/PhysRevB.66.235321. (p. 98)

[170] S. Reineke, K. Walzer, and K. Leo. Triplet-exciton quenching in organic phosphorescent light-emitting diodes with ir-based emitters. *Phys. Rev. B*, 75:125328, 2007. doi:10.1103/PhysRevB.75.125328. (p. 98, 99)

[171] T. Neumann, D. Danilov, C. Lennartz, and W. Wenzel. Modeling disordered morphologies in organic semiconductors. *J. Comput. Chem.*, 34(31): 2716–2725, 2013. doi:10.1002/jcc.23445. (p. 108)

[172] B. Baumeier, O. Stenzel, C. Poelking, D. Andrienko, and V. Schmidt. Stochastic modeling of molecular charge transport networks. *Phys. Rev. B*, 86:184202, 2012. doi:10.1103/PhysRevB.86.184202. (p. 108)

INDEX

SUMMARY

MOLECULAR-SCALE SIMULATION OF ELECTRONIC PROCESSES IN ORGANIC WHITE LIGHT-EMITTING AND SINGLE-CARRIER DEVICES: STEADY-STATE AND TIME-DEPENDENT RESPONSES

The realization of devices of organic semiconductors has resulted in a new field in technology called "organic electronics", holding great promises of low production costs and unique properties when compared to traditional inorganic electronics. A particularly promising class of devices are organic light-emitting devices – OLEDs – emitting white light. Such "white OLEDs" are candidates for future lighting applications with unique and appealing features like homogeneous brightness over a large emitting area, mechanical flexibility, and low power consumption. However, large research and development efforts are still needed to improve the energy efficiency, color rendering, and stability of white OLEDs. Crucial in this respect is a complete understanding at the molecular scale of the electronic processes that are responsible for their performance. This thesis focuses on steady-state and time-dependent responses of organic devices to an applied voltage caused by the electronic processes taking place in the disordered organic semiconductors from which they are composed. The computer simulations that we have employed turned out to be essential in studying these electronic processes and to identify parameters that determine the device performance.

Electronic processes in disordered organic semiconductors differ completely from those in their conventional crystalline inorganic counterparts. Instead of delocalizing and forming energy bands, charge carriers in these semiconductors are localized by the disorder to specific sites. The energy levels of these sites form a distribution that is often described by a Gaussian function with a certain width, which is referred to as the disorder strength. Conduction occurs by thermally assisted tunneling – hopping – of charges between sites. The rate of these hops is determined by the overlap of the wave functions and the energy difference between the initial and final state.

In addition to the steady-state response of an organic device to a constant applied voltage, an analysis of the time-dependent response to a non-constant voltage can improve our understanding of charge dynamics, including charge

trapping. Charge-carrier relaxation in hole-only devices of a polyfluorene-based light-emitting polymer is studied in this thesis by modeling the current transient in a dark-injection experiment and comparing this to the measured transient. In such experiment the voltage across the device is abruptly increased, after which the time-dependent current is monitored. The resulting current transient depends on the charge-transport properties of the organic semiconductor. Modeling the current by solving a one-dimensional master equation using the instantaneous equilibrium charge-carrier mobility neglects charge-carrier relaxation and predicts too slow transients. Three-dimensional molecular-scale modeling, however, yields transients with a correct time scale. Using a disorder strength somewhat smaller than extracted from temperature-dependent current density-voltage profiles, the current transients are found to agree well with experiment.

Charge-carrier relaxation is also studied in this thesis via simulations of impedance spectroscopy. In this technique, a small ac voltage is applied to an organic device in addition to a dc voltage. From the measured current response, the capacitance-voltage, C–V, curve can be obtained as a function of frequency. One-dimensional modeling using the equilibrium mobility leads to C–V curves that deviate strongly from experiment. We performed simulations of the C–V curve by solving a time-dependent three-dimensional master equation in a similar way as for the dark-injection modeling and for exactly the same hole-only devices. A good agreement with the measured C–V curves is obtained if a comparable disorder strength is assumed as in the dark-injection modeling.

Finally, three-dimensional Monte Carlo simulations are performed to study electroluminescence in a white multilayer OLED. Obtaining white light from an OLED is challenging and the state-of-art approach is to use multilayer structures, where several thin organic layers performing different tasks are placed between one transparent and one metallic electrode. Hole and electron injecting and transporting layers inject and transport electrons and holes to different emitting layers where they form excitons on emitter molecules of the right color. On the emitter molecules the excitons can decay radiatively or non-radiatively. The radiative decay is fluorescent or phosphorescent depending on the spin configuration of the generated exciton (singlet or triplet) and the presence of a heavy-metal atom inducing spin-orbit coupling. In addition, exciton diffusion can occur via a Förster- or Dexter-type energy-transfer mechanism. For a hybrid white OLED based on blue fluorescence and green and red phosphorescence we consider all these processes by using rates for each process obtained from literature and specific measurements. The simulated current density and emission profile agree well with experiment and the exciton transfer from green to red is shown to be crucial for the color balance in this OLED.

In addition, the internal quantum efficiency as a function of current density is simulated for this OLED. The initial increase of the efficiency with current density, the roll-on, can be largely explained from a reduced formation of non-radiative excitons formed in the interlayer between the blue fluorescent and the green phosphorescent layer. At high current density the efficiency shows a decrease, the roll-off. This roll-off, which is caused by exciton-quenching processes, is an important factor limiting the performance and lifetime of OLEDs. We model exciton quenching by assuming that in a nearest-neighbor encounter of a triplet exciton and a charge, or of two triplet excitons, one exciton is lost. Our simulations show that for the considered white OLED the first process is more important than the second. However, the simulated roll-off occurs at a too high current density, which indicates that for a proper description of the roll-off long-range exciton-quenching processes should be accounted for. We made an initial study of such processes. A proper description of exciton quenching is crucial for the development of white OLEDs with higher efficiencies and longer lifetimes.

LIST OF PUBLICATIONS

PUBLICATIONS IN PEER-REVIEWED JOURNALS

1. M. Mesta, M. Carvelli, R. J. de Vries, H. van Eersel, J. J. M. van der Holst, M. Schober, M. Furno, B. Lüssem, K. Leo, P. Loebl, R. Coehoorn, and P. A. Bobbert, Molecular-scale simulation of electroluminescence in a multilayer white organic light-emitting diode, *Nature Mater.*, 12(7), 652 (2013)
2. M. Mesta, C. Schaefer, J. de Groot, J. Cottaar, R. Coehoorn, and P. A. Bobbert, Charge-carrier relaxation in disordered organic semiconductors studied by dark injection: Experiment and modeling, *Phys. Rev. B*, 88(17), 174204 (2013)
3. M. Mesta, J. Cottaar, R. Coehoorn, and P. A. Bobbert, Study of charge-carrier relaxation in a disordered organic semiconductor by simulating impedance spectroscopy, *Appl. Phys. Lett.* 104, 213301 (2014)
4. M. Mesta, H. van Eersel, R. Coehoorn, and P. A. Bobbert, Modeling of exciton processes in a multilayer white organic light-emitting diode, *in manuscript*, (2015)

AUTHOR CONTRIBUTIONS TO PUBLICATIONS

Publication 1 (Chapter 5): M. Mesta carried out the main Monte Carlo simulations and the analysis of the results. M. Carvelli performed the main measurements on the OLED and the reconstruction of the emission profile. R. J. de Vries determined the electron transport parameters in Spiro-DPVBi and NET5. H. van Eersel programmed the exciton diffusion software. J. J. M. van der Holst was involved in setting up the Monte Carlo simulations. M. Schober and M. Furno fabricated the OLED, provided its experimental optimization and characterization, and determined the hole transport parameters. B. Lüssem and K. Leo supervised the work of M. Schober and M. Furno. P. Loebl was involved in the definition of the OLED stack, the UPS and optical measurements on the stack materials, and the fabrication of devices for the determination of electron transport parameters. R. Coehoorn and P.A. Bobbert supervised the work and the writing of the manuscript.

Publication 2 (Chapter 3): M. Mesta carried out the 3D-ME simulations, made minor adaptations to the 3D-ME solver, and performed the analysis of the results. C. Schaefer performed the DI measurements and the 1D simulations. J. de Groot carried out the 3D-MC simulations. J. Cottaar performed the main programming of 3D-ME solver. R. Coehoorn and P.A. Bobbert supervised the work and the writing of the manuscript.

Publication 3 (Chapter 4): M. Mesta carried out the 3D-ME simulations, made minor adaptations to the 3D-ME solver, and performed the analysis of the results. J. Cottaar performed the main programming of 3D-ME solver. R. Coehoorn and P.A. Bobbert supervised the work and the writing of the manuscript.

Publication 4 (Chapter 6): M. Mesta carried out the Monte Carlo simulations and the analysis of the results. H. van Eersel performed the main programming and the measurements. R. Coehoorn and P.A. Bobbert supervised the work and the writing of the manuscript.

CONTRIBUTIONS TO INTERNATIONAL CONFERENCES

1. M. Mesta, H. van Eersel, R. Coehoorn, and P. A. Bobbert, Molecular-scale simulation of a multilayer white OLED: Electroluminescence and efficiency roll-off, *International Conference on Synthetic Metals*, Turku (2014) – Oral presentation
2. M. Mesta, M. Carvelli, R. J. de Vries, H. van Eersel, J. J. M. van der Holst, M. Schober, M. Furno, B. Lüssem, K. Leo, P. Loebl, R. Coehoorn, and P. A. Bobbert, Molecular-scale simulation of electroluminescence in a multilayer white OLED, *SPIE Photonics Europe*, Brussels (2014) – Oral presentation
3. M. Mesta, J. de Groot, C. Schaefer, H. van Eersel, R. Coehoorn, and P. A. Bobbert, Advanced molecular-scale modelling of electronic processes in OLED stacks and materials, 12^{th} *European Conference on Molecular Electronics*, London (2013) – Poster presentation
4. M. Mesta, M. Carvelli, R. J. de Vries, H. van Eersel, J. J. M. van der Holst, R. Coehoorn, P. A. Bobbert, Molecular-scale simulation of electroluminescence in a multilayer white OLED, *The Material Research Society Spring Meeting*, San Francisco (2013) – Poster presentation
5. M. Mesta, J. J. M. van der Holst, F. W. A. van Oost, R. Coehoorn, and P. A. Bobbert, Monte Carlo simulations of electronic processes in a red-emitting multilayer OLED, 11^{th} *European Conference on Molecular Electronics*, Barcelona (2011) – Poster presentation

CURRICULUM VITÆ

Murat Mesta was born on 22nd of July 1984 in Ankara, Turkey. After finishing his high-school education in Ankara, he was admitted to the prestigious Middle East Technical University in Ankara to study Physics. During his undergraduate education his interest was in condensed matter theory. He obtained his Bachelor of Science degree in Physics in July 2007 after completing his graduation thesis on lattice dynamics of cesium chloride under the supervision of Prof. Dr. Şinasi Ellialtıoğlu. In his master's project, he focused on the study of the electronic structure of titanium surfaces applied to dye-sensitized solar cells. This gave him the opportunity to gain hands-on experience with methods employing density-functional theory. After successfully completing his master's study in Ankara, he joined the Fritz Haber Institute of the Max Planck Society in Berlin in 2010 to conduct research in the group of Prof. Dr. Klaus Hermann. He enrolled in a collaborative project on the theoretical analysis of near-edge x-ray absorption fine-structure spectroscopy of porphyrin-based molecular switches for a period of half a year. After that he moved to the Eindhoven University of Technology in January 2011 to work as a PhD student in the group of Dr. Peter A. Bobbert and Prof. Dr. Reinder Coehoorn. The main results of his PhD research are presented in this dissertation and have been presented at international conferences in Barcelona, San Francisco, London, and Turku.

ACKNOWLEDGEMENTS

This thesis couldn't have been completed without the help and support of many people.

First of all, I would like to express my deepest gratitude to my supervisor, Reinder Coehoorn and my co-supervisor Peter A. Bobbert, not only for their continuous support in completing this thesis, but also for their sincere supervision of my research during the last four years. Peter, I particularly acknowledge your able guidance and your critical reading of the manuscript that put me on the right track and allowed me to successfully complete this dissertation.

I would like to thank all the members of the reading committee; Jenny Nelson, Geert Brocks, René Janssen, Herman Clercx, and Stefan Meskers for their critical reviews and suggestions. Your valuable comments have improved the text in many ways.

Next, I would like to thank my PhD collaborators at Philips Eindhoven and TU/e; Marco Carvelli, Rein de Vries, Jeroen van der Holst, and Harm van Eersel, for their enthusiastic participation in our research and the fruitful discussions that we have had during our meetings. I am also grateful to Frank van Oost for his technical guidance during the early stages of my research. I should not forget to thank Alexey Lyulin for the useful discussions and for his kind companionship.

I also thank Helmi van Lieshout for her administrative support during my four years of stay in Eindhoven.

In the past four years, I was fortunate to have great friends and colleagues that made my stay in Eindhoven a memorable one. Their presence has always motivated me and writing this dissertation would not have been possible without their continuous support. I would also like to thank all the members of the groups "Theory of Polymers and Soft matter" and "Molecular Materials and Nanosystems" that I have met and worked with in the past four years, for establishing such a friendly research environment. Our scientific discussions, group seminars, lunch and coffee breaks, group outings and also the movie nights have motivated me in many different ways. In particular, I would like to thank Abhinav Sharma for his suggestions that helped me establish a better perspective of my research, Augusto Batagin-Neto for his sincere friendship and the many discussions that we had during his short stay in our group, Andrea Massé and Vikas Negi for creating a friendly office space to share with,

which I also appreciate the most while finalizing this dissertation, Vikas for his reading and for his comments on some parts of the manuscript.

I also appreciate the support of my friends from Turkey; Efe, Buket, İlker, Nurcan, and Orhan. Their friendship and kind hospitality had motivated me to continue working on this dissertation even during the toughest times. Efe and İlker, it has been such a pleasure to have all those lovely discussions with you during the coffee and lunch breaks.

My parents have unconditionally loved and supported me all throughout my life, and they have always been with me during my study in Eindhoven away from my homeland. I would like to thank them in our native language: *Sevgili annem, babam ve canım ablam; bugüne kadar hep yanımda olduğunuz ve beni desteklediğiniz gibi bu tezi oluşturan dört yıllık çalışmam boyunca da beni desteklediğiniz için size sonsuz teşekkür ederim. Anne ve baba, aldığım bütün eğitimi size borçluyum ve her zaman eğitime değer veren sorumluluk sahibi ebeveynler olduğunuz için size minettarım.*

Finally, I would like to thank my partner Gönül Ünal for the many discussions we had to improve the manuscript, particularly Chapter 2, and her endless support while writing this thesis. Gönül, I cannot express how grateful I am to have you contributing in every important aspect of my life, including this thesis. In the past four years, you patiently listened to all the problems that I had, you never gave up, and you always encouraged me to continue working no matter how hard the situation was. Although, we have been separated by thousands of kilometers, all this while, you never let me feel alone. Thank you for opening your wonderful heart to me.

M. Mesta

Eindhoven, 2015